UNIVERSITY OF COPENHAGEN
FACULTY OF SCIENCE

NIELS BOHR INSTITUTE

Modeling diurnal sea surface warming in the tropical ocean

An interactive boundary condition
for idealized atmospheric simulations

Master Thesis

submitted by

Reyk Börner

in partial fulfillment of the
Master of Science in Physics

August 16, 2021

supervised by

Jan O. Haerter
Romain Fiévet
Peter Ditlevsen

Abstract

A better understanding of self-organizing tropical convection holds the potential to reduce long-standing uncertainties around climate sensitivity and predicting extreme events. Idealized cloud-resolving simulations are known to exhibit convective self-aggregation over a constant and homogeneous sea surface temperature (SST). At the same time, there is increasing evidence that artificially imposed SST variations – such as spatial inhomogeneities or a diurnal cycle – impact the clustering of convection. This has sparked renewed interest in more realistic representations of ocean-atmosphere interaction, particularly diurnal SST variability. Recent numerical studies have included a slab ocean as a responsive lower atmospheric boundary. However, by ignoring wind-induced vertical mixing, slab models with fixed slab depth neglect a crucial wind effect on sea surface warming. To address this, we present an idealized, one-dimensional model of heat transfer in the upper few meters of the ocean, forced by insolation and atmospheric conditions. Unlike slab oceans, our model includes important processes such as wind-driven turbulent diffusion, near-surface heat trapping, and skin cooling, while retaining conceptual simplicity. We describe the depth-resolved temperature evolution by only a few parameters, which we estimate with Bayesian inference using a combination of radiometric SST measurements, ship records, and buoy data. Subsequent analysis verifies that our model is capable of reproducing key features of diurnal warming in the tropical ocean. Aiming to be versatile, computationally affordable and easy to code, the model is suited as an interactive surface boundary condition for high-resolution cloud-resolving simulations. Thus, our work could enable a next step towards more realism in idealized simulations of the tropical atmosphere, seeking to help build the bridge between conceptual modeling and real-world process understanding.

Acknowledgements

This thesis is the result of nine exciting months in the Atmospheric Complexity group. Despite a global pandemic and a research group split between two locations in Bremen and Copenhagen, I felt a part of an inspiring and super friendly team. First of all, my thanks go out to Jan Haerter, who managed to be there as a supervisor and mentor even though we first met in person after eight months. No matter whether it was the first or the seventeenth zoom meeting of the day, Jan was always curious to hear about my project and provided guidance to move forward. I would equally like to thank Romain Fiévet, who was always available to discuss and offered great help with all the numerical instabilities that arose in the course of this work. Furthermore, I am grateful to Peter Ditlevsen for his interest in following along with the project.

I would like to thank Peter Minnett for providing the MOCE-5 dataset and gratefully acknowledge the Pacific Marine Environmental Laboratory at NOAA for making the GTMBA buoy data available.

Lastly, I would like to thank coagulation, condensation, and convection for tirelessly walking around randomly in parameter space, no matter how often their proposed move was rejected.

Beyond writing my thesis, it was a great experience to be involved in numerous group activities and to learn a lot about the fascinating world of clouds in our weekly group meetings. I look forward to staying in touch!

Code availability: `https://github.com/reykboerner/diusst`

Contact: reyk.boerner@online.de

Contents

List of Figures

1 Introduction

Suppose we double the concentration of carbon dioxide in the Earth's atmosphere. By how much will the global mean temperature rise, if we wait until it equilibrates? This long-standing question remains difficult to answer, despite significant advancements in observations, theories, and modeling [1]. Much of the uncertainty around climate sensitivity stems from our limited understanding of clouds in a changing climate [2, 3]. Unraveling how clouds interact with the radiative energy balance, the large-scale atmospheric circulation, and the water cycle belongs to the key challenges of climate science today [4].

Clouds and convection are known to organize over a wide range of spatial and temporal scales [4, 5]. Particularly in the tropics, clouds tend to cluster in large convective systems, often associated with extreme rainfall and the genesis of tropical cyclones. The spatio-temporal patterns of tropical convection modulate weather and climate across the globe. Vice versa, the cloud field depends on the surrounding conditions, such as radiative forcing and large-scale flows. This chicken-versus-egg situation makes it challenging to understand fundamental mechanisms of convective organization. At the same time, an accurate parametrization of cloud processes is crucial in global climate models, since to date their spatial resolution does not permit to explicitly resolve relevant small-scale dynamics such as convective updrafts [2].

To tackle the complexity of nature, it is often useful to gain conceptual insight from simplified models. Cloud-resolving large-eddy simulations (LES) provide a powerful numerical laboratory to study tropical convection under idealized conditions. Over the past years, numerous studies have performed simulations of the atmosphere under radiative-convective equilibrium (RCE) – a thermal steady-state where constant solar forcing is balanced by outgoing longwave radiation above a constant and homogeneous lower boundary surface [6, 7, 8]. In these simulations, clouds spontaneously self-organize until they form a single cluster. Studying this effect known as convective self-aggregation may help illuminate the feedback processes that facilitate aggregation in nature [9]. However, the assumption of a fixed uniform surface temperature is often unrealistic, given that both land and ocean surfaces show diurnal temperature oscillations [10, 11].

Recent idealized simulations show that an imposed diurnal cycle of sea surface temperature (SST) can substantially alter the spatio-temporal patterns of convection, as compared to the RCE case [12, 13]. Aggregation emerges, yet seemingly by different mechanisms. Likewise, spatial variations in SST have been shown to imprint themselves on the moisture field [14, 15]. These findings suggest to include a more realistic lower boundary condition in atmospheric simulations.

Here, we focus on the tropical ocean, which covers three quarters of the tropics and about thirty percent of the Earth's surface area. If you have ever jumped into the sea on a warm summer day, you may have experienced that the water gets noticeably cooler one or two meters below the surface. This phenomenon arises from an intricate competition

of near-surface heat trapping due to absorbed solar radiation and wind-driven turbulent mixing [10, 16, 17]. Diurnal warming in the tropical ocean can reach amplitudes of several degrees Celsius on calm and clear days, which could have relevant implications for air-sea interactions [18]. Indeed, neglecting the diurnal cycle may lead to an error on the order of $10\,\mathrm{W\,m^{-2}}$ in monthly-averaged surface heat fluxes [19]. It has been proposed that diurnal SST variation may play an important role in large-scale coupled ocean-atmosphere processes such as the Madden-Julian Oscillation [20].

A first step from a fixed to an interactive SST is to represent the ocean as a single-layer slab with a certain heat capacity, which absorbs and re-emits heat according to parametrized surface fluxes. Several studies have coupled a slab ocean to cloud-resolving simulations [21, 22, 23, 24]. Overall, these works report that a responsive SST slows down the onset of convective aggregation. However, one-layer slab models with constant thickness may be insufficient to represent diurnal surface warming because they omit a critical factor: the wind dependence of vertical oceanic heat transport.

To address this, we present an idealized, one-dimensional model of diurnal temperature evolution in the upper few meters of the tropical ocean. Forced by solar insolation and atmospheric conditions, our model treats turbulent mixing as diffusion combined with an additional temperature relaxation term. This retains conceptual simplicity while mimicking important processes such as wind-driven vertical mixing, near-surface heat trapping, and skin cooling. Using a combination of ship and buoy measurements, we show that the model is capable of reproducing key features of diurnal surface warming.

Upper ocean heat transfer has been modeled on various levels of complexity over the last fifty years, ranging from fully turbulent-resolving models [25, 26, 16, 27, 28] to simplified bulk or slab models [17, 29, 30, 31] and empirical models [32, 33, 34, 35, 36]. Rather than attempting to improve on these models, our approach seeks to address the need of a "plug-and-play" ocean surface for high-resolution atmospheric simulations. Being easy to implement and computationally feasible, our model could be suitable as an interactive lower boundary condition for a more realistic representation of air-sea interactions. Hopefully, this could help bridge the current gap between conceptual modeling and real-world process understanding.

This work consists of three parts. First, we conduct an observational analysis of diurnal SST variation at different locations in the tropical ocean. Building on the insight from this study, we next develop our model. We discuss different variants based on the principle of staying as simple as possible but as complex as necessary. In the final part, we then bring the data and model together, using Bayesian inference to estimate the parameters of our model.

2 Mathematical toolbox

Before we dive into the upper ocean, let us take a quick tour through selected topics in numerical analysis, fluid dynamics, and statistics to attain a mathematical background for our study. First, we review the finite difference method to solve partial differential equations numerically, focusing on what we will need. We show how to generalize to a non-uniform spatial mesh and discuss different time-stepping schemes. The second part introduces theoretical and practical concepts of Bayesian inference, laying a foundation for the data-driven analysis to follow. If you wish to save the technical details for later, skip to page 14.

2.1 Numerical solution of partial differential equations

Consider a partial differential equation (PDE) for $y \equiv y(x,t)$ of the form

$$\frac{\partial y}{\partial t} = A\frac{\partial^2 y}{\partial x^2} + B\frac{\partial y}{\partial x} + Cy + D \ , \tag{2.1}$$

where $t \in [0, \mathcal{T}]$ represents time, $x \in [0, L]$ is the spatial coordinate, and $y : [0, L] \times [0, \mathcal{T}] \to \mathbb{R}$. If the coefficients A, B, C, and D only depend on x and t but not on y, the PDE is linear.

Even the linear case is typically not solvable analytically, except for some simple cases with specific boundary conditions. Therefore, we rely on numerical integration methods to solve eq. (2.1) in time and space, given an initial condition $y_0 \equiv y(x,0)$ and suitable boundary conditions $y(0,t)$, $y(L,t)$. One vastly used approach is the finite difference method, which we discuss here. The general idea is to approximate the spatial derivatives as difference quotients, turning the PDE into a system of coupled ordinary differential equations (ODEs). This system of equations can then be iteratively solved in time, starting out at the initial condition and advancing in discrete time steps.

2.1.1 Discretization of space

To approximate the spatial derivatives, the interval $[0, L]$ is discretized into $N+1$ points x_n, with $n \in \{0, 1, \ldots, N\}$ such that $x_0 = 0$ and $x_N = L$. If the spacing between points is constant, we refer to this as a *uniform grid*, that is,

$$\Delta x_n := x_{n+1} - x_n = \Delta \qquad \forall\ n \in \{0, \ldots, N-1\} \ ,$$

where $\Delta > 0$ is the constant grid step. For now, we will stick to the uniform grid and later extend the results to the non-uniform case.

Consider the Taylor series for y around the point x_n at any given t, evaluated at the two adjacent grid points $x_{n\pm1} = x_n \pm \Delta$:

$$y(x_n + \Delta) = y(x_n) + \Delta \left.\frac{\partial y}{\partial x}\right|_{x_n} + \frac{\Delta^2}{2} \left.\frac{\partial^2 y}{\partial x^2}\right|_{x_n} + \mathcal{O}(\Delta^3) \ , \tag{2.2a}$$

$$y(x_n - \Delta) = y(x_n) - \Delta \left.\frac{\partial y}{\partial x}\right|_{x_n} + \frac{\Delta^2}{2} \left.\frac{\partial^2 y}{\partial x^2}\right|_{x_n} + \mathcal{O}((-\Delta)^3) \ . \tag{2.2b}$$

We have omitted the time arguments for clarify. Subtracting the second equation from the first gives

$$y(x_{n+1}) - y(x_{n-1}) = 2\Delta \left.\frac{\partial y}{\partial x}\right|_{x_n} + \mathcal{O}(\Delta^3) \ . \tag{2.3}$$

Note that the terms of even order (zeroth, second, ...) cancel. Dividing by 2Δ yields

$$\left.\frac{\partial y}{\partial x}\right|_{x_n} = \frac{y(x_{n+1}) - y(x_{n-1})}{2\Delta} + \mathcal{O}(\Delta^2) \ . \tag{2.4}$$

Thus we may approximate the first derivative of y at point x_n by a finite difference between the adjacent grid points. The error of this approximation is of the order Δ^2, which is termed *second order accurate*. Eq. (2.4) is commonly known as the *central difference*. Similarly, we may derive the *forward* and *backward difference* from eq. (2.2a) (using the grid points n and $n+1$), respectively eq. (2.2b) (using the grid points $n-1$ and n). However, the forward and backward differences are only first order accurate because the second order Taylor term does not cancel, making the central difference preferable. Generally, it is possible to obtain finite difference schemes of higher accuracy by including additional neighboring grid points in the approximations. However, this comes at a higher computational cost, so that a trade-off must be made between accuracy and speed, depending on the problem in question.

To derive a central difference equation for the second spatial derivative of y, we add eqs. (2.2a) and (2.2b). In that case all the odd-order terms of the Taylor expansion cancel, and we find, up to second order accuracy,

$$\left.\frac{\partial^2 y}{\partial x^2}\right|_{x_n} = \frac{y(x_{n+1}) - 2y(x_n) + y(x_{n-1})}{\Delta^2} + \mathcal{O}(\Delta^2) \ . \tag{2.5}$$

Inserting eqs. (2.4) and (2.5) into the PDE (2.1) replaces the spatial derivatives by algebraic expressions, leading to a system of coupled ODEs. However, we must treat the boundary points x_0 and x_N with special care because the points x_{-1} or x_{N+1} are not defined. If $y(x_0)$ and $y(x_N)$ are specified through (Dirichlet) boundary conditions, it suffices to evaluate the points in between ($1 \leq n \leq N-1$) and there is no problem. Contrarily, under free boundary conditions we also need to evaluate derivatives at the edge points. Suppose the value of $y(x_0, t)$ is free to evolve according to the PDE, i.e. we must solve for it as a function of time. One option is to define a *ghost point* x_{-1} outside of the domain. Its value $y(x_{-1}, t)$ is extrapolated from $y(x_0, t)$, and we can then use the central difference scheme to evaluate derivatives at x_0. Alternatively, we could use a forward difference at the boundary, which only involves grid points within the domain.

Non-uniform grid. In many applications of computational fluid dynamics, the spatial domain contains regions of special interest where the solution $y(x,t)$ varies rapidly with x. For example, when studying air-sea interactions, we are dealing with boundary layers at the air-sea interface. Near the interface, shear as well as cross-boundary fluxes of energy, mass, and momentum play an important role, such that we may expect relatively large gradients in the quantities we aim to model.

To obtain an accurate solution in regions of large gradients, we require a sufficiently high spatial resolution, i.e. small grid spacing Δ. On the other hand, a fine-resolution grid is computationally expensive. Using a uniform grid throughout the domain may thus be inefficient since "uneventful" parts of the domain do not require such fine resolution. This issue naturally leads to the idea of a *non-uniform grid* in which the grid spacing depends on position,

$$\Delta x_n := x_{n+1} - x_n \neq \text{const.}$$

The objective is to determine a function which constructs a grid with small spacing in the regions of large gradients and larger spacing otherwise.

When using a non-uniform grid, the discretization of spatial derivatives must account for the asymmetry in the grid spacing. We cannot use the finite difference eqs. (2.4) and (2.5) directly, since they were derived using $\Delta x_m = \Delta x_n$ $(m \neq n)$, which led to a convenient cancellation of terms. If we would re-derive these equations with variable grid spacing, these terms would not cancel, and the truncation error would be larger (first order accurate instead of second order). However, there is an elegant way of using a non-uniform mesh while maintaining second-order accuracy. It involves transforming from "x-space" with non-uniform intervals Δx_n to a so-called *computational space*, or ξ-space, where the generalized grid coordinates ξ_n form a uniform grid,

$$\Delta \xi_n := \xi_{n+1} - \xi_n = 1 \ ,$$

without loss of generality. First, we need to write down a transformation rule $\xi : \{x_n\} \to \{\xi_n\}$, expressed as a continuous invertible function $\xi(x)$ on $[0, L]$ with inverse $x(\xi)$. Then, using the chain rule, the first derivative of a function f in x-space is given by

$$\frac{\mathrm{d}f}{\mathrm{d}x} = \frac{\mathrm{d}f}{\mathrm{d}\xi}\frac{\mathrm{d}\xi}{\mathrm{d}x} \ , \tag{2.6}$$

and, invoking the product rule, the second derivative in x-space becomes

$$\begin{aligned} \frac{\mathrm{d}^2 f}{\mathrm{d}x^2} &= \frac{\mathrm{d}}{\mathrm{d}x}\left(\frac{\mathrm{d}f}{\mathrm{d}\xi}\cdot\frac{\mathrm{d}\xi}{\mathrm{d}x}\right) \\ &= \frac{\mathrm{d}^2 f}{\mathrm{d}\xi^2}\left(\frac{\mathrm{d}\xi}{\mathrm{d}x}\right)^2 + \frac{\mathrm{d}f}{\mathrm{d}\xi}\frac{\mathrm{d}^2\xi}{\mathrm{d}x^2} \ . \end{aligned} \tag{2.7}$$

Since the grid in ξ-space is uniform, we can use eqs. (2.4) and (2.5) to approximate the derivatives of f with respect to ξ, noting that $f(x_n) = f(x(\xi_n))$. This gives, with second order accuracy in x-space,

$$\left.\frac{\mathrm{d}f}{\mathrm{d}x}\right|_{x_n} \approx \frac{f(x_{n+1}) - f(x_{n-1})}{2}\cdot\left.\frac{\mathrm{d}\xi}{\mathrm{d}x}\right|_{x_n} \ , \tag{2.8a}$$

$$\left.\frac{\mathrm{d}^2 f}{\mathrm{d}x^2}\right|_{x_n} \approx \frac{f(x_{n+1}) - 2f(x_n) + f(x_{n-1})}{1^2}\cdot\left(\left.\frac{\mathrm{d}\xi}{\mathrm{d}x}\right|_{x_n}\right)^2 + \frac{f(x_{n+1}) - f(x_{n-1})}{2}\cdot\left.\frac{\mathrm{d}^2\xi}{\mathrm{d}x^2}\right|_{x_n} \ . \tag{2.8b}$$

The derivatives of the coordinate transformation, $\mathrm{d}\xi/\mathrm{d}x$ and $\mathrm{d}^2\xi/\mathrm{d}x^2$, are calculated analytically for the specific form of $\xi(x)$.

2.1.2 Discretization of time

Now that we know how to turn spatial derivatives into algebraic expressions on a non-uniform grid, we are ready to integrate in time. To do this, we partition time into discrete steps t_i of duration Δt ($i \in \{0, 1, \ldots, M\}$). The general concept is then to iteratively move forward in time by calculating the solution at time t_{i+1} based on the solution at time t_i, starting with the known initial condition at t_0.

Euler method. Consider a general ODE

$$\frac{\partial y(x,t)}{\partial t} = F\Big(y(x,t)\Big) \ , \tag{2.9}$$

with initial condition $y_0 \equiv y(x, t_0)$. Approximating the time derivative by a forward difference, that is,

$$\left.\frac{\partial y(x,t)}{\partial t}\right|_{t_i} \approx \frac{y(x,t_{i+1}) - y(x,t_i)}{\Delta t} \ , \tag{2.10}$$

we arrive at a stepping procedure known as the *Euler method*: for $i \in \{0, 1, \ldots, M-1\}$,

$$y(x,t_{i+1}) = y(x,t_i) + \Delta t \cdot F\Big(y(x,t_i)\Big) + \mathcal{O}(\Delta t^2) \ . \tag{2.11}$$

In the linear case, F is a linear operator, and we may conveniently express the problem in the language of linear algebra. Writing $F(\vec{y}) = \hat{F} \cdot \vec{y} + \vec{b}$, we obtain the linear system of equations[1]

$$y_n^{i+1} = (\delta_{nm} + \Delta t\, F_{nm}^i) \cdot y_m^i + \Delta t\, b_n^i \ , \tag{2.12}$$

where $y_n^i \equiv y(x_n, t_i)$ and δ_{nm} is the Kronecker delta. The matrix $\hat{F}^i \equiv (F_{nm}^i)$ and the vector $\vec{b}^i \equiv b_n^i$ depend on the specific form of the ODE.

Let us now apply the Euler method to the PDE (2.1) introduced at the beginning. To illustrate how to treat edge points, suppose that we have a Dirichlet boundary condition at x_N, $y(x_N, t) = y_N$, as well as a free boundary condition at x_0, i.e. $y(x_0, t)$ evolves freely. For this case, the specific form of eq. (2.12) reads

$$\begin{pmatrix} y_0 \\ y_1 \\ \vdots \\ y_{N-1} \\ y_N \end{pmatrix}^{(i+1)} = \left(\mathbb{1} + \Delta t \begin{bmatrix} \alpha_1 & \beta_1^+ & 0 & \cdots & 0 \\ \beta_2^- & \alpha_2 & \beta_2^+ & \cdots & 0 \\ \vdots & \ddots & \ddots & \ddots & \vdots \\ 0 & \cdots & \beta_{N-1}^- & \alpha_{N-1} & \beta_{N-1}^+ \\ 0 & \cdots & 0 & 0 & 0 \end{bmatrix}^{(i)} \right) \cdot \begin{pmatrix} y_0 \\ y_1 \\ \vdots \\ y_{N-1} \\ y_N \end{pmatrix}^{(i)} + \Delta t \begin{pmatrix} b_0 \\ b_1 \\ \vdots \\ b_{N-1} \\ b_N \end{pmatrix}^{(i)} \ , \tag{2.13}$$

[1] We are using Einstein's sum convention here.

where the global superscript $(\cdot)$ indicates the time index. Here the non-zero elements of the $N \times N$ matrix (F^i_{nm}) are given by[2]

$$\begin{aligned} \alpha^i_n &:= C - 2A \cdot \Big(\xi'(x_n)\Big)^2 \\ \beta^{\pm,\,i}_n &:= A \cdot \Big((\xi'(x_n))^2 \pm \frac{1}{2}\xi''(x_n)\Big) \pm \frac{B}{2}\xi'(x_n) \;, \end{aligned} \tag{2.14}$$

and the vector b^i_n, which includes the inhomogeneous part of the PDE (2.1), becomes

$$\begin{pmatrix} b_0 \\ b_1 \\ \vdots \\ b_{N-1} \\ b_N \end{pmatrix}_{(i)} = \begin{pmatrix} D + \beta^-_1 y_{-1} \\ D \\ \vdots \\ D \\ 0 \end{pmatrix}_{(i)} \;. \tag{2.15}$$

In eq. (2.14), $\xi'(x_n)$ and $\xi''(x_n)$ are short notation for the derivatives of the grid transformation ξ (see eq. (2.8)). The factors A, B, C, and D are the coefficients of eq. (2.1); we re-emphasize that in general they may depend on x and t, even though we have omitted this here for readability. Lastly, note that we have introduced a ghost point y_{-1} for handling the free boundary condition at x_0, while the Dirichlet boundary condition fixes the value of y_N in time. Since we do not know the value of y at the ghost point, we must extrapolate from y^i_0. A basic choice is simply $y^i_{-1} = y^i_0$.

The Euler method scores with simplicity and computational speed, but it is only first order accurate in the time step Δt. While having a local truncation error of $\mathcal{O}(\Delta t^2)$ as shown in eq. (2.11), the accumulated error after repeated iterations in time will be on the order of Δt (global truncation error[3]).

Fourth-order Runge-Kutta method. We achieve higher accuracy by evaluating the problem at additional time points between t_i and t_{i+1} in order to better approximate the solution at t_{i+1}. This technique underlies a class of algorithms termed *Runge-Kutta methods*, of which the Euler method is the first-order special case. For later use we focus on the highly popular *fourth order Runge-Kutta method* (RK4), which boasts a global truncation error of $\mathcal{O}(\Delta t^4)$. It computes $y(x, t_{i+1})$ according to

$$y(x, t_{i+1}) = y(x, t_i) + \frac{1}{6}\Big(k_1 + 2k_2 + 2k_3 + k_4\Big) \;, \tag{2.16}$$

where

$$\begin{aligned} k_1 &:= \Delta t \cdot F\Big(y(x, t_i),\, t_i\Big) \\ k_2 &:= \Delta t \cdot F\left(y(x, t_i) + \frac{k_1}{2},\, t_i + \frac{\Delta t}{2}\right) \\ k_3 &:= \Delta t \cdot F\left(y(x, t_i) + \frac{k_2}{2},\, t_i + \frac{\Delta t}{2}\right) \\ k_4 &:= \Delta t \cdot F\Big(y(x, t_i) + k_3,\, t_i + \Delta t\Big) \;. \end{aligned} \tag{2.17}$$

[2]The expressions in eq. (2.14) for the matrix elements α and $\beta^\pm$ hold for a general non-uniform spatial grid, which makes them slightly more involved. In the case of a uniform grid with grid spacing Δ, the result simplifies by replacing $\xi'(x_n) \to 1/\Delta$ and $\xi''(x_n) \to 0$.

[3]To integrate over a duration $\mathcal{T}$, we require $\mathcal{T}/\Delta t \sim 1/\Delta t$ time steps, each contributing an error $\sim \Delta t^2$, accumulating in a global error $\sim \Delta t$.

Note that the first term k_1 evaluates F at time t_i, the second and third terms k_2, k_3 constitute intermediate evaluations at $t_i + \frac{\Delta t}{2}$, whereas k_4 evaluates F at t_{i+1}. The explicit time arguments play a role when we deal with non-autonomous systems.

Implicit methods. The Euler method and the RK4 method belong to the class of *explicit* schemes which directly calculate the next solution step from known quantities obtained at the previous step. A quick look at eqs. (2.11) and (2.16) confirms that the time argument t_{n+1} only appears on the left-hand side of these equations (which we are solving for), while the right-hand side exclusively contains terms at t_n. Recall that we used a forward difference in time to derive the Euler method. What happens when we approximate the time derivative in eq. (2.9) by a backward difference instead? We get

$$y(x, t_{i+1}) = y(x, t_i) + \Delta t \cdot F\Big(y(x, t_{i+1})\Big) + \mathcal{O}(\Delta t^2) \ . \tag{2.18}$$

Note that here the operator F depends on y at time t_{n+1}. Adopting previous notation, the corresponding linearized equation reads

$$y_n^{i+1} = y_n^i + \Delta t \, F_{nm}^{i+1} \, y_m^{i+1} + \Delta t \, b_n^{i+1} \ . \tag{2.19}$$

Now the solution of y_n^{i+1} depends on the solutions y_m^{i+1} at other grid points at the same time t_{n+1}, and it becomes clear that we must solve the coupled equations simultaneously. This procedure is termed an *implicit* method.

We rewrite eq. (2.19) in vector notation as

$$\boldsymbol{F}^{i+1} \cdot \vec{y}^{\,i+1} = \vec{y}^{\,i} + \Delta t \, \vec{b}^{\,i+1} \ , \tag{2.20}$$

where the matrix $\boldsymbol{F}^{i+1} := \mathbb{1} - \Delta t \, \hat{F}^{i+1}$ is assumed to possess an inverse $(\boldsymbol{F}^{i+1})^{-1}$. Solving for $\vec{y}^{\,i+1}$ then leads to

$$\vec{y}^{\,i+1} = (\boldsymbol{F}^{i+1})^{-1} \cdot \Big(\vec{y}^{\,i} + \Delta t \, \vec{b}^{\,i+1}\Big) \ . \tag{2.21}$$

As indicated by the superscript, $\boldsymbol{F}$ and $\vec{b}$ may depend on time but we assume that their time dependence is known. Thus, starting at $i = 0$, all terms on the right-hand side are known and we can iteratively solve for $\vec{y}^{\,i+1}$.

Explicit vs. implicit schemes. We have shown that we may solve a partial differential equation numerically either by an explicit or an implicit method. Which option should we choose? At first glance, we notice that implicit schemes require matrix operations such as inversion and matrix multiplication, which is computationally costly especially for large matrices, i.e. many grid points. Explicit schemes seem convenient and fast. However, it turns out that explicit schemes can become unstable whereas implicit schemes are unconditionally stable. This will become important later.

2.2 Bayesian inference

Any modeling study that seeks to describe aspects of the real world requires a coherent method to quantify "goodness." To what degree does the model output match observations?

In a probabilistic sense, this translates to asking, *how likely is it that the model represents the truth, given what we know from observational data?* Bayesian statistics provide a systematic approach to answering this question.

Let us define a model $\mathcal{M}(\Theta)$ governed by a set of N_Θ parameters Θ. Generally, we do not know the *true* values of these parameters. We also specify a dataset $\mathcal{D}$ which contains observations of the feature or phenomenon to be modeled. For the chosen model $\mathcal{M}$, our goal is now to infer the conditional probability distribution of the parameters Θ, given the data $\mathcal{D}$. In the following, we denote *conditional probability* as $P(A|B)$, meaning "the probability of A under the condition that B is true."

Bayes' theorem. The conditional probability of a certain parameter combination $\Theta \equiv (\Theta_1, \Theta_2, \ldots, \Theta_{N_\Theta})$, given the data $\mathcal{D}$, follows from *Bayes' theorem* [37]:

$$P(\Theta|\mathcal{D}) = \frac{P(\mathcal{D}|\Theta) \cdot P(\Theta)}{P(\mathcal{D})} \ . \tag{2.22}$$

On the right-hand side, we have three terms. One is the *prior probability* $P(\Theta)$, or the probability of the parameters without knowledge of the data. The second factor in the numerator is the *likelihood* $P(\mathcal{D}|\Theta)$, describing the conditional probability of observing the data, assuming that the given parameters Θ represent the truth. The denominator $P(\mathcal{D})$ denotes the probability of the data being true. On the left-hand side, $P(\Theta|\mathcal{D})$ is called the *posterior probability* since it is the conditional probability of the parameters after gaining knowledge of the data.

We may think of any specific value of Θ as a hypothesis. The posterior probability tells us how likely this hypothesis is, given the data. Note that the denominator in eq. (2.22) does not depend on the hypothesis; it only makes a statement about the (generally unknown) truthfulness of the dataset. This is equivalent to marginalizing the joint probability of data and parameters over the parameters, i.e.,

$$P(\mathcal{D}) = \int P(\Theta, \mathcal{D}) \mathrm{d}\Theta = \int P(\mathcal{D}|\Theta) P(\Theta) \mathrm{d}\Theta \ , \tag{2.23}$$

where the integral is taken over all possible values of Θ. Substituting this expression for the denominator in eq. (2.22), we see that the posterior probability is normalized in the sense $\int P(\Theta|\mathcal{D}) \mathrm{d}\Theta = 1$. This reflects the tacit assumption that the model $\mathcal{M}$ is generally suitable for describing the data, albeit with an uncertainty in the parameters [38, 37].

Inferring the posterior parameter distribution. Once we have fixed a dataset, we are primarily interested in the relative probability of different hypotheses. It then suffices to consider the proportionality

$$P(\Theta|\mathcal{D}) \propto P(\mathcal{D}|\Theta) \cdot P(\Theta) \ . \tag{2.24}$$

Hence the product of the likelihood and the prior probability is proportional to the posterior probability [37].

The distributions of prior and posterior probabilities are multivariate probability distributions on the N_Θ-dimensional parameter space. Fig. 2.1 illustrates (in one dimension) that we may think of the posterior distribution as the overlap of the prior distribution

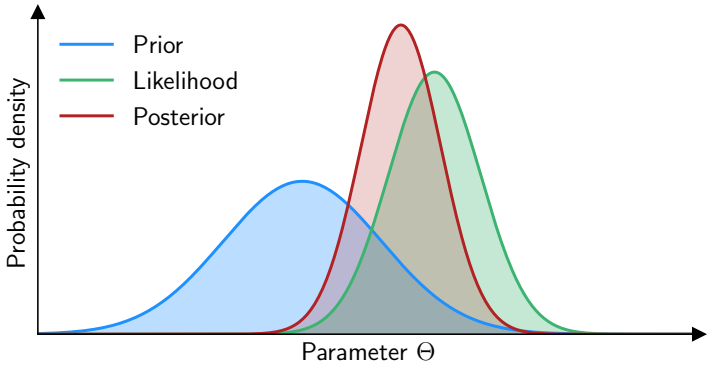

Figure 2.1: Bayesian inference The posterior distribution follows from the product of the prior distribution and the likelihood, as sketched here schematically for a one-dimensional parameter space.

with the likelihood function. The philosophy behind this lies at the heart of the Bayesian thinking, which interprets probability as a measure of confidence or belief. We begin with what we believe to know about the model parameters Θ and encapsulate this knowledge in the prior distribution. The prior knowledge could originate from previous statistical analysis, physical reasoning, or simply from a more or less educated guess. Then, the data comes into play, adding *new* information about which parameter values are more likely than others. Based on the additional knowledge, we update our belief, which hopefully reduces parameter uncertainty. This data-driven learning procedure is known as *Bayesian inference* [37, 38].

In practice, Bayesian inference involves three basic steps [39]:

1. Construct the prior distribution of parameters as a probability density in parameter space based on previous knowledge or belief. Often, the parameter space itself is bounded by physical or mathematical constraints. The more uncertain the prior belief, the broader and more delocalized the prior distribution should be.

2. Define the likelihood function, which serves as a measure of how well the data fits the model for fixed parameters. Since in fact the data are given while the parameters are unknown, it makes sense to interpret the likelihood as a function of Θ, denoted $\mathcal{L}(\Theta)$ (rather than treating it as the conditional probability of $\mathcal{D}$ given Θ). The choice of likelihood function is often ambiguous and should be adjusted to the problem at hand [38].

3. Compute the (unnormalized) posterior distribution by evaluating the product of likelihood and prior distribution. In most cases, $\mathcal{L}(\Theta)$ is too complicated to write in closed form, such that we must revert to approximation techniques (see below).

Bayesian inference allows us to sequentially update our knowledge as new data become available. To do this, we simply apply Bayes' theorem iteratively, using the posterior distribution of the previous update as the new prior distribution, and combining this with the likelihood derived from the new data to infer a refined posterior distribution.

A great benefit of Bayesian inference is that it provides an uncertainty measure that reflects all errors associated with the choice of model, in addition to the uncertainty originating from randomness and potential bias in the data. All these uncertainties factor into the shape of the posterior distribution, which encodes our confidence in a certain parameter

combination. To estimate the "best" parameter combination, several options exist:

- Maximum a posteriori estimate (MAP): the parameter combination Θ which maximizes the posterior distribution,

$$\hat{\Theta}_{\text{MAP}} := \arg\max_{\Theta} P(\Theta|\mathcal{D}) \ . \tag{2.25}$$

  If the prior distribution is uniform (i.e. constant in parameter space), the MAP estimate coincides with the maximum likelihood estimate (MLE).

- Mean estimate: Θ is estimated from the mean of the posterior distribution,

$$\hat{\Theta}_{\text{mean}} := \langle\Theta\rangle = \int \Theta P(\Theta|\mathcal{D})\,\mathrm{d}\Theta \ . \tag{2.26}$$

- Median estimate: Instead of the mean, we can also use the median of the posterior distribution as an estimate of Θ.

These estimates differ from each other if the posterior distribution is asymmetric; the most appropriate choice then depends on the situation.

Markov Chain Monte Carlo sampling. Typically, we cannot write down an explicit functional form of the posterior distribution because the likelihood function $\mathcal{L}(\Theta)$ depends on Θ in a complicated way. We can, however, select a specific value of Θ and state its posterior probability by calculating the product $\mathcal{L}(\Theta)P(\Theta)$. This is where Markov Chain Monte Carlo (MCMC) sampling comes into play.

Inspired by the randomness of a gamble in Monaco's famous casino, *Monte Carlo* methods utilize random sampling to numerically solve an often high-dimensional problem not amenable to analytical treatment [40]. In Bayesian analysis, we seek to characterize the posterior probability distribution. The idea is to draw random samples from this distribution, where a sample corresponds to a point in parameter space. This is always possible as long as we know how to compute the likelihood of individual samples. With increasing sample size, the sample distribution will approximate the posterior distribution; in the limit of infinitely many samples, the two distributions become identical (up to a proportionality factor).

A *Markov chain* is a sequence of random samples $\Theta(1), \Theta(2), \Theta(3), \ldots$ where the k-th sample $\Theta(k)$ only depends on the value of the previous sample $\Theta(k-1)$. For example, a random walk generates a Markov chain. MCMC methods approximate the posterior distribution by performing numerous random walks in parameter space. To ensure that the distribution of walker positions converges to the posterior distribution, the walkers should visit regions of high posterior probability relatively often, while proportionally less frequently visiting regions of low posterior probability. This is achieved by *acceptance-rejection sampling*, which we here exemplify with the popular *Metropolis algorithm*.

In the Metropolis algorithm, a walker advances from the position $\Theta(k)$ to $\Theta(k+1)$ under the following rules [41]:

- Propose, by some chosen means, a new position Θ' in the vicinity of $\Theta(k)$.
- Draw a random number x from a uniform distribution on $[0, 1)$.

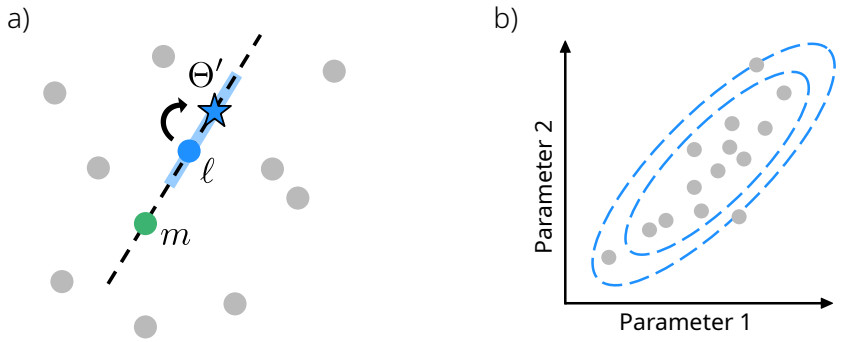

Figure 2.2: Stretch moves in the Goodman and Weare algorithm a) A stretch move for the ℓ-th walker (blue dot). The proposed position (star) lies within the blue shaded interval ($a = 2$) on the straight line connecting walkers ℓ and m (green dot). Grey dots symbolize other walkers not participating in the move. b) Stretch moves effectively deal with correlated parameters by directing the walkers such that they trace the shape of the posterior distribution (blue dashed contour lines).

- Compare the posterior probabilities of the current and proposed positions. If

$$x < \frac{P(\Theta'|\mathcal{D})}{P(\Theta(k)|\mathcal{D})} ,$$

  accept the proposed move and set $\Theta(k+1) = \Theta'$. Else, reject the move and set $\Theta(k+1) = \Theta(k)$.

This way, the walker always accepts the move if the proposal is more probable than its current position, but it sometimes also accepts moving to a less probable position (with probability proportional to the ratio $P(\Theta'|\mathcal{D})/P(\Theta(k)|\mathcal{D})$). We iterate the procedure until the chain of walker positions converges to the target distribution.

In principle, we could sample the parameter space by letting one walker stroll around for a long time. This is inefficient and entails the risk of getting stuck in a local maximum. Several independent walkers, initialized at different positions, could reduce this risk. Alternatively, more sophisticated solutions such as *parallel tempering* exist which explore the parameter space more thoroughly[4]. Nonetheless, the situation becomes tricky when model parameters are strongly correlated, since this can result in skewed posterior distributions that are stretched in one direction and squeezed in another. This would force a Metropolis walker to make small steps, leading to long convergence times. How can we avoid this?

The Goodman and Weare algorithm. MCMC simulations with several simultaneous walkers also work when the walker positions depend on each other. Goodman and Weare elegantly exploit this fact, presenting an efficient algorithm that can deal with highly skewed target distributions and nonlinear correlations (GW10, [42]). The algorithm is widely used in astrophysics, particle physics, and other fields. Since we will employ the GW10 algorithm later in this thesis, we briefly summarize its workings.

Consider an ensemble of N_W walkers, $\{\Theta_1, \Theta_2, \ldots, \Theta_{N_W}\}$, defining an ensemble Markov chain. Note that the subscript labels the walker here; for any $\ell \in \{1, \ldots, N_W\}$ the walker position Θ_ℓ is a vector of N_Θ dimensions. A step in the Markov chain comprises one

[4]For an introduction to the technique of parallel tempering, which we omit here for the sake of brevity, we refer to [37] and [41].

update cycle through all walkers. If we pick out a certain walker ℓ at the t-th step, the current positions of all other walkers define the *complementary ensemble* $\Theta_{[k]}(t)$,

$$\Theta_{[k]}(t) := \{\Theta_1(t+1), \ldots, \Theta_{\ell-1}(t+1), \Theta_{\ell+1}(t), \ldots, \Theta_{N_W}(t)\} \ .$$

The trick is now to determine the move $\Theta_\ell(t) \to \Theta_\ell(t+1)$ based on the other current walker positions. Goodman and Weare suggest a *stretch move* (see fig. 2.2), which randomly selects one walker $\Theta_m \in \Theta_{[k]}(t)$ from the complementary ensemble ($m \neq \ell$) and proposes a new position according to

$$\Theta_\ell(t) \to \Theta' = \Theta_m + Z\Big(\Theta_\ell(t) - \Theta_m\Big) \ . \tag{2.27}$$

Here the random variable Z is drawn from the distribution[5]

$$g(z) \propto \begin{cases} \frac{1}{\sqrt{z}} & \text{if } z \in \left[\frac{1}{a}, a\right] \\ 0 & \text{otherwise,} \end{cases} \ , \tag{2.28}$$

where $a > 1$ can be tuned for performance and is typically set to $a = 2$. The proposed move $\Theta_\ell(t) \to \Theta'$ is accepted with probability p,

$$p := \min\left\{1, \ Z^{N_\Theta - 1} \frac{P(\Theta'|\mathcal{D})}{P(\Theta_\ell(t)|\mathcal{D})}\right\} \ , \tag{2.29}$$

in which case $\Theta_\ell(t+1) = \Theta'$. Otherwise, we set $\Theta_\ell(t+1) = \Theta_\ell$.

The stretch move causes the walkers to explore the parameter space together, spreading out in a way that traces the topography of the posterior probability landscape. For example, if the posterior distribution is squeezed in one direction and stretched orthogonally, the walkers will increasingly sprawl in the stretched direction. Future stretch moves will then make larger steps in the stretched direction and smaller steps in the squeezed direction, ensuring fast convergence.

The Goodman and Weare algorithm satisfies *affine invariance*, which means that the sampling is invariant to affine coordinate transformations in the parameter space. Affine invariant algorithms are efficient regardless of how strongly correlated the parameters are, because in principle we could transform to new, uncorrelated parameters, sample in that parameter space, and finally transform back. The stretch move in GW10 essentially performs this transformation automatically [41].

[5] This particular choice of g fulfills symmetry requirements for the Markov chain to satisfy detailed balance. Other distributions have the same property.

3 Background

This work concentrates on the interactive interface between two complex, non-linear dynamical systems: the ocean and the atmosphere. Our goal will be to model how the ocean surface responds to the atmosphere. But as we will see, this is impossible without also considering the dynamics within the upper ocean. Furthermore, the motivation for our study results from the need to plug the response of the sea surface back into an atmospheric model, in order to investigate how the atmosphere responds to precisely the surface condition it affected. To provide a background, the present chapter takes a tour from the atmosphere to the air-sea interface and into the upper ocean.

3.1 Understanding convective organization

It is increasingly recognized that clouds play a critical role in the climate system. At the same time, their response to a changing climate is not well understood [4]. In short, if we don't understand clouds, we may not understand climate change. In this section, we aim to draw a picture of the complexity of tropical convection and the scientific challenges that come along with it. As we will see, atmospheric processes in the tropics are intimately connected to air-sea interactions and the properties of the sea surface. Hence we could say: if we don't understand air-sea interactions, we may not understand clouds.

3.1.1 What is convection?

When you heat a pot of water on a hot plate, the water near the bottom warms first. Due to thermal expansion, this water becomes less dense than the colder water above, increasing available potential energy. The warm, buoyant water begins to rise, converting potential into kinetic energy and transporting heat upwards. At the same time, conservation of mass requires that the rising water is replaced by some of the colder water which flows downwards and converges below the updraft. The result is a turbulent overturning motion called *convection*.

Let us idealize the situation above by considering a fluid, such as water or air, confined between two heat-conducting plates whose surface normals are parallel to the gravity vector. If the bottom plate is warmer than the top plate, a temperature and density gradient will form. The fluid's viscosity acts to maintain this gradient (dissipation), while gravity acts against it (buoyancy) [43]. Beyond a critical temperature difference ΔT_c between the plates ($\Delta T = T_{\text{bottom}} - T_{\text{top}}$), the fluid becomes instable, and convective overturning sets in. This setup describes *Rayleigh-Bénard convection*, for which the instability condition can be written down as

$$R := \frac{\alpha g d^3}{\nu \kappa} \Delta T \geq R_c = 1708 \ . \tag{3.1}$$

Here R is the *Rayleigh number*, defined in terms of the thermal expansion coefficient α, gravitational acceleration g, the distance d between the plates, the kinematic viscosity ν and the thermal diffusivity κ.

Despite the simplicity of this system, Rayleigh-Bénard convection shows very interesting nonlinear behavior. At Rayleigh numbers larger than R_c but not so large that the flow is fully turbulent, convective cells emerge spontaneously, breaking the symmetry and forming heterogeneous spatio-temporal patterns [43]. In other words, the velocity field self-organizes in order to facilitate vertical heat transport.

Of course, convection does not only occur in cooking pots and between imaginary parallel plates. It is a ubiquitous phenomenon of fluid dynamics that plays a major role in oceanography, meteorology, astrophysics, and engineering. While Rayleigh-Bénard convection under controlled laboratory conditions exhibits rather regular circulation cells, the complexity of the real world leads to fascinatingly diverse patterns of convection.

3.1.2 Tropical convection, clouds, and climate

In the Earth's atmosphere, convection influences weather and climate on a vast range of spatial and temporal scales. Convection is as important for the occurrence of extreme rainfall during a localized thunderstorm as it is relevant for the low-frequency variability of the global circulation and the Earth's energy budget. Why do rain forests envelop the equator, while large deserts scatter over the subtropics? How do hurricanes form, and why do some places drown in floods whereas others suffer from drought? Understanding convection is key to answering these questions.

Atmospheric convection differs substantially from the examples introduced above because it strongly depends on an additional quantity: moisture. Besides re-distributing heat, atmospheric convection mediates the water cycle through the moisture transport, condensation, precipitation, and re-evaporation of water. Meteorologists call this *moist convection* to highlight the distinction from dry convection, where moisture effects such as phase changes of water are absent.

Warm air can hold more water vapor than cold air. This is expressed by the Clausius-Clapeyron equation, which relates the saturation water vapor pressure e_{sat} to the air temperature T:

$$\frac{\mathrm{d}e_{\mathrm{sat}}(T)}{\mathrm{d}T} = \frac{L(T)}{RT^2}\, e_{\mathrm{sat}}(T) \ . \tag{3.2}$$

Here L denotes the specific latent heat of evaporation of water and R is the gas constant of water vapor. Thus, when warm moist air rises in a convective updraft and cools below its saturation temperature, water vapor condenses around aerosols present in the air. This is, in simple terms, how clouds form. In fact, clouds and rainfall are so closely related to convection that cloud cover and precipitation rate are commonly used direct measures of convective activity; vice versa, convection often stands as a collective term for all the cloud formation and precipitation processes involved.

If a rain cloud precipitates, a fraction of the precipitating water re-evaporates as it falls, consuming latent heat due to the phase change. This leads to a localized pocket of cool, dense air beneath the cloud, known as *cold pool*. Inside the cloud, however, condensation

releases latent heat, causing dried air to rise even more until it loses buoyancy and typically diverges horizontally. When these air masses sink again in a convective downdraft (subsidence), they warm and become even less saturated with moisture. Broadly speaking, moisture therefore mainly circulates in regions of convective updrafts, while dry conditions persist in areas of subsidence. A defining trait of moist convection is its asymmetry: updrafts are horizontally confined to small regions featuring high vertical velocities, wheres subsidence with small negative vertical velocities extends over large areas.

Hadley circulation. With this knowledge, we can explain the latitudinal distribution of rain forests and deserts. Similar to the overturning in a cooking pot, a giant circulation cell called *Hadley Cell* extends from near the equator to roughly 30°N, mirrored by a similar cell in the southern hemisphere. In the latitudes of highest solar insolation, warm and moist air rises. Large cloud clusters form, producing strong rainfall able to sustain rain forests. After rising to 10 to 15 km altitude, the air moves poleward until it sinks as dry air over the subtropics. There, the arid conditions promote deserts. The circulation is closed by equatorward convergence near the surface, where the air picks up moisture again.

The tropical precipitation belt where hot air converges and rises is known as the *Intertropical Convergence Zone* (ITCZ). Owing to the Earth's obliquity, its latitudinal position shifts seasonally along with the annual oscillation of the subsolar point[1]. In addition, the ITCZ exhibits more complex variability such as north-south asymmetry and regional patterns which meander with interannual to decadal variability. It is generally understood that these spatiotemporal variations of the ITCZ are closely related to the distribution of sea surface temperature (SST), which regulates the energy exchange between the ocean and the atmosphere [44]. A change in SST patterns can cause the location of the ITCZ to adapt accordingly. Interestingly, general circulation models (GCMs) often have difficulties with accurately simulating the ITCZ. Owing to errors in the simulated SST field, GCMs often feature a double ITCZ (one convergence zone on either side of the equator, instead of just one slightly north), which in turn leads to further discrepancies between the real world and the simulated world of a global climate model [45]. This example highlights that accurately modeling SST can be essential for an accurate description of the atmosphere.

As a consequence of the Hadley circulation, the tropics are a region of high convective activity featuring some of the most intense rainfall on Earth. This makes them particularly interesting for studying convective organization. Indeed, a view from space (see fig. 3.1) shows that the subtropics remain largely cloud-free, while complex cloud clusters of various structures and sizes appear around the equator. Large cloud fields also occur at higher latitudes but their structure seems less fragmented and more immediately shaped by the large-scale circulation. In the following, we will concentrate on the tropics.

Madden-Julian Oscillation. Tropical convection exhibits organization across scales. On intraseasonal time scales, the dominating mode of variability is known as the *Madden-Julian Oscillation* (MJO). It was first described in the early 1970s by Madden and Julian,

[1]The subsolar point describes the latitude where the sun's light rays hit the Earth at a perpendicular angle, i.e. where the sun crosses the zenith, for a given day of the year. It is located on the northern hemisphere during boreal summer and on the southern hemisphere during boreal winter, intersecting the equator at the equinoxes in March and September.

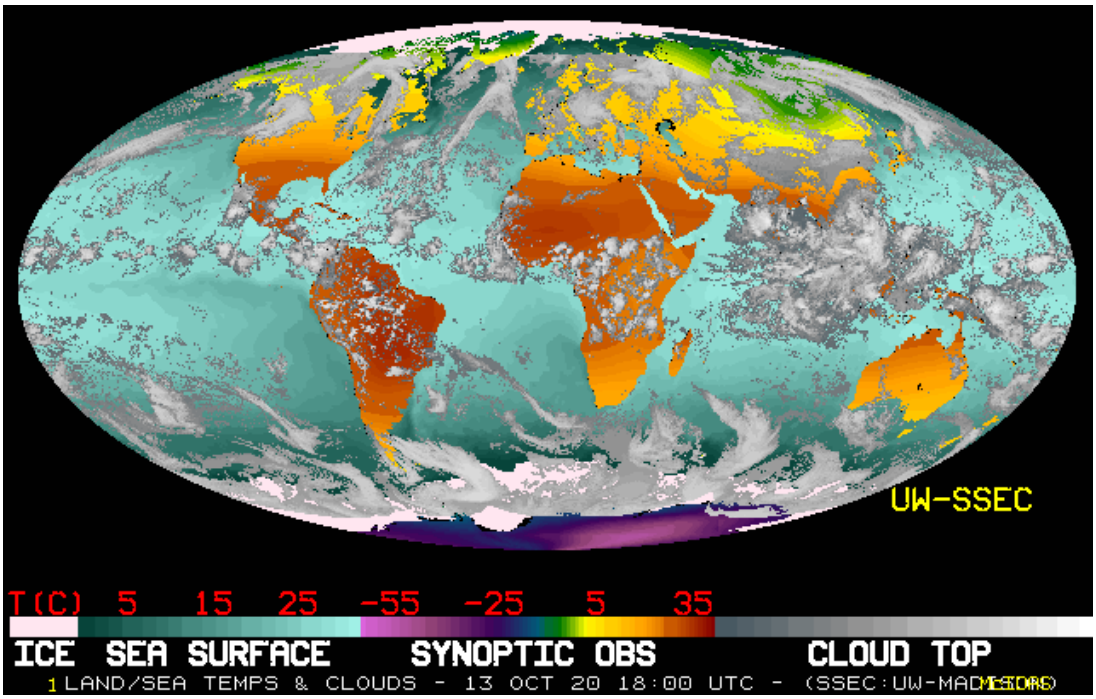

Figure 3.1: A satellite view of the global cloud field. While the subtropics are largely cloud-free, the tropics show complex patterns of cloud organization and clustering across several scales. Image source: https://www.ssec.wisc.edu/data/comp/cmoll/, also inspired by [5].

who observed a recurring pattern in precipitation and wind variability over the tropical Indian Ocean and Western Pacific Ocean [46]. An MJO event lasts about 30 to 90 days. The pattern consists of a zone of strong deep convective activity, sandwiched by extended low-convection regions to the east and west, which together propagate eastward at speeds of around $5\,\mathrm{m\,s^{-1}}$ [47].

The MJO serves as a prime example for multiscale interaction, since its rather localized convection center couples to the large-scale circulation and influences weather across thousands of kilometers. Observational studies reveal interactions with many other features of atmospheric dynamics such as the El Niño Southern Oscillation (ENSO) or the Asian monsoon systems. Importantly, the MJO appears to be strongly linked to sea surface temperature and the diurnal cycle of SST [47]. Not only does the MJO predominantly emerge in regions of high SST, it has also been proposed that diurnal warming during the inactive phase of the MJO can act as a trigger for the next active phase [48].

Even though intensively studied, the Madden-Julian Oscillation remains very difficult to model in numerical simulations. This indicates a potential deficit in our understanding of the underlying physical mechanisms, or possibly an inadequate parametrization of unresolved processes. Given that the MJO is a coupled ocean-atmosphere phenomenon, it seems crucial to accurately represent the ocean surface when studying large-scale convective organization in numerical models of the atmosphere.

Mesoscale convective systems and cold pools. Another characteristic of tropical convection is its tendency to form *mesoscale convective systems* (MCSs). An MCS is a clustered group of thunderstorms, spanning an area on the order of $100 \times 100\mathrm{km}^2$ [49]. This mode of organization is closely associated with extreme rainfall and the genesis of

tropical cyclones (hurricanes). Our capability to understand and model the dynamics of MCSs may thus be essential in order to predict tropical weather extremes in a changing climate.

Recently, the research community has intensified its interest in the role cold pools play for the self-organization of clustered convective systems. After forming during the re-evaporation of precipitation, cold pools sink rapidly and are forced to spread horizontally as they hit the ground. This causes gust fronts of cool air at the edge of the expanding cold pool. At locations where two or more cold pool gust fronts collide, warmer air masses are pushed upwards, initiating new convective updrafts. Following this argument, cold pools could organize the cloud and moisture fields by triggering convection in the vicinity of previous convective events – a process which favors aggregation. On the other hand, cold pools also counteract convective aggregation by distributing moisture from wet regions to dry regions and reducing buoyancy [50, 51]. To our knowledge, it is not clear how the gust fronts of cold pools interact with the evolution of SST.

A clouded view of climate change. The spatiotemporal pattern of clouds and convection not only modulates weather but also has important implications for climate. For example, clouds impact the planetary energy budget by influencing the Earth's albedo. A higher cloud cover fraction increases the mean albedo because cloud tops are more reflective to incoming shortwave radiation than the sea or land surface below (unless the surface is covered with ice). In this way, clouds can act like a sun shield. At the same time, they also act like a blanket by trapping longwave radiation. If clouds were to cluster more in a warmer climate, this could introduce a negative feedback, since there would be more extended clear-sky regions where outgoing longwave radiation can escape to space. Conversely, an increased cloud cover could either lead to more or less cooling, depending, for example, on the height of the cloud tops [3]. Overall, the connection between climate change and clouds remains blurred, which relates back to the question of climate sensitivity posed at the beginning of this thesis.

3.1.3 Convective self-aggregation in cloud-resolving simulations

To date, the resolution of global climate models is typically too coarse to resolve cloud processes such as convective updrafts and precipitation. This means that the net effect of cloud dynamics must be parametrized and incorporated in an averaged sense. The output of the climate models can thus be sensitive to the choice of parametrization. In order to improve parametrizations, we require a deep process understanding of convective organization. This is where idealized, conceptual models come into play.

Large-eddy simulations, or cloud-resolving models, allow to explicitly study clouds at high resolution. By idealizing the modeling setup, e.g. by choosing homogeneous boundary conditions, one hopes to simulate processes that can be dissected and understood. A paradigmatic example in idealized simulations of the tropical atmosphere is radiative-convective equilibrium, where the incoming radiation is balanced across the domain by outgoing radiation and the boundary surface is imposed with a constant, homogeneous surface temperature [8].

Radiative-convective equilibrium (RCE) has been studies intensively, accumulating insight into cloud-radiative feedbacks and cloud-cloud interactions. A fascinating feature of RCE

is that the cloud field self-organizes into a state of *convective self-aggregation*, where the convective activity is clustered in a small fraction of the model domain and the rest of the domain is dry and cloud-free [7, 6]. Historically, RCE simulations have been conducted at a relatively high horizontal resolution of 4 km. Convective self-aggregation, however, seems to break down in RCE simulations in the realistic limit of fine model resolution [13]. By contrast, recent simulations indicate that a diurnally oscillating surface temperature can facilitate aggregation at high resolution, albeit by different mechanisms [12]. This raises the question in which way convective self-aggregation is connected to the real world, or whether it is a numerical curiosity. A key disparity between RCE simulations and the real world is the assumption of a constant, uniform SST. The simulations with an imposed cycle of SST, as well as simulations imposing spatial SST inhomogeneities, suggest that air-sea interactions under a responsive sea surface may not be negligible [15]. This has sparked a renewed interest in a better representation of air-sea interactions in idealized atmospheric simulations.

3.2 Towards more realism: Air-sea interactions

A quick glance at fig. 3.2 evidences that the assumption of a non-interacting air-sea interface does not live up to reality. The previous section has shown that the ocean influences the state of the atmosphere. Conversely, the atmosphere also drives many ocean processes. This two-way interaction implies that we may not be able to understand the dynamics in either of the two subsystems unless we consider the coupled ocean-atmosphere system.

3.2.1 Surface fluxes

The sea surface acts as the responsive interface through which the ocean and atmosphere communicate. Understanding this communication means to understand the fluxes of momentum, heat, moisture, gases, and particles across the interface[2]. As we describe these exchange processes in the following paragraphs, the sea surface temperature will appear repeatedly as a key variable governing air-sea interactions.

Momentum transfer. When wind blows over the sea surface, it exerts a shear force on the water surface. This frictional force sets the water in motion and leads to the formation of wind waves. As a result, momentum is transferred across the air-sea interface, since the kinetic energy gained by the water is lost by the air. We may describe this transfer of momentum and energy with the *wind stress* $\boldsymbol{\tau}$, defined as the shear force per unit area. A common bulk formula for wind speed reads

$$\boldsymbol{\tau} = \rho_a C_D \boldsymbol{u}|\boldsymbol{u}| \ , \tag{3.3}$$

where ρ_a denotes the air density, $\boldsymbol{u}$ is the horizontal wind velocity vector (usually at a reference height of 10 m above the surface), and C_D is known as the drag coefficient. In

[2]In addition to the references cited, this section draws from the lecture material of the courses *Physical Oceanography* by Pål Isachsen and Kai Christensen at the University of Oslo (attended in 2017) as well as *Ocean Dynamics and the Carbon Cycle* by Markus Jochum and Katherine Richardson at the University of Copenhagen (attended in 2020).

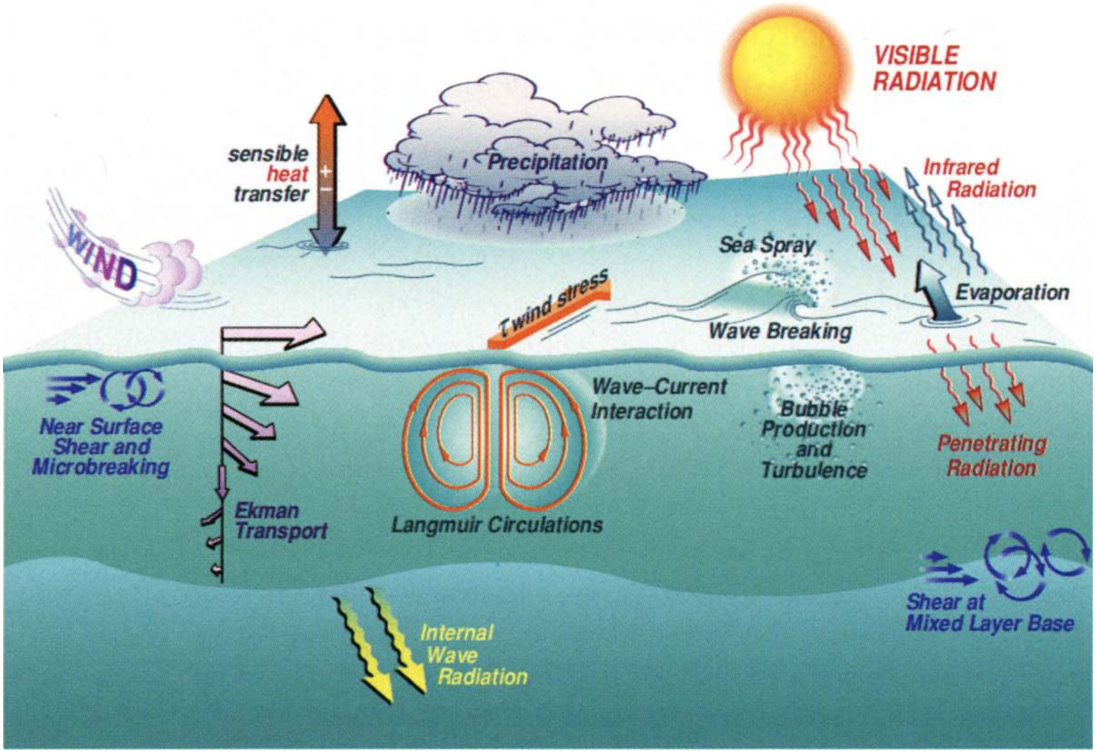

Figure 3.2: Schematic illustration of the variety of dynamical processes involved in air-sea interactions. Figure reproduced from [52].

reality, the drag coefficient is not constant but depends on the present conditions, such as wind speed, roughness of the sea surface, and even air-sea stability, which in turn depends on the air-sea temperature difference and moisture fluxes [53]. Therefore the drag coefficient can vary significantly both in space and time; its parametrization remains an active topic of research. For our purposes, we simply note that the magnitude of the wind stress is approximately proportional to the square of the wind speed.

Heat fluxes. The ocean and atmosphere exchange heat in several ways. Let us write the total heat flux Q as the sum of individual contributions,

$$Q = R_{\mathrm{sw}} + R_{\mathrm{lw}} + Q_{\mathrm{s}} + Q_{\mathrm{l}} \; . \tag{3.4}$$

Here R_{sw}, R_{lw}, Q_{s}, and Q_{l} represent the *shortwave*, *longwave*, *sensible*, and *latent* heat flux, respectively [54]. Q measures the transfer of thermal energy per unit time per unit area, normally expressed in $\mathrm{W\,m^{-2}}$. While different sign conventions exist, we define all heat fluxes such that they are positive when pointing downwards (i.e. positive Q means the ocean gains heat). As we will see, the first two terms are purely radiative, whereas the last two involve turbulent heat transport.

Shortwave radiation emitted by the sun makes up the largest heat source in the ocean [55]. The term includes direct and scattered downward irradiance at frequencies ranging from the ultraviolet to near-infrared regime. Although some of the incoming solar radiation gets absorbed or reflected in the atmosphere, the irradiance spectrum arriving at the sea surface still resembles that of a black body (as given by Planck's law, see section 4.1). If we integrate over all frequencies, approximately $1360\,\mathrm{W\,m^{-2}}$ of solar irradiance reach the

Earth at the top of the atmosphere. Peak values at the sea surface can amount to around 1000 to 1100 $\mathrm{W\,m^{-2}}$ on a clear day in the tropics.

The shortwave heat flux exhibits a pronounced diurnal cycle owing to the rotation of the Earth, as well as an annual cycle caused by the axial tilt of the rotation axis. Furthermore, clouds have an important effect on the surface heat budget by blocking incoming solar radiation.

Due to the low reflectance of sea water, most of the incoming shortwave radiation passes the sea surface. As it penetrates the upper ocean, scattering and absorption lead to an attenuation of radiation with increasing depth. This is described by the extinction law [55], which states the change of irradiance $\Gamma(z)$ with depth z as

$$\frac{\mathrm{d}\Gamma}{\mathrm{d}z} = \alpha\Gamma \ , \tag{3.5}$$

where $\Gamma(0) \equiv R_{\mathrm{sw}}$ and the z axis is oriented upwards, pointing out of the ocean (zero at the surface). Hence the radiance decays exponentially with the *attenuation coefficient*, or extinction coefficient, α. In principle the attenuation coefficient depends strongly on the wavelength of the incoming radiation, as well as on the optical properties of the sea water which may depend on depth. Integrated over all frequencies, most of the radiation gets absorbed within a few meters from the surface. While ultraviolet light penetrates only tens of centimeters, visible light reaches deeper; but at 100 m depth barely any light remains. Biological activity and inorganic particles also have an impact on light attenuation. For instance, phytoplankton effectively absorbs blue light, leading to a green or yellow water color and more heat absorbed near the surface.

The ocean loses heat by emitting *longwave*, or thermal infrared, radiation to the atmosphere. Following the *Stefan-Boltzmann law*, this heat loss is proportional to the fourth power of the sea surface temperature. In the same way, however, the atmosphere radiates heat downwards into the ocean, according to its temperature near the air-sea interface. The difference between oceanic and (downward) atmospheric emittance determines the net longwave heat flux R_{lw}. By assuming that we may approximate the ocean and atmosphere as two grey bodies[3], the Stefan-Boltzmann law yields

$$R_{\mathrm{lw}} = \sigma_{\mathrm{SB}}\left(\varepsilon_a T_a^4 - \varepsilon_w T_s^4\right) \ , \tag{3.6}$$

where σ_{SB} is the Stefan-Boltzmann constant; T_a denotes the air temperature (typically measured at some reference height 2 to 10 m above the sea surface) and T_s is the sea surface temperature (measured directly at the surface). The effective emissivities ε_w and ε_a could in principle factor in effects of cloud cover and water vapor in the atmosphere [56]. Unlike shortwave radiation, longwave radiation gets fully absorbed within the first micrometers below the surface; thus longwave heat exchange truly occurs at the ocean skin.

Sensible and *latent heat fluxes* arise from turbulent heat exchange at the air-sea interface. The former describes direct thermal conduction across the interface in the presence of a temperature difference. For example, if the sea surface is warmer than the air above, it will heat the air that comes in direct contact with it. Conversely, a warmer atmosphere heats

[3] A grey body is an idealized emitter of electromagnetic radiation, similar to a black body but with reduced emissivity $\varepsilon < 1$. For a black body, $\varepsilon = 1$ by definition.

the ocean skin. The efficiency of this heat exchange depends on the level of turbulence in the near-surface flow. This is because turbulent eddies bring "fresh" air to the interface, counteracting the conductive equilibration of temperature and allowing for enhanced heat transport. In general terms, the sensible heat flux is given by [57, 58]

$$Q_\mathrm{s} = \rho_a c_{p,a} \overline{w'T'} \ , \tag{3.7}$$

where ρ_a is, again, the air density, $c_{p,a}$ the heat capacity of air at constant pressure, and $\overline{w'T'}$ represents the Reynolds-averaged vertical velocity-temperature covariance, or turbulent heat flux. Since $\overline{w'T'}$ is difficult to measure, the following bulk parametrization is often used in practice:

$$Q_\mathrm{s} = \rho_a c_{p,a} C_s U \left(T_a - T_s\right) \ . \tag{3.8}$$

Here T_a and T_s are the air temperature and sea skin temperature as before [58], and U is the wind speed near the surface, which enters as a measure of turbulence. The coefficient C_s, known as the Stanton number, is typically assumed to be a constant.

Lastly, a latent heat flux is associated with the evaporation of sea water. Since the phase change from liquid to vapor requires latent heat, this process always cools the ocean. The rate of evaporation depends on the specific humidity of air, s_a, at some reference height above the surface, compared to the humidity s_sat of the saturated air directly at the sea surface. Similar to eq. (3.8), a bulk formula for latent heat flux Q_l is given by

$$Q_\mathrm{l} = \rho_a C_l L U \left(s_a - s_\mathrm{sat}\right) \ , \tag{3.9}$$

where L denotes the latent heat of vaporization of sea water and C_l is another exchange coefficient, the so-called Dalton number. The proportionality between Q_l and wind speed U reflects that, as with sensible heat transfer, turbulence enhances the latent heat flux. We emphasize that also the latent heat flux depends on sea surface temperature, since both the latent heat of vaporization and the saturation water vapor pressure depend on temperature (see eq. (3.2)).

Moisture flux. As mentioned above, the ocean supplies moisture to the atmosphere through the evaporation of sea water. It gains water from the atmosphere through precipitation. We can write the total moisture flux E as [57]

$$E = \rho_a \overline{w's'} + P \ , \tag{3.10}$$

where evaporation is represented by the first term containing the Reynolds-averaged covariance between vertical velocity and specific humidity $\overline{w's'}$, while P represents the moisture flux owing to precipitation. Note that to obtain a bulk formulation for evaporative moisture flux, we can simply divide eq. (3.9) by the latent heat of vaporization L. This yields the corresponding flux of water mass across the air-sea interface.

The importance of SST. From this overview of energy, mass, and momentum transport across the air-sea interface, it becomes clear that sea surface temperature (SST) is arguably the most important variable in modulating air-sea interactions. All surface heat fluxes and the rate of evaporation depend on the water temperature directly at the sea skin. By

regulating the supply of energy and moisture to the lower atmosphere, it is evident that the variation of SST can impact convection, weather, and climate [10]. At the same time, the evolution of SST is itself sensitive to oceanic and atmospheric dynamics, including the fluxes between them.

On a daily rhythm, this leads to a mode of variability known as diurnal sea surface warming. Under clear conditions, the sun heats up the upper ocean, since the water absorbs the incoming shortwave radiation. Most of the energy is absorbed in the few upper meters of the ocean. As the surface warms, a positive temperature gradient forms, which causes stable density stratification. Due to this stability, the warm water near the surface is prevented from exchanging heat with the cooler water below (except by molecular conduction, which is a very slow heat transfer process). In effect, heat gets trapped near the surface, and the sea skin warms considerably. After the sun has passed its highest point, the incoming solar heat source decreases. At the same time, the outgoing longwave, sensible, and latent heat fluxes increase because of the higher sea surface temperature. Thus the upper water layer loses heat and eventually becomes colder than the water below, causing instable density stratification. Consequently, the water masses start to mix vertically in an overturning motion, and some of the heat that was trapped near the surface is transported downwards.

In the presence of wind, we also have the wind stress $\boldsymbol{\tau}$ which generates shear at the surface, pushing the water masses to mix despite stable stratification. In effect, the evolution of diurnal SST is determined by the competition between the stabilizing effect of stratification and the destabilizing effect of wind forcing. To understand diurnal warming, we must not only understand the heat exchange across the air-sea interface, but also the turbulent mixing of heat downwards into the water column.

3.2.2 Turbulent diffusion in the upper ocean

Turbulence in the upper ocean has a net effect of mixing water masses. In general, the vertical heat transfer contribution from turbulent mixing is written as

$$\left(\frac{\partial T}{\partial t}\right)_{\text{turb}} = -\frac{\partial \overline{w'T'}}{\partial z} \ , \tag{3.11}$$

where again the covariance of the vertical velocity w and the temperature T, or turbulent heat flux $\overline{w'T'}$, appears. To the lowest-order approximation, the turbulent heat flux may be parametrized as "down-gradient", i.e.

$$\overline{w'T'} = -\kappa_{\text{turb}} \frac{\partial T}{\partial z} \ , \tag{3.12}$$

such that turbulent mixing is described as diffusion with the turbulent diffusivity κ_{turb}. The turbulent diffusivity of sea water is typically several orders of magnitude larger than the molecular diffusivity κ_{mol}, in which case $\kappa = \kappa_{\text{turb}} + \kappa_{\text{mol}} \approx \kappa_{\text{turb}}$.

3.3 A review of diurnal SST modeling

Based on a cross-disciplinary literature review, we identify two somewhat disconnected fields with an interest in the modeling of SST variability. Loosely speaking, we might

describe the first group as the near-surface oceanographers, who have been modeling upper ocean processes and air-sea interactions at various levels of complexity for many years. On the other side, there is the active field of idealized numerical atmospheric modeling, where the interest in SST variability has recently intensified. In the following, we provide a condensed overview of SST modeling from both perspectives.

3.3.1 Models of upper ocean temperature variation

Various models have been developed over the last fifty years to simulate the diurnal variability of temperature in the near-surface ocean. Conceived for different purposes such as satellite calibration, air-sea flux estimation, or the study of boundary layer dynamics, these models differ in design and level of realism. Following a systematic review by Kawai and Wada [10], we identify three overall categories. The first category comprises *turbulent boundary layer models*, which explicitly resolve turbulent mixing processes. Secondly, *bulk or slab models* take a more idealized approach based on simplifying assumptions. *Empirical models* that deduct functional relations from observational data form the third general category.

Turbulent boundary layer models. The most direct physics-based way of determining upper ocean dynamics is to solve the equations of motion and thermodynamics that govern momentum, temperature, and salinity[4]. Models based on this principle have been proposed e.g. by Kondo et al. (1979) [25], Mellor and Yamada (1982) [26], Large et al. (1994) [16], and Kantha and Clayson (1994) [27]. These models differ in the way they treat turbulence. For example, Kondo et al. as well as Large et al. parametrize vertical eddy transport by introducing a stability-dependent eddy diffusivity based on a *Richardson number* criterion and *Monin-Obukhov similarity theory*.

In contrast, rather than parametrizing turbulent mixing semi-empirically, the Mellor-Yamada model and its further development by Kantha and Clayson use turbulence closure at second or higher order. Other turbulence closure models include the Noh model [28, 59], which accounts for turbulent mixing due to wave breaking and Langmuir circulations. It has been coupled to an atmospheric weather forecasting model [60]. An alternative way to parametrize turbulent transport is known as the transilient method, which describes mixing by a spectrum of eddies of different scales [61].

Studying diurnal SST variability is just one possible application of these models, as they more generally describe boundary layer dynamics in geophysical systems. Their ability to simulate SST has been successfully tested against observational data on different time scales, though the representation of turbulent heat transport remains imperfect [62, 10].

Bulk or slab models. The complicated nature of turbulent mixing dynamics has motivated researchers to develop more simplified models of diurnal SST variation. Bulk or slab models partition the upper ocean into one or several layers, imposing certain assumptions on the dynamics within and between layers.

[4]Typically the hydrostatic approximation is assumed, which replaces the vertical component of the momentum equations by an expression for the vertical pressure dependence.

A widely used candidate is a multi-layer model by Price et al. (1986) called the PWP model [17]. The authors assume the existence of a surface *mixed layer* in which vertical temperature, density and velocity gradients are negligible, connecting to a transition layer of stratified fluid below. The depth of the mixed layer changes in time; its evolution is determined based on the energy and momentum budget inside the mixed layer using a bulk Richardson number criterion. Basically, wind forcing deepens the mixed layer while strong surface warming resets it. While the mixed layer is numerically implemented as a *dynamic instability model* (DIM) [63], an additional mixing process in the transition layer avoids discontinuities in the gradients.

If all we are interested in is the evolution of skin SST, vertical profiles do not matter as long as the surface is modeled accurately. This idea underlies further simplified models such as the F96 model by Fairall et al. (1996) [29]. F96 essentially reduces the PWP model to a single-layer version; fluxes are evaluated as bulk integrals over the layer depth which again evolves according to a Richardson number condition. The bulk calculations yield a temperature gradient which is imposed as a linear temperature profile throughout the warm layer. Furthermore, the authors add a thin, cool skin layer at the air-sea interface where the temperature gradient is governed by molecular conduction. Refinements to the F96 model have been proposed by Gentemann et al. (2009) with their POSH model [30]. Among other changes, it includes a more sophisticated absorption model of shortwave solar radiation.

Zeng and Beljaars (2005) [31] present a prognostic scheme which imposes a somewhat more realistic shape of the temperature profile: rather than a linear depth dependence they propose a power law with an empirically determined exponent. This allows writing down an evolution equation for the difference between the skin temperature (defined at the bottom of the cool skin layer) and the foundation temperature where the diurnal variation vanishes (set to 3 m in their study). Similar to Large et al. [16], turbulent mixing is parametrized by an eddy diffusivity derived from Monin-Obukhov similarity theory. Takaya et al. (2010) [64] later added refinements such as increased mixing owing to Langmuir circulations.

Empirical models. A number of models derive relations between SST variation and meteorological quantities empirically, that is, by fitting a parametric function to data. Some models specialize to estimating the amplitude of diurnal warming (difference between daily maximum and minimum SST), including Webster et al. (1996) [32], Price et al. (1987) [34], and Kawai and Kawamura (2002) [33]. The input quantities, such as solar radiation, wind speed, and precipitation, are typically required as daily averaged values. For example, Webster et al.'s model takes the form

$$\mathrm{d}SST = f + aR + bP + c\ln(U) + dP\ln(U) + eU \ , \tag{3.13}$$

where R is the peak solar radiation ($\mathrm{W\,m^{-2}}$), P is daily mean precipitation ($\mathrm{mm\,h^{-1}}$), U is the daily mean wind speed (at 10 m height, in $\mathrm{m\,s^{-1}}$), and the coefficients a, b, c, d, e, f are determined empirically.

To make statements about the SST variation over the course of the day, Li et al. (2001) [65], developed approaches to deduct hourly values from the above formula (3.13) [10]. Further empirical models for hourly evolution of the SST cycle were proposed, e.g. by Zeng et al. (1999) [35] and Gentemann et al. (2003) [36].

In summary, models for upper ocean SST variability exist in various shapes and forms, from turbulence-resolving dynamical equations to single-layer slabs. Many have been successfully applied and tested, though no model is perfect. Full turbulence closure models come closest to reality. Bulk models perform differently well depending on the situation and their level of simplification, often showing a systematic under- or overestimation of surface warming [10]. Empirical models face the issue that their accuracy depends strongly on the underlying dataset, and often a fixed set of parameters only holds for a limited range of input variables.

3.3.2 Slab ocean models in idealized simulations of the atmosphere

In the context of atmospheric modeling, slab ocean models typically refer to a single-layer bulk model with a fixed specified slab depth. Surface fluxes are integrated vertically to obtain the slab's temperature response, for example:

$$\frac{\mathrm{d}T_{\mathrm{slab}}}{\mathrm{d}t} = \frac{1}{\rho_w c_p h}\Big(Q_{\mathrm{sw}} + Q_{\mathrm{lw}} + Q_{\mathrm{s}} + Q_{\mathrm{l}} - Q_{\mathrm{ocean}}\Big) \,. \tag{3.14}$$

Here ρ_w and c_p are the density and heat capacity of sea water, respectively. The first four Q terms on the right-hand side denote shortwave, longwave, sensible, and latent heat flux as before (positive Q means downward flux, into the ocean). Furthermore, Q_{ocean} represents the heat lost from the slab to the deep ocean. This term is particularly important under tropical conditions, where the ocean absorbs on the order of $100\,\mathrm{W\,m^{-2}}$ averaged over a year. Without it, the slab temperature would become too warm. An alternative approach to deal with the excess heat is described by the slab equation

$$\frac{\mathrm{d}T_{\mathrm{slab}}(x,y)}{\mathrm{d}t} = \frac{F(x,y)}{\rho_w c_p h} + \frac{T_{\mathrm{target}} - \langle T_{\mathrm{slab}}\rangle}{\tau} \,, \tag{3.15}$$

where the slab temperature now depends on the horizontal grid position (x, y) in the simulation domain and $F(x, y)$ is the net heat flux, abbreviating the four Q-terms in eq. (3.14). The second term relaxed the domain-mean slab temperature $\langle T_{\mathrm{slab}}\rangle$ to a target temperature T_{target}, at a relaxation time scale τ This ensures that the mean slab temperature does not drift, while allowing for spatial inhomogeneities which are not directly affected by the temperature relaxation. This type of slab model has been used, for example, by [23].

It appears that there is a gap between the rather sophisticated upper ocean models proposed in the ocean modeling literature and the highly simplified single-layer slab models employed in idealized atmospheric simulations. We argue that the slab models in eqs. (3.14) and (3.15) are too simple to adequately capture the evolution of SST under air-sea interactions. This motivates our aim to develop a model that could fill the gap. In the next chapters, let us climb up one rung on the ladder of complexity.

4 Observations

This chapter presents an observational study of diurnal sea surface warming in the tropical ocean. It will lay the foundation for the subsequent model development, allowing for comparison and calibration. To our knowledge, large parts of the present analysis have not been conducted before.

4.1 Measuring sea surface temperature

Sea surface temperature, or SST, refers rather loosely to the temperature of sea water near the surface. This can mean different things, depending on the method of measurement.

From buckets to buoys. Beginning in the late 1700s, seafarers collected water with buckets to measure its temperature aboard with a thermometer. With the advent of steam engines, ships began to monitor the temperature of the cooling water entering the engine room. After the 1950s, the number of SST records grew rapidly and became more systematic. Instruments such as CTD (conductivity-temperature-depth) profilers, submerged below the surface, allowed to measure sea temperature directly in the water. Data from moored buoys complemented shipborne observations from the 1970s onward, soon followed by drifting buoys. In fact, by 2010 around 90 percent of in situ SST measurements originated from moored or floating buoys [66].

Looking down from space. The revolutionary introduction of satellites in Earth observation offered a new way to monitor SST with global coverage (see fig. 4.1). Satellites employ infrared or microwave radiometers to infer SST from the electromagnetic radiation emitted by the ocean surface. For a black body, the relationship between emitted spectral radiance $R(\nu)$ and temperature T is governed by Planck's law,

$$R(\nu) \propto \left(\exp\left\{ \frac{h\nu}{k_B T} \right\} - 1 \right)^{-1} , \tag{4.1}$$

where ν denotes the frequency and h and k_B are Planck's and Boltzmann's constants, respectively. Note that in the low-frequency limit ($\nu \to 0$) the radiance becomes approximately proportional to temperature (Rayleigh-Jeans law). While the ocean surface is a gray rather than a black body, we can calculate its temperature from Planck's law if we know the ocean's emissivity [67].

Infrared radiometers capture radiance at wavelengths of $\sim$ 1 to 10 µm, the "infrared window". In this range, radiation does not penetrate clouds very well, such that infrared radiometers require clear sky conditions to produce appropriate SST estimates. By contrast, microwave radiometers are capable of "looking" through clouds. They operate

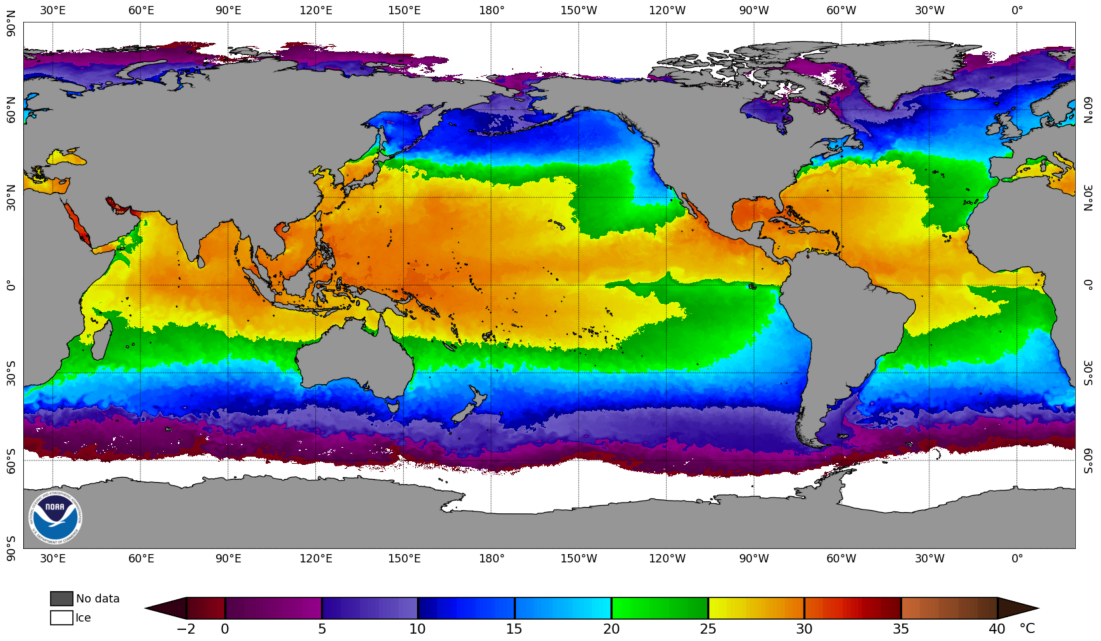

Figure 4.1: Satellite-derived global sea surface temperature (SST) on August 9, 2021, as observed at 5km resolution by the CoralTemp product of NESDIS. The tropics exhibit extended regions of warm SST above 25°C. Note that this snapshot shows typical characteristics of tropical SST, such as the Western Pacific Warm Pool (high SST near the maritime continent) and the "cold tongues" of cool SST wiggling along the equator in the Eastern Pacific and west of Central Africa. Image source: NOAA Coral Reef Watch [68].

with frequencies on the order of 1 to 10 GHz, which experience little attenuation by cloud droplets [69]. A downside of microwave radiometers is that their SST estimation depends on the roughness of the sea surface, as caused by waves or spray. In any case, the atmospheric composition, specifically of aerosols, affects the quality of satellite-derived SST, and during rain events remote sensing surface temperatures becomes impossible.

Need for calibration. The temperature derived from satellite observations corresponds to the water temperature at the penetration depth of the corresponding electromagnetic waves. In the microwave window, the penetration depth is less than a centimeter, whereas for infrared radiation it even decreases to a few micrometers [67, 70]. Hence satellites truly measure the temperature of the sea *skin*. For buoys, the situation is very different. Moored buoys typically have thermometers installed at different depths; SST is then defined as the temperature of the upper-most thermometer, usually located somewhere between tens of centimeters to ten meters below the surface. Drifters often have their temperature sensor roughly a meter beneath the air-sea interface.

It thus becomes clear that SST measurements from different methods are not directly comparable and entail different biases. This presents a challenge for climate science. For example, bucket measurements on ships tend to yield a higher SST than buoy data. When ship records were increasingly supplemented by buoy records over the years, this induced a bias which has been identified as a partial explanation for an apparent slowdown of global warming at the beginning of the 21st century [71, 72]. Indeed, the calibration of SST data is a field of research in itself and has motivated many field campaigns as well as modeling efforts.

4.2 The data base of this thesis

The atmosphere "feels" the ocean skin. Air-sea exchanges of energy, specifically the sensible, latent, and longwave heat fluxes, are governed by the temperature of the interfacial skin layer. Therefore, it is interesting to take a detailed look at radiometric data, since they directly show the skin SST.

4.2.1 Ship data: The MOCE-5 cruise

The primary dataset for our subsequent modeling study originates from a research cruise that took place in 1999 off the Mexican west coast[1]. More specifically, the *Fifth Marine Optical Characterization Experiment* (MOCE-5) cruise was conducted from October 1-21, 1999 aboard the research vessel *Melville* [73]. The ship started its observations in the Eastern Pacific near San Diego, California and traveled southeast along Baja California (see fig. 4.2a). In the second week, the cruise led into the Gulf of California up to the Midriff Islands, while the third week was used to return towards San Diego along the west coast.

Throughout the cruise, a combination of meteorological, oceanographic, and radiometric sea skin temperature data were collected. The meteorological and oceanographic data include wind speed, incident solar irradiance, air temperature, and sea water temperature at a depth of 3 m. Additionally, the on-board operation of the infrared radiometer M-AERI provided precise temperature measurements of the sea skin. M-AERI stands for *Marine-Atmospheric Emitted Radiance Interferometer*. The instrument records emission spectra in the range of 3-18 µm at a resolution of around 0.5 cm^{-1}, leading to an accuracy of deduced temperature of 0.03 K [74].

Figure 4.2b shows that the vessel stopped at different locations to measure at a fixed position. Generally, the vessel moved at night and halted during daytime (with exceptions). However, data were collected regardless of whether the boat moved or not, and quantities such as wind speed and direction were corrected for the ship's motion. Simultaneous measurements of the above quantities are available every 11-12 minutes with several gaps in between.

A highlight of this dataset is that it provides in situ radiometric measurements of the sea skin, which are sparsely available. However, the study area of the MOCE-5 cruise lies slightly north of the tropics and predominantly in coastal waters. This motivates us to gather additional data from the equatorial Atlantic and Pacific Oceans.

4.2.2 Buoy data: Global Tropical Marine Buoy Array

Since the 1980s, the U.S. National Oceanic and Atmospheric Administration (NOAA) operates a collection of moored buoys across the tropical oceans, forming the *Global Tropical Marine Buoy Array* (GTMBA) [75]. It consists of the programs TAO (Pacific), PIRATA (Atlantic), and RAMA (Indian Ocean). A map of all buoy locations is depicted in fig. 4.3.

[1]The dataset was kindly provided by Peter Minnett.

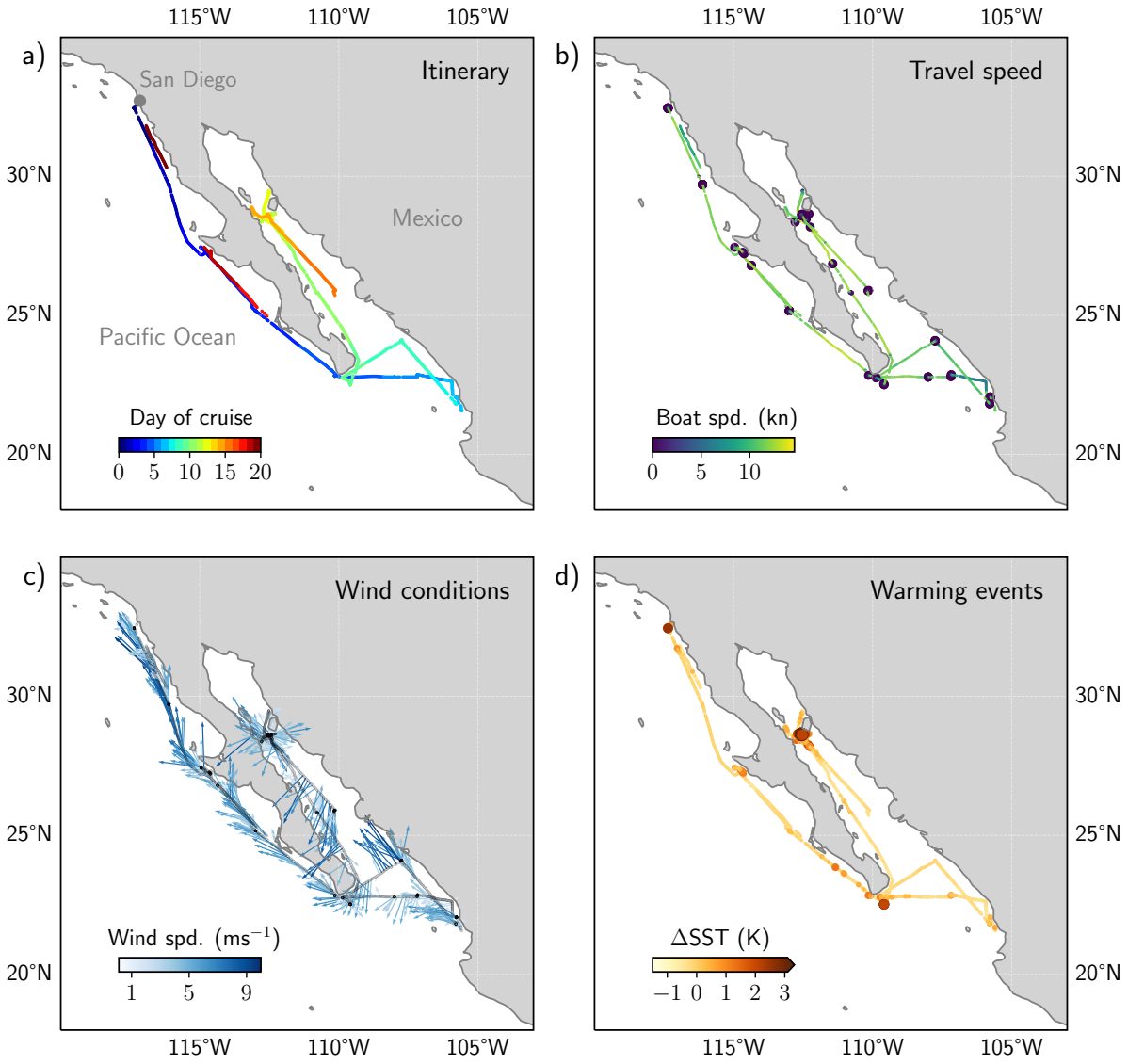

Figure 4.2: The MOCE-5 cruise, October 1999. The first panel (a) shows the travel route of the research vessel *Melville*, colored by days since departure in order to visualize the chronology of the cruise. (b) provides an overview of the stops taken during the voyage by plotting the ship's speed in knots, where the point size is inversely proportional to the speed. Large dark points thus indicate the locations where the ship essentially halted. (c) illustrates true wind speed and direction (arrows pointing into the wind); (d) shows observed surface warming (ΔSST), where data points are colored and sized according to the magnitude of warming.

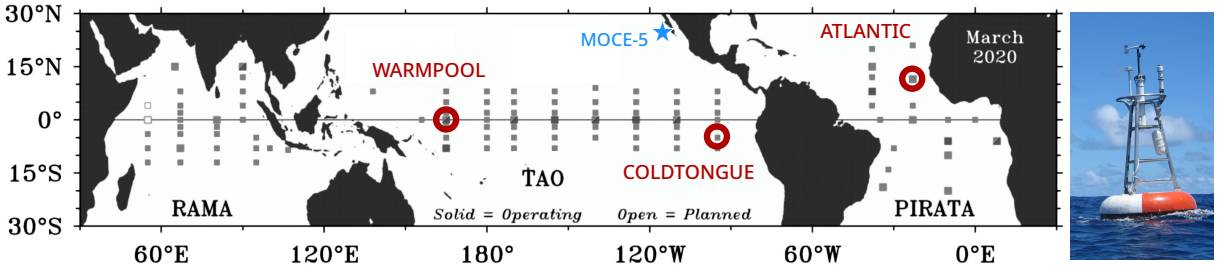

Figure 4.3: Map of the Global Tropical Marine Buoy Array extending over the Indian, Pacific, and Atlantic Oceans. Grey squares indicate the buoy positions. In this study, we use data from three buoys marked by the red circles and labeled by their reference names. The blue star indicates the study area of the MOCE-5 cruise. (Map adopted from [75] with modifications.) *Right:* Photograph of one of the buoys, type ATLAS. (Image source: [76])

Buoy reference name	Location	Data used	resolution
WARMPOOL	00°N 165°E	SST(1m), T(5m), T(10m), wind	10 min
COLDTONGUE	05°S 095°W	SST(1m), T(5m), T(10m), wind	10 min
ATLANTIC	12°N 023°W	SST(1m), T(5m), T(10m), wind	10 min

Table 4.1: Specifics of the buoy data used.

The GTMBA buoys record a wide range of meteorological and oceanographic quantities at time intervals from several minutes to hours. We are mainly interested in near-surface sea temperature measurements at different depths, together with wind speed, solar irradiance, air temperature, and air humidity. SST is measured at 1 m depth, corresponding to the temperature sensor closest to the surface. The next thermometers further down are mostly located at 5 m and 10 m depth, respectively.

To allow for an insight into regional variability, we focus on three buoys at different locations around the globe (see fig. 4.3 and table 4.1). We select these buoys as single samples from different SST regimes, based on the map of yearly averaged SST displayed in fig. 4.1. The first buoy – which we label WARMPOOL – lies on the equator at 165°E, within a region of high SST known as the Western Pacific Warm Pool. On the eastern side of the Pacific, we choose the buoy at 5°S and 95°W, located in an area of comparatively cold SST characterizing the Pacific Cold Tongue (COLDTONGUE). Third, we select one buoy in the Atlantic, off the coast of Western Africa where large mesoscale convective systems advect from the land to the ocean and tropical cyclones are suspected to emerge (ATLANTIC, 12°N 23°W). All these locations are of research interest regarding the influence of air-sea interactions on atmospheric dynamics.

For these three buoys, we download sea temperature and wind speed data from the last twenty years, recorded at a sampling interval of 10 minutes. However, the time series are not continuous, as not all instruments were operational throughout.

4.2.3 Additional data

The combination of radiometric skin temperature data with buoy data at 1, 5, and 10 meters depth allows for limited insight into the depth dependence of diurnal warming. However, it is not clear in which way the two datasets may be linked, since they originate from different locations at different times. To attain a better understanding of vertical

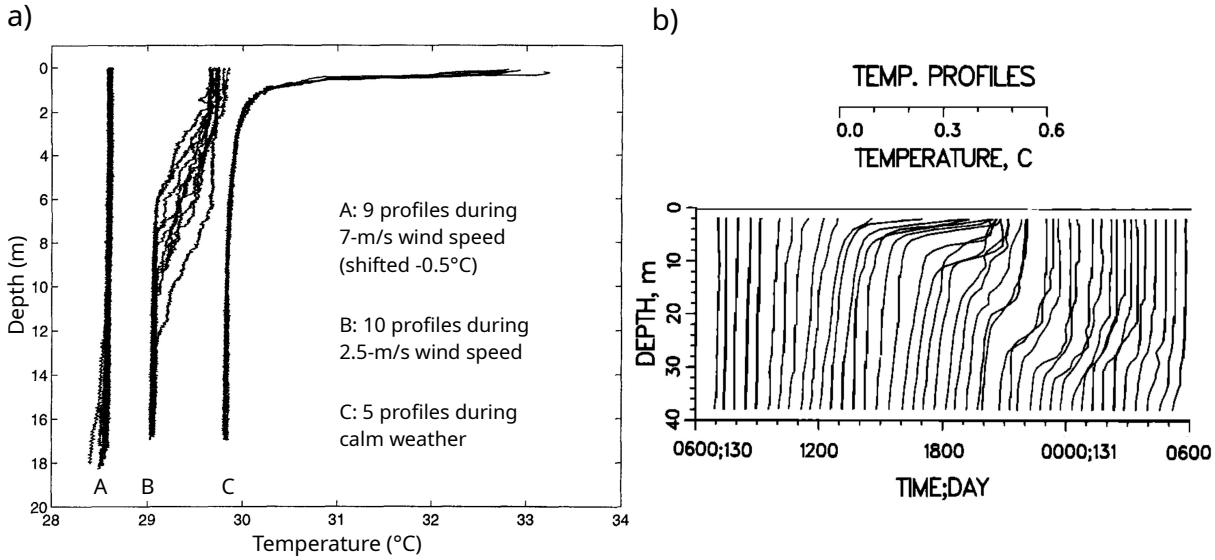

Figure 4.4: Observed vertical temperature profiles of diurnal warming. (a) shows a collection of profiles at different wind speeds, measured during afternoon hours with a free-rising profiler in the Western Pacific. The data were obtained in 1994 aboard the *Moana Wave* as part of the TOGA Coupled Ocean Atmosphere Response Experiment. Adopted from [18], with enlarged labels for readability. (b) depicts a time series of CTD profiles recorded on the vessel *Flip* in spring 1980 in the Eastern Pacific, a few hundred kilometers off the Californian coast. The bottom of each profile indicates its time of observation. From [17], with modifications.

temperature profiles under diurnal warming, we refer to observed profiles reported by Soloviev and Lukas [18] as well as Price et al. [17], shown in figs. 4.4a and 4.4b, respectively. To our knowledge, these data are not available in numeric form, but we will use the figures as visual points of reference. Their origin is described in the figure caption.

4.3 Data preparation and analysis

Equipped with a million observations of diurnal SST warming, we are ready to begin our analysis.

Preliminaries. Both the cruise and buoy datasets consist of raw data stored in several files. This necessitates a careful conflation of different variables into synchronized time series. For example, during the MOCE-5 cruise the meteorological data were sampled at a higher frequency compared to the radiometric skin temperature measurements. To combine the two, we develop an algorithm that finds the closest meteorological data point for each radiometric data point. Then, the algorithm checks whether the corresponding times lie more than 10 minutes apart. If they do, that data point is discarded. We also omit a few data points where the GPS position of the radiometric dataset differs substantially from that of the meteorological data at the same time. This may be superfluous because the radiometer is mounted on board the ship, but we could not establish whether these cases were due to an erroneous position or a false time stamp. Furthermore, the time coordinate of both datasets is provided in UTC. We translate from time of day in UTC to

local sun time using a simple shift by longitude:

$$t_{\text{local}} = \left(t_{\text{UTC}} + \frac{\varphi}{15}\right) \mod 24 \ , \tag{4.2}$$

where the longitude φ is inserted in degrees east and time is in units of hours. Lastly, we clean the conflated data by removing time points where at least one of the temperature values reads $-99\,°\text{C}$, indicating a missing value.

For a selected GTMBA buoy, the data come in different files for different variables with different starting dates, which we synchronize when conflating them. While the arrays contain continuous entries every ten minutes, only a fraction of these entries have numerical values, depending on when the corresponding instrument was operational. We use the functionality of masked arrays in Python to ignore empty fields, which enables convenient data processing. Like before, we convert time from UTC to local sun time based on eq. (4.2).

In the following study, we will sometimes fit a function to a collection of data points. For fitting we use the least-square optimizer of the `iminuit` package for Python [77].

4.3.1 MOCE-5 data analysis

Figure 4.5 depicts the time series of key parameters obtained from the MOCE-5 cruise dataset. In the top panel, we present the chronology of diurnal warming. The amplitude of warming ΔSST is hereby defined as the difference between the skin temperature obtained by the radiometer and the sea temperature at 3 m depth, which we refer to as *foundation temperature* T_f, i.e.

$$\Delta\text{SST} := T_{\text{skin}} - T_f \ .$$

The data points are colored by the ship's current cruising speed to indicate which measurements were recorded under drifting conditions (see also fig. 4.3b). Since the vertical grid lines along the time axis indicate midnight, we notice that the vessel mainly relocated during the night and drifted slowly during daytime. The second panel plots the absolute value of skin SST (T_{skin}) together with the air temperature, while the third panel shows wind speed (after correction of the ship's motion). Lastly, the two bottom panels display solar irradiance and the boat speed as a function of time, respectively. Overall the observation time series exhibits three larger gaps of missing data, between days 7 and 8 as well as after day 16 (of October 1999).

General description. As seen in the figure, the first week of the cruise is characterized by small to moderate warming events, reaching around 0.5 to 1 K. This coincides with a relatively windy start; only on days 6 and 7 the wind falls below $2.5\,\text{m}\,\text{s}^{-1}$ for extended periods. At the same time, SST and the air temperature rise by around 10 K as the vessel moves southward. This does not seem to imprint itself in the ΔSST signal. After a windy day 9 without significant warming, the following days show large diurnal warming events of more than 2 K and up to 5 K. Figure 4.2d) gives an overview of where these events occurred. While the day 10 event is located at the tip of the Baja California Peninsula, the vessel is inside the Gulf of California between days 12 and 16. We observe that the air temperature and SST fluctuate more within the Gulf and cool down by a few degrees as the vessel proceeds north, further into the Gulf. Note that the warming events coincide

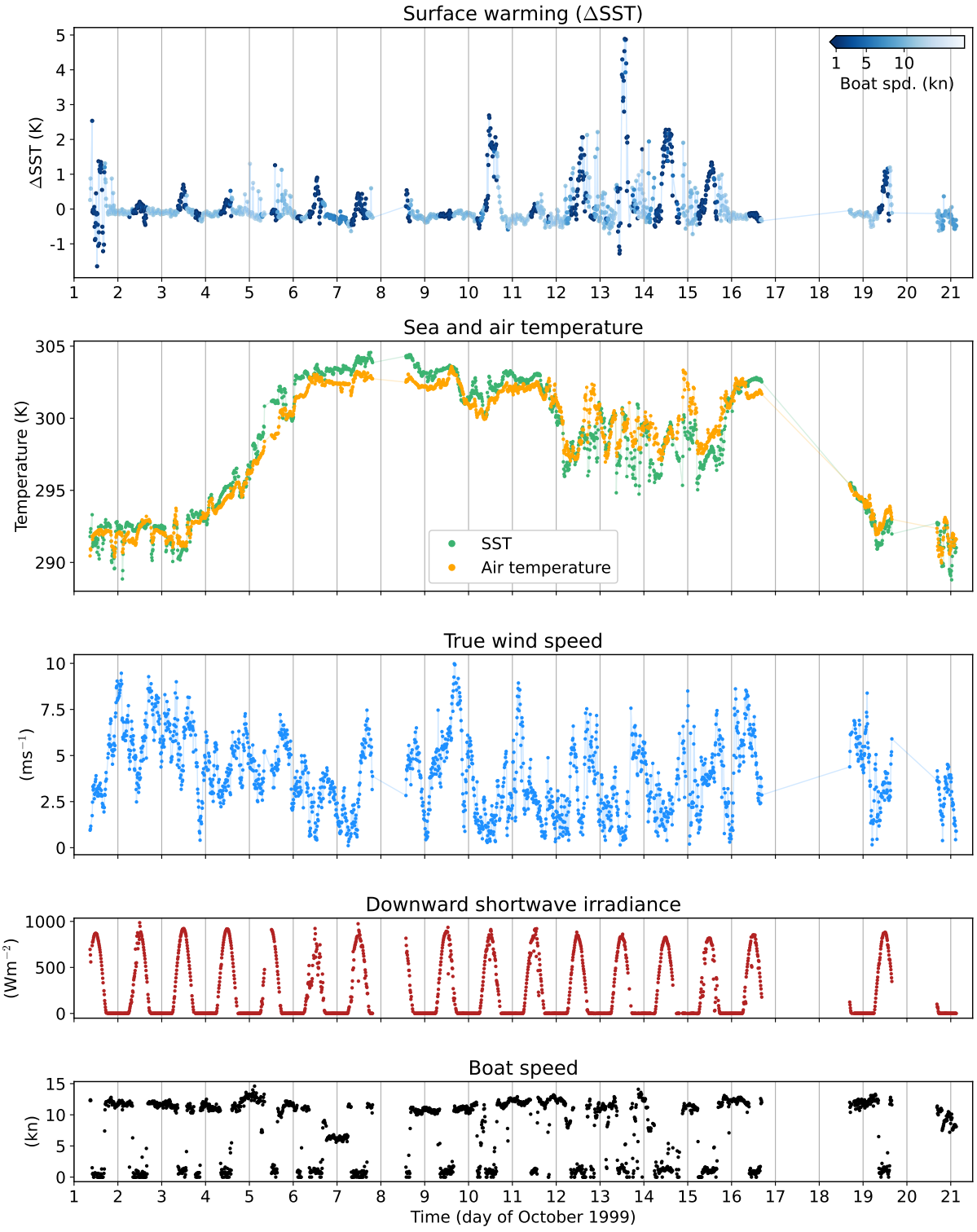

Figure 4.5: Overview of the MOCE-5 dataset. From top to bottom: Temperature difference ΔSST between the sea skin (as measured by the M-AERI radiometer) and a depth of 3 m (temperature sensor of the ship); absolute values of the radiometrically measured skin SST and of air temperature; wind speed, corrected for the ship's motion; incident shortwave irradiance; and the ship's travel speed in knots. The gaps reflect missing data.

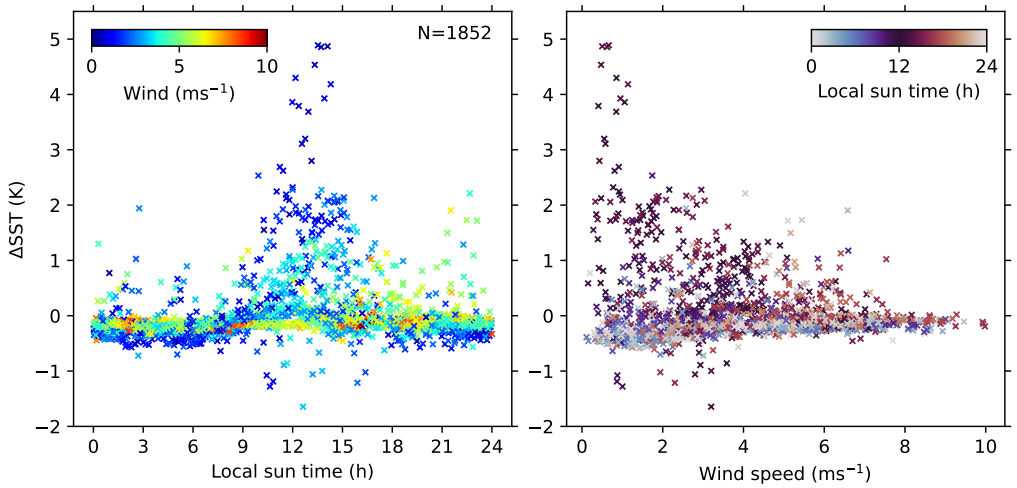

Figure 4.6: Time and wind dependence of ΔSST. Left: Scatter plot of all 1852 data triples (ΔSST, local sun time, wind speed) of the MOCE-5 data set, plotted as a function of local sun time and colored by wind speed. Right: The same data but plotted as a function of wind speed, while colored by local sun time.

with relatively low wind speeds during midday hours. Since much of the data from the final days of the cruise are missing, we merely note that there is another moderate warming event on the open Pacific side on day 19. The shortwave radiation curve frequently peaks above 800 $\mathrm{W\,m^{-2}}$ throughout the cruise, indicating dominant clear sky conditions, except perhaps on day 6.

Wind dependence. Let us analyze the properties of the observed warming events in more detail. Our aim is to distill general features of diurnal SST warming, in particular the course of the diurnal cycle and its wind dependence. As a first step, we take all 1852 data points of the time series and plot their magnitude of warming, ΔSST, as a function of local sun time. The result is depicted in fig. 4.6 (left panel), where data points are colored by their corresponding wind speed[2]. Similarly, the right panel of fig. 4.6 shows ΔSST as a function of wind speed, colored by local sun time. This presentation clearly demonstrates that strong diurnal warming events are restricted to low wind speeds. As wind increases, the skin temperature deviates less and less from the foundation temperature. However, we also observe the cool skin effect, that is, ΔSST is often slightly negative at night.

Amplitude, phase shift, skin effect. To investigate the wind dependence further, we now bin the data by wind speed and plot the resulting subsets individually, as illustrated in fig. 4.7). We fit each of these subsets with a Gaussian (with multiplicative scale factor and additive constant) as well as a Lorentzian function, or Cauchy distribution. The purpose of this is to estimate a mean time and magnitude of peak warming; we do not assume that the warming curve actually follows one of those two functional forms. We do assume by this choice that the warming and cooling is symmetric around the peak, which seems to hold reasonably well when inspecting fig. 4.7. Note that in the 5-6 $\mathrm{ms^{-1}}$ bin, diurnal

[2]This data has been presented in the same way before, see ref. [74]. The following analysis, however, is new in this thesis.

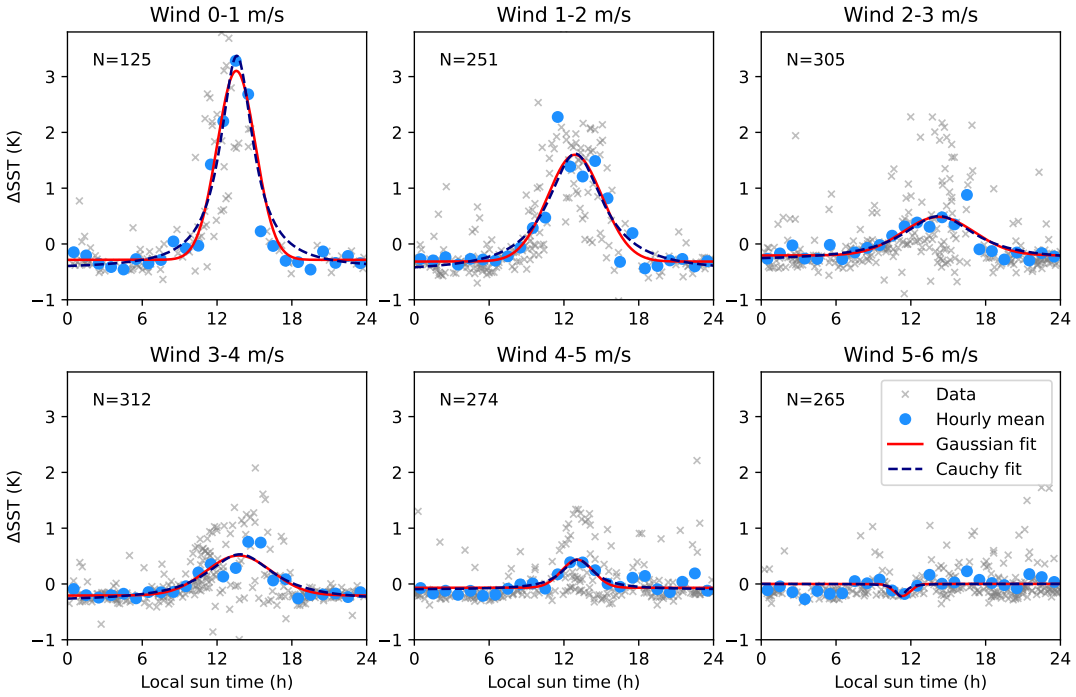

Figure 4.7: Diurnal warming binned by wind speed. Each plot shows raw data (gray crosses) and hourly averages (blue dots) of ΔSST as a function of local sun time, for a given wind range as indicated above the plot. Additionally, least-square fits of a Gaussian bell curve (red solid curve) and Lorentz-Cauchy distribution (blue dotted line) are shown.

warming is essentially absent, such that the optimizer does not find a positive peak. Since the Gaussian and Cauchy fits yield similar results, we now focus on the former.

The time and temperature coordinates of the Gaussian maxima serve as estimators of phase and amplitude of the diurnal cycle, respectively. Furthermore, the additive constant (which was included as an additional fit parameter) provides a rough estimate of the cool skin effect, since it represents the overall offset of the warming curve with respect to the foundation temperature. Figure 4.8 bundles the results for wind bins of $0.5\,\mathrm{ms}^{-1}$. The left panel confirms that the amplitude of diurnal warming decreases with wind speed. The data may suggest an exponential dependence, which we test with a least-square fit to an exponential function (gray line). This fit has a p-value of 0.25%, which is rather small yet not extremely unlikely given the scatter in the data. Next, we investigate at which time of day peak warming occurs (center panel, fig. 4.8). Here the limited number of data points makes it difficult to identify a trend. Overall, peak warming seems to occur between about 1230 and 1530 local sun time, around 30 minutes to 3.5 hours after peak solar insolation. Lastly, despite considerable scatter, the right panel in fig. 4.8 indicates a decrease in skin effect with increasing wind speed. At low wind speeds and during nighttime, we find that the skin is on average about 0.3 K cooler than the foundation temperature.

Two regimes. Due to the distinct geography of the open Eastern Pacific and the Gulf of California, which is enclosed by land on three sides, we may expect different prevalent conditions in these regions. Likewise, the water properties may differ, including optical properties and turbulent diffusivities. In fig. 4.9a), we show that we can clearly separate two regimes by plotting air temperature against foundation temperature. The colors in

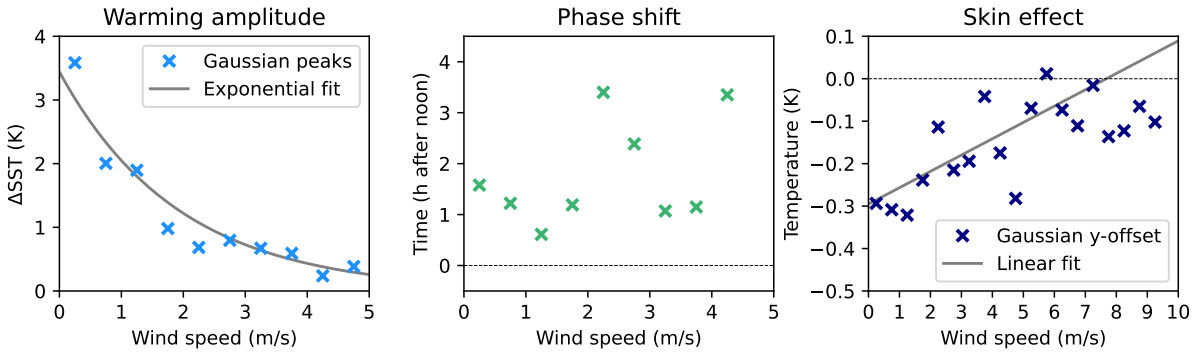

Figure 4.8: Warming amplitude, phase shift, and skin effect as a function of wind in the MOCE-5 dataset. The amplitude of ΔSST, the phase shift of ΔSST, as well as the skin effect are esimated by the peak values, peak times, and y-offsets of the Gaussian fits, respectively. The grey solid lines indicate least-square fits to the data points.

the scatter plot are based on the following simple classification: we draw an imaginary straight line from San Diego to the south-eastern cape of the Baja California Peninsula, declaring any data point south of that line as "Pacific" and any point north of the line as "Gulf".

Given this distinction, is it a coincidence that the five largest diurnal warming events of the MOCE-5 cruise occurred in the area classified as "Gulf of California"? Possibly, the Gulf of California features high concentrations of organic or inorganic particles in the upper ocean, causing strong solar absorption and heat trapping near the surface. On the other hand, the winds were stronger when the research vessel was in the open Pacific, compared to inside the Gulf. This could either be a momentary coincidence or a general trend. Moreover, stronger waves in the open ocean could cause a difference in vertical mixing. Further investigation in this direction goes beyond the scope of this study. However, we are interested whether similar warming events as observed in the Gulf of California also frequently occur in the open ocean. This leads us to the buoy data.

4.3.2 Buoy data analysis

The radiometric cruise data from MOCE-5 reveals diurnal SST warming of several Kelvin, constrained to low wind conditions. Using observations from the three buoys in table 4.1, we now test to what extent our results from the previous section transfer more generally to the tropical ocean. Recall that the uppermost temperature sensor is located at 1 m depth for all of the buoys, such that here SST$= T(1\mathrm{m})$. For this case we define the magnitude of surface warming ΔT as

$$\Delta T := T(1\mathrm{m}) - T(10\mathrm{m}) \ ,$$

where $T(1\mathrm{m})$ and $T(10\mathrm{m})$ denote the temperatures at 1 and 10 meter depth, respectively.

Annual and diurnal variability. First, let us inspect what the raw data look like. In fig. 4.10, we contrast sea surface warming on two very different timescales, as observed by the ATLANTIC buoy. The left panel illustrates the interannual variability of warming for a selected six-year interval (2010-2016). Absolute SST exhibits a clear annual cycle with an amplitude of about 5-8 K between late boreal summer and winter. Interestingly, we

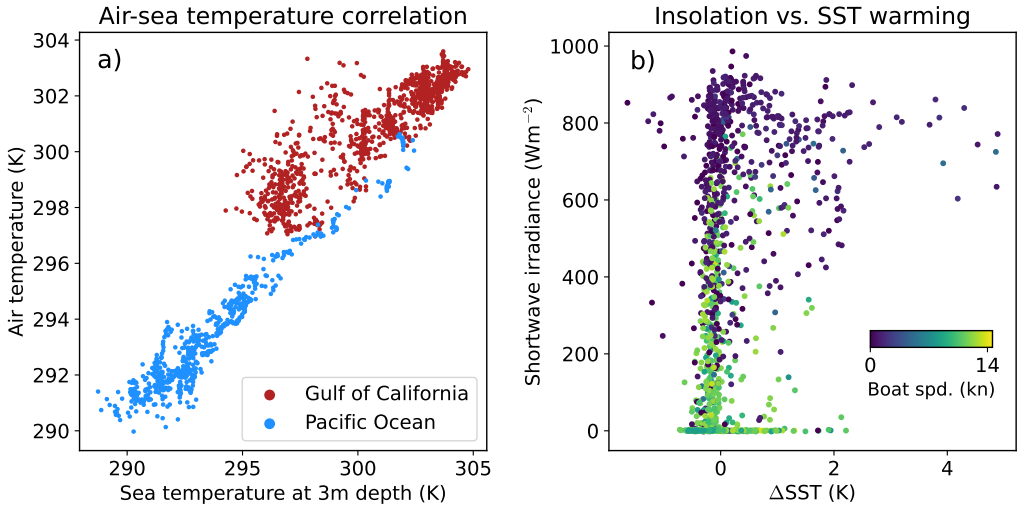

Figure 4.9: Correlations in the MOCE-5 data. Left: Plotting the air temperature against the sea foundation temperature separates the data from within and outside the Gulf of California. The points are colored as described in the main text. Right: Scatter plot of insolation as a function of ΔSST, colored by the ship's travel speed. Note that the boat speed is usually low during the day (high insolation valued) and high at night. Overall, large ΔSST requires strong insolation. However, there are also some night-time data points at zero insolation with up to 2 K of warming. We assume that these are artifacts due to currents or due to the boat cruising through waters of different temperature.

also detect an annual variation in the ΔT signal, i.e. the amplitude of diurnal warming oscillates with an annual period. More specifically, large diurnal warming events of more than 1 K appear predominantly during boreal summer, when SST is high. Several possible reasons come to mind. One of them is that the winters are windier, as shown in the bottom left panel of fig. 4.10. If the result from the cruise data analysis transfers to this case, strong winds inhibit warming. Indeed, fig. 4.11 (left panel) demonstrates that this statement also holds for the ATLANTIC buoy. We will investigate the wind dependence at all buoy locations in detail below.

On the right side of fig. 4.10, we zoom in on a twenty-day period in 2014 to illustrate the diurnal cycle of warming. This time interval begins and ends with relatively high wind speeds, coinciding with the absence of diurnal warming. In between, we observe a period of low wind speeds where diurnal warming of up to 3 K occurs.

To confirm the visual impression of a diurnal and annual cycle in the sea temperature signals, we display the power spectrum of the full $T(1\text{m})$ and ΔT time series in fig. 4.11 (right panel). Distinctive peaks in the power spectral density of $T(1\text{m})$ show at frequencies corresponding to periods of 12 hours, 1 day, and 1 year; a monthly period does not stand out. The power spectrum of the temperature difference ΔT has similar spikes at the diurnal and 12-hour period. Though the power is suppressed in the low frequency range compared to $T(1\text{m})$, there also is a peak corresponding to a 1-year period. At the WARMPOOL buoy located on the equator, we also find a strong diurnal and 12-hour component, whereas an annual period is less distinct for $T(1\text{m})$ and ΔT (not shown). The COLDTONGUE dataset contains less data with multiple gaps, such that a spectral analysis becomes less feasible.

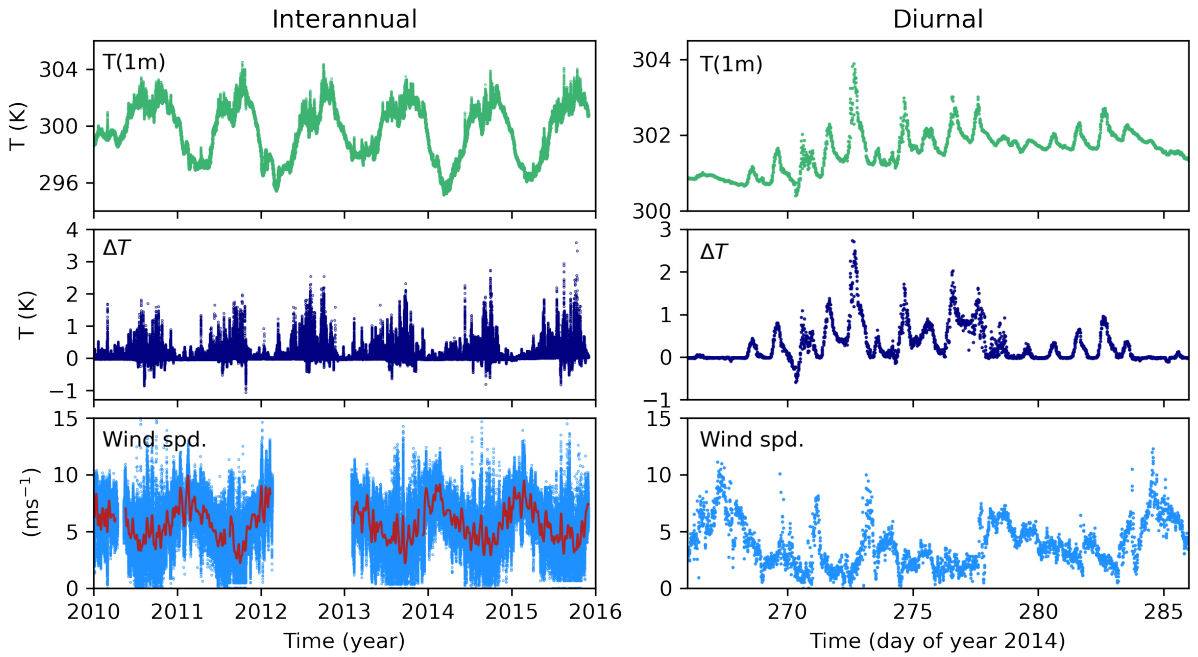

Figure 4.10: Interannual and diurnal sea surface warming. Left: Absolute SST (at 1m depth), temperature difference $\Delta T = T(1\text{m}) - T(10\text{m})$, and wind speed in an interannual time series from 2010 to 2016. Right: Zooming in on the diurnal scale, on a 20-day interval from the left time series in 2014.

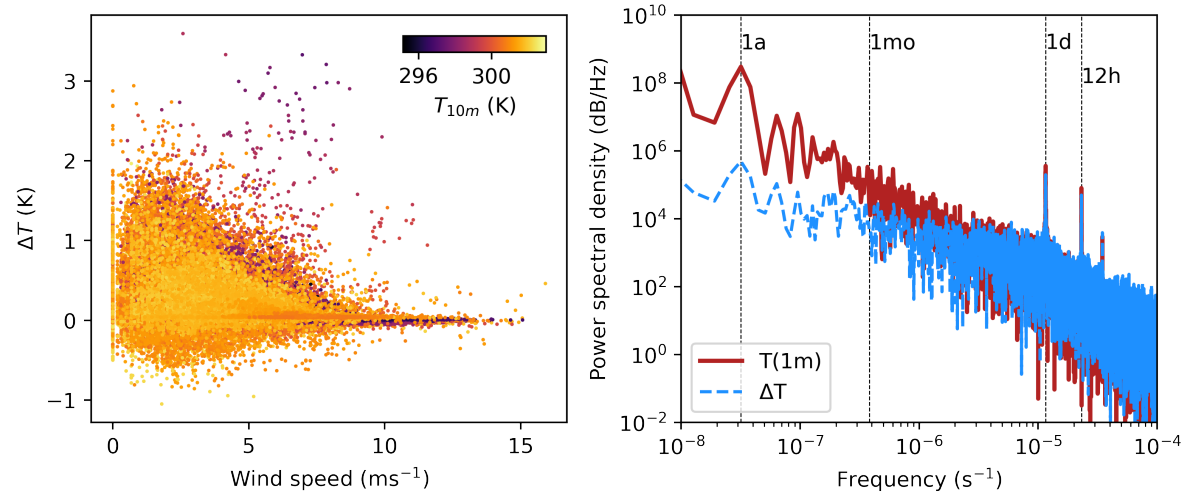

Figure 4.11: Wind dependence and power spectrum of sea surface warming. Left: Scatter plot for the ATLANTIC buoy of the temperature difference $\Delta T = T(1\text{m}) - T(10\text{m})$ as a function of wind speed, colored by the foundation temperature. Right: Power spectral density of the absolute temperature signal (T(1m), red solid line) as well as the temperature difference ΔT (blue dotted line). Frequencies corresponding to 1 year, 1 month, 1 day, and 12 hours are indicated by vertical dotted lines.

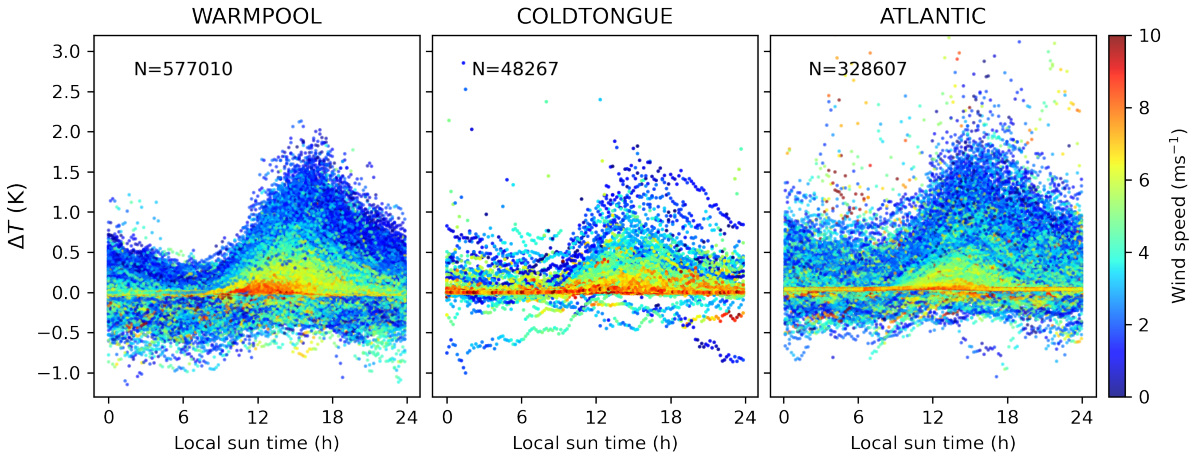

Figure 4.12: Wind-resolved warming profiles of the GTMBA buoys. The plots show the temperature difference $\Delta T = T(1\text{m}) - T(10\text{m})$ as a function of local sun time, colored by wind speed.

Diurnal warming. We now move on to a comparison of diurnal warming at the WARMPOOL, COLDTONGUE, and ATLANTIC buoy locations. As before, our goal is to study general features of the diurnal warming pattern. Figure 4.12 illustrates the time evolution and wind dependence of ΔT for each of the three locations, plotted in the same way as in fig. 4.6 for the MOCE-5 data. The three panels are remarkably similar in their overall features. At 1 m below the sea surface, warming under low wind conditions can reach up to 2 K in the late afternoon, sometimes even more at the ATLANTIC buoy. Note that low-wind data are limited for the COLDTONGUE buoy; nonetheless the wind dependence is clear.

As previously, we subdivide the data by wind speed for further analysis. Figure 4.13 depicts results for wind bins of $2\,\text{ms}^{-1}$. The blue curves represent half-hourly sample averages of $\Delta T = T(1\text{m}) - T(10\text{m})$ as a function of time. Analogously, the dark red curves show the sample averages of warming at 5 m depth, defined as $\Delta T_5 = T(5\text{m}) - T(10\text{m})$.

In agreement with the MOCE-5 observations (see fig. 4.7), the amplitude of near-surface warming generally decreases with increasing wind speed at all three buoy locations. However, we also register some differences between the buoy and cruise data. Firstly, the mean amplitude of less than 1 K is significantly smaller than the amplitude of skin SST observed during MOCE-5, which reached 3 K. Secondly, the buoy data still exhibit some warming at wind speeds between 5 and $8\,\text{ms}^{-1}$, until diurnal warming essentially disappears above $8\,\text{ms}^{-1}$. Third, compared with fig. 4.7, the 1m-depth warming curves at low winds seem further shifted towards the evening. Lastly, we note that there is no skin effect, i.e. the minimum values of ΔT and ΔT_5 are close to 0 °C.

Depth dependence. It is also interesting to compare the warming at 1m depth with the warming at 5m depth. At low wind speeds, the amplitude of ΔT is several times larger than that of ΔT_5, while the peak of ΔT occurs earlier than that of ΔT_5. At higher wind speeds, the two curves become more similar, both in amplitude and phase. In fact, the amplitude of ΔT_5 does not decrease until about $6\,\text{ms}^{-1}$. In the following, we focus on the amplitude and phase at 1m depth.

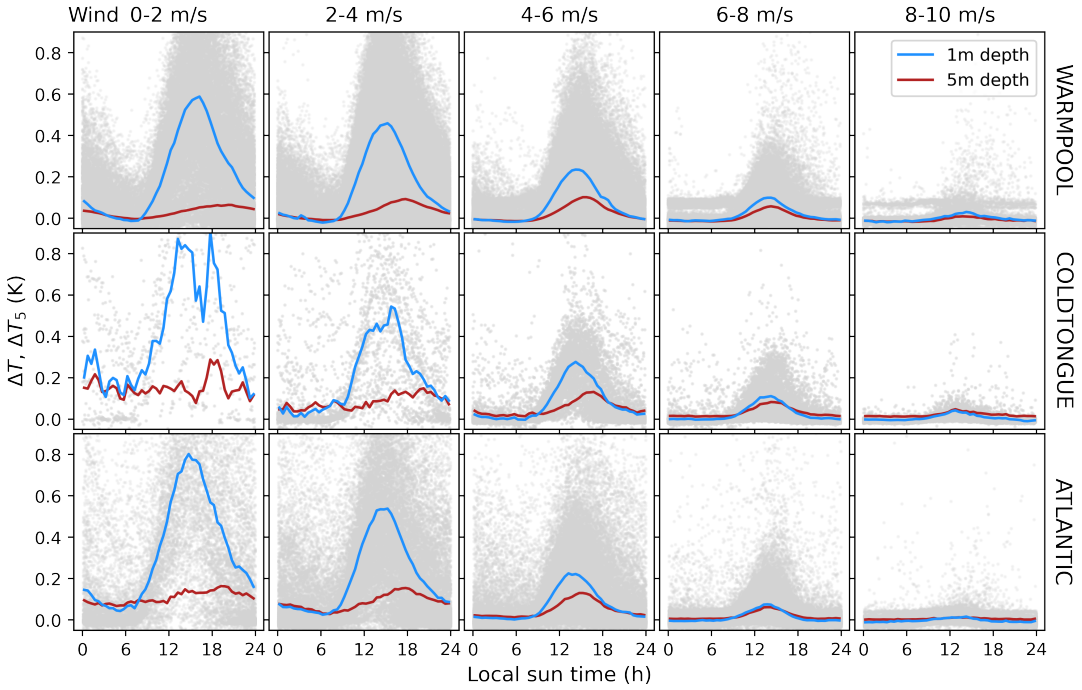

Figure 4.13: Buoy warming data, binned by wind speed. The blue lines depict the temperature difference between 1m depth and the foundation temperature at 10m depth, whereas the red lines show the temperature difference between 5m and 10m depth. Light gray points visualize the raw data. The wind intervals for each column are given at the column top. Top row: WARMPOOL, center row: COLDTONGUE, bottom row: ATLANTIC.

Amplitude and phase at 1 m depth. Let us next extract the peak values and times of the mean warming curves at 1m depth. Unlike previously in the case of the MOCE-5 data, we now have sufficiently many data points in each wind bin to use the maxima of the half-hourly means directly, rather than fitting to a Gaussian and using the Gaussian maximum as an estimate (the COLDTONGUE data at low winds poses an exception; corresponding averages should be treated with caution). Figure 4.14 combines results for all buoys, computed using wind bins of $0.5\,\mathrm{ms}^{-1}$. The left panel depicts the mean diurnal warming amplitude as a function of wind speed. Curiously, the curves seem to level at low wind speeds. Beyond $2\,\mathrm{ms}^{-1}$ wind, the amplitude decays with increasing wind speed, revealing a strong similarity between all three buoys. We perform an exponential fit on the combined data, which is shown as a solid line in the figure.

The right panel of fig. 4.14 visualizes the wind dependence of the phase shift of mean warming. Despite considerable scatter, it seems that the phase shift with respect to 1200 noon decreases with increasing wind speed. All three buoys feature this trend. Thus, on average, warming at 1m depth occurs in the later afternoon at low winds and a few hours earlier at high wind speeds.

Extrapolating to the surface. The preceding analysis has uncovered similarities and differences between the properties of diurnal warming observed during the MOCE-5 cruise and by the buoys. However, comparisons between the two datasets remain difficult due to the differing depths of the measurements. If, at a given instant, a buoy in the tropical ocean records $\Delta T = 1\,\mathrm{K}$ at 1m depth, how large is the warming precisely at the surface? We cannot answer this question definitely, but we may derive a rough estimate by extrapolating

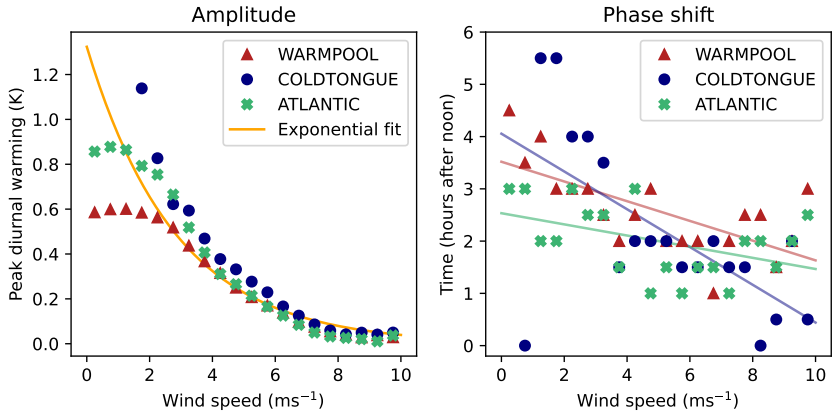

Figure 4.14: Wind dependence of the warming amplitude and phase shift as observed by the GTMBA buoys. The solid lines illustrate to least-square fits to the data.

from the three depths where we have temperature measurements (1m, 5m, and 10m). For this purpose, we concentrate on the low-wind regime of 0-2 ms^{-1}.

The simplest option would be to assume a linear vertical temperature profile. Considering the observed profiles in fig. 4.4, however, this seems an unrealistic choice. In addition, the three temperature values $T(1\text{m})$, $T(5\text{m})$, and $T(10\text{m})$ generally do not lie on a straight line in a depth-temperature diagram. As our first choice, we therefore assume an exponential shape of the profile. We motivate this by the fact that incoming solar radiation decays exponentially with water depth, constituting an exponentially decreasing heat source. For three (non-negative) data points, there exists a unique exponential function with two parameters that intersects each point. The temperature difference between depth z and the foundation temperature at $z = 10\,\text{m}$ is then given by

$$\Delta T(z; a, b) = b\left(e^{a(10-z)} - 1\right) \ , \tag{4.3}$$

where a, b are the free parameters and $z = 0$ represents the sea surface.

As a second option, we employ the power law profile proposed by Zeng and Beljaars [31] (referred to as ZB05),

$$T(z) = T_\delta - \left(\frac{z-\delta}{d-\delta}\right)^\nu (T_\delta - T_d) \ , \tag{4.4}$$

where δ represents the depth of the cool skin layer, d is the depth at which the foundation temperature is taken, and $\nu = 0.3$ is an empirical parameter. Since the skin layer is typically very thin, we set $\delta = 0$, such that T_δ represents the skin surface temperature. Then, by choosing $d = 10\,\text{m}$ and $z = 1\,\text{m}$, we can solve for T_δ using the data points at 1m and 10m depth:

$$\Delta T(z=0) = T_\delta = \frac{T(z=1) - 10^{-\nu} T(z=10)}{1 - 10^{-\nu}} \ . \tag{4.5}$$

To perform the extrapolation, we use hourly mean temperature values, averaged from all data of the WARMPOOL and COLDTONGUE buoys with a wind speed of less than 2 ms^{-1}. Each hourly mean includes those data points with local sun time within that hour. In addition to the average, we calculate the 90th percentile of each hourly data slice. We

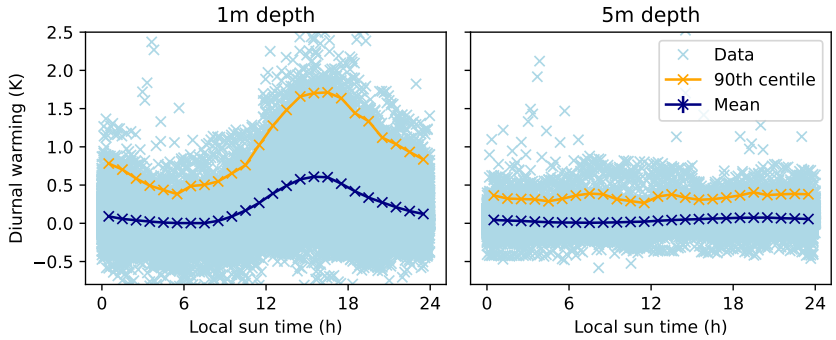

Figure 4.15: Spread of diurnal warming in the low wind regime of 0-2 m s^{-1} wind speed. Left: Temperature difference between 1m and 10m depth as a funtion of local sun time. The light blue crosses show the raw data, while the blue line shows hourly averages and the orange line shows the 90th percentile of each hour. Right: Same as the plot on the left, but showing the temperature difference between 5m and 10m.

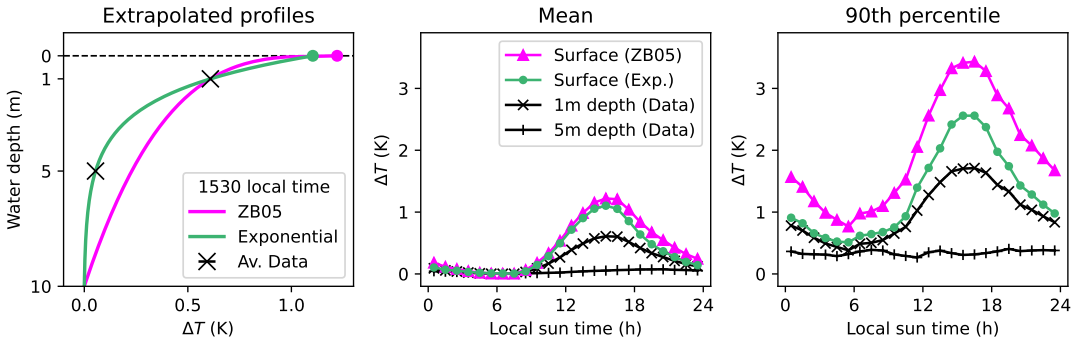

Figure 4.16: Extrapolating to the surface. Left: Two example profiles using the ZB05 and the exponential profile to fit the data, as described in the main text. The rounded ends mark the extrapolated temperature value at the sea surface. Center: Observed hourly mean ΔT at 5m depth and 1m depth, as well as extrapolated ΔT using the ZB05 and the exponential profile, respectively, as a function of local sun time. Right: Same as the center panel, but showing the 90th percentiles and using these to extrapolate to the surface.

do this because the data in fig. 4.12 show a wide spread in temperature, such that the mean warming value is not representative of the large warming events associated with up to 2 K warming at 1m depth (see fig. 4.15).

We present the outcome of the extrapolation in fig. 4.16. The left panel exemplifies the shapes of the two vertical profiles. Note that the exponential profile intersects both data points at 1m and 5m depth, whereas the ZB05 profile only uses the point at 1m depth together with the foundation temperature ($z = 10$ m). In the center panel, we show hourly sea skin temperatures extrapolated from the hourly means; the right panel displays extrapolations from the 90th percentiles. In the case of the mean, both the exponential and the ZB05 profiles yield similar results, stating that peak warming at the surface is roughly twice the peak warming at 1m depth. By contrast, if we extrapolate from the 90th percentile, the exponential profile reaches about 2.5 K at the surface, while the ZB05 profile rises to around 3.5 K.

These extrapolated surface temperatures should be regarded as rather crude estimates. Given the exponential and power law behavior of the used profiles, a small difference in the temperature values at depth can result in a large change in estimated surface temperature.

Nonetheless, the results help to get an idea of possible surface warming amplitudes at the selected buoy locations.

4.4 Features of diurnal sea surface warming

To conclude our observational data analysis, let us summarize the key findings of this chapter. Near-surface diurnal warming in the tropical ocean is characterized by the following general traits.

- At the sea skin, amplitudes of diurnal warming reach up to 5 K under low wind conditions. On average, the surface warming under clear and calm conditions amounts to around 2-3 K.
- Diurnal warming also reaches 1m depth, but here the amplitude is reduced compared to the surface. Under extreme conditions, warming can exceed 2 K at 1m depth.
- Peak warming at the sea surface occurs about 1-4 hours after peak insolation (noon), while it typically occurs later in the afternoon with increasing depth. Below the surface, the phase shift decreases with increasing wind speed.
- At 5m depth, there is little diurnal warming, with a peak typically shifted into the late afternoon.
- The magnitude of diurnal warming is strongly influenced by wind speed. Our data analysis suggests that the average diurnal warming amplitude decays exponentially with increasing wind speed. Winds of more the $5\,\mathrm{m\,s^{-1}}$ essentially prohibit any significant temperature increase at the surface.
- Depending on location, the diurnal warming amplitude may exhibit variability on longer time scales, as exemplified by the annual oscillation at the ATLANTIC buoy.

Our key modeling goals will be to capture the amplitude and the exponential wind dependence of diurnal sea surface warming. The secondary objective will be to adequately mimic the time and depth dependence of the temperature variability, such as the gradual downward-transport of heat in the hours after noon.

5 The model

In this chapter, we present an idealized model of diurnal surface warming in the tropical ocean. Forced by atmospheric conditions, the model simulates the heat transfer and temperature evolution within the first few meters below the sea surface. Our modeling approach is based on the principle of being as simple as possible, yet as complex as necessary, in order to capture the basic features of diurnal warming described in the previous chapters. To this end, we combine a physics-based approach with conceptual simplifications of the fluid dynamical processes involved. Rather than aiming for high accuracy and realism, our goal is to arrive at a model which qualifies as a generic, interactive lower boundary condition for idealized atmospheric simulations.

5.1 Conceptualizing heat transfer in the surface ocean

Let us begin by defining a simplified domain for our model. In agreement with other observations, our data analysis has shown that most of the diurnal warming occurs within the top five meters of the water column. This motivates the introduction of a theoretical *foundation depth* z_f where any atmospherically driven diurnal temperature variability vanishes. At the foundation depth, we take the water temperature to be constant in time and refer to it as the *foundation temperature* T_f. We thus assume that we can separate the scales of diurnal SST variation from the ocean's internal low-frequency variability. The foundation depth essentially partitions the water column into two layers: the *diurnal layer* between the surface and z_f, where diurnal temperature variations occur, and the *foundation layer* below z_f, acting as an infinite reservoir at temperature T_f. Moreover, since we are mainly concerned with vertical heat transport, we assume that the ocean is horizontally homogeneous. This implies that we neglect surface waves, imposing a flat sea surface. The homogeneity assumption allows us to treat the problem as a one-dimensional system.

The atmospheric forcing consists of solar radiation and the surface fluxes, which, to first order, depend on wind speed, air temperature, and air humidity. Incoming solar radiation acts as a heat source that decreases with increasing depth. Next, we need to describe how heat is transported within the domain, bounded by the sea surface and the foundation depth z_f. Our fundamental starting point is the heat equation.

To what extent is the heat equation capable of representing upper ocean heat transport under atmospheric forcing? Which minimal set of additional terms and parameters may be required to reproduce a behavior that resembles observations? These questions guide the development of our model. We already know that diurnal warming results from a competition between wind-driven turbulent mixing and near-surface heat trapping. Our data analysis suggests that including the wind dependence of mixing will be crucial. The other competing process, heat trapping at the surface, involves the formation of stable

density stratification near the surface, which counteracts vertical mixing. We will also explore how this can be incorporated in a simplified manner.

While we have an understanding of the heat fluxes at the air-sea interface, the heat exchange at the lower domain boundary z_f is a priori less clear. In addition to wind-driven turbulence, there may be non-negligible internal mixing processes. With these thoughts in mind, let us introduce the model.

5.2 Model description

We consider the sea temperature $T(z,t)$ as a function of time t and vertical coordinate $z \in [z_f, 0]$. The sea surface is located at $z = 0$, and we define the z axis to point upwards, such that $z < 0$ below the sea surface[1]. To simulate the time evolution of $T \equiv T(z,t)$, starting out from an initial condition $T(z,0)$, we propose a single partial differential equation:

$$\frac{\partial T}{\partial t} = \underbrace{\kappa(t)\frac{\partial^2 T}{\partial z^2}}_{\text{diffusion}} - \underbrace{\mu\frac{T - T_f}{|z - z_f|}}_{\text{mixing}} + \underbrace{\frac{1}{\rho_w c_p}\frac{\partial Q(z,t)}{\partial z}}_{\text{source}} \ . \tag{5.1}$$

Here $\kappa(t) > 0$ is the time-dependent diffusivity and $\mu > 0$ is a constant which we term the relaxation coefficient of mixing, or simply *mixing coefficient*. ρ_w and c_p are the density and heat capacity at constant pressure of sea water, respectively. Furthermore, $Q(z,t)$ denotes the total heat flux, defined positive downwards (into the ocean). The prescribed foundation temperature $T_f \equiv T(z_f)$ is fixed in time, acting as a Dirichlet boundary condition at the lower domain boundary. Physically, it represents the bulk SST in the absence of any diurnal variation or cool skin effect. At the surface ($z = 0$), the sea temperature evolves under the influence of the surface heat fluxes $Q(0,t)$.

The temperature dynamics are thus governed by three components: a diffusion term, an additional mixing term, and a source term.

- **Diffusion term.** The first term describes the diffusion of heat due to molecular conduction and turbulent mixing. In the case of a time-independent diffusivity κ, it corresponds to the right hand side of the heat equation. In other words, we approximate turbulence as down-gradient diffusion using first-order turbulence closure (see section 3.3.1). Intuitively, we argue that the turbulent diffusion term should contain some form of wind dependence, since we know from observations and theory that increased wind stress leads to enhanced turbulence in the upper ocean. The wind stress $\boldsymbol{\tau}$ is proportional to the square of the horizontal wind speed $u(t)$ (see eq. (3.3)). Based on this heuristic argument, we propose a turbulent diffusivity κ_{turb} proportional to u^2. Together with the molecular diffusivity κ_{mol}, we write this as

$$\kappa(t) := \kappa_{\text{mol}} + \tilde{\kappa}\frac{u(t)^2}{u_0^2} \ , \tag{5.2}$$

[1] This is a common convention; it may sometimes be easier to define the vertical coordinate the other way around

where $\tilde{\kappa}$ may be interpreted as the wind stress-specific turbulent diffusivity and $u_0 = 1\,\mathrm{m\,s^{-1}}$. We divide by u_0^2 to ensure that $\tilde{\kappa}$ has units of a diffusivity, $[\tilde{\kappa}] = \mathrm{m^2\,s^{-1}}$. This way, the wind dependence simply adds a dimensionless factor representing a time-dependent measure of turbulence. The magnitude of $\tilde{\kappa}$ scales the response of turbulent diffusion to wind stress; it will be one of the tuning parameters of our model. In the following, we refer to $\tilde{\kappa}$ as the *eddy diffusivity*.

The molecular diffusivity κ_{mol} is typically around three orders of magnitude smaller than κ_{turb} and only plays a role in the absence of turbulence (e.g. in the molecular skin layer very close to the sea surface, where no eddies can form [31]).

- **Internal mixing term.** The diffusion term only includes turbulent mixing due to wind forcing at the surface, which induces shear instability. In principle, turbulent eddies can also arise from other instabilities, e.g. related to convective overturning under instable density stratification, or internal waves. We argue that such turbulent processes will mix the water of the diurnal layer with deeper waters from the foundation layer. Consequently, any temperature deviations in the diurnal layer will eventually relax to the foundation temperature. It seems reasonable that water masses close to the foundation depth will mix faster with foundation layer water compared to water masses near the sea surface. These considerations motivate the introduction of a linear relaxation term that depends inversely on depth, i.e.

$$\text{internal mixing} \;\sim\; -\mu \frac{T - T_f}{|z - z_f|} \;, \tag{5.3}$$

where $t_\mu := |z - z_f|/\mu$ is the relaxation time scale. The mixing coefficient μ controls the speed of the relaxation and is the second tuning parameter in our model. Note that technically the internal mixing term diverges as $z \to z_f$, but in practice we will evaluate eq. (5.1) at finite distances from z_f, as we discuss below (section 5.3).

- **Source term.** The dynamics of eq. (5.1) would be rather uneventful without a source term. This is where the radiative forcing and the surface heat fluxes enter the equation. At the surface, the net heat flux is given by

$$Q(0,t) = R_{\mathrm{sw}}(t) + R_{\mathrm{lw}}(t) + Q_{\mathrm{s}}(t) + Q_{\mathrm{l}}(t) \;, \tag{5.4}$$

where R_{sw} is the incident solar irradiance penetrating the air-sea interface. For the longwave (R_{lw}), sensible (Q_{s}), and latent (Q_{l}) heat fluxes, we use the standard bulk parametrizations described in section 3.2 (eqs. (3.6, 3.8, 3.9)), which we recapitulate here in the notation of our model:

$$R_{\mathrm{lw}}(t) = \sigma_{\mathrm{SB}}\Big(\varepsilon_a T_a(t)^4 - \varepsilon_w T(0,t)^4\Big) \tag{5.5a}$$

$$Q_{\mathrm{s}}(t) = \rho_a c_{p,a} C_s u(t) \Big(T_a(t) - T(0,t)\Big) \tag{5.5b}$$

$$Q_{\mathrm{l}}(t) = \rho_a C_l L u(t) \Big(s_a(t) - s_{\mathrm{sat}}(T(0,t))\Big) \;. \tag{5.5c}$$

The surface fluxes add a number of constants to the model, some of which are physical while others have well-established empirical values. We summarize them in table 5.1.

The longwave heat flux includes the emissivities ε_a and ε_w of air and sea water, respectively. To a good approximation, we set $\varepsilon_w = 1$, meaning that the ocean is

a black body [78]. In the case of air, an emissivity of less than 1 could be used to incorporate the fact that the atmosphere is not opaque to outgoing longwave radiation. For now, we set $\varepsilon_a = 1$ as the simplest choice.

In general, the latent heat flux will always be non-positive because the specific air humidity s_a will not exceed the saturation specific humidity at the sea surface, s_{sat}. According to the Clausius-Clapeyron equation eq. (3.2), s_{sat} is a function of temperature – in this case the sea surface temperature. While evaluating the Clausius-Clapeyron equation can be complicated, there exists a common approximation which yields the saturation water vapor pressure e_{sat} for given temperature T [79]:

$$e_{\text{sat}}(T) \approx 611.2 \exp\left(\frac{17.67(T - 273.15)}{T - 29.65}\right) , \tag{5.6}$$

where e_{sat} is in units of Pa and T in K. From this, we obtain the saturation specific humidity at temperature T,

$$s_{\text{sat}}(T) \approx \frac{e_{\text{sat}}(T)}{\rho_a R_w T} , \tag{5.7}$$

Here R_w is the gas constant of water vapor; its value is stated in table 5.1.

In contrast with the longwave, sensible, and latent heat fluxes, shortwave radiation can penetrate through the sea skin and is absorbed at a range of depths. As we learned in chapter 3, the combination of absorption and scattering leads to an exponential decay of downward irradiance with depth. Although more sophisticated options exist, we keep it simple and describe the attenuation of solar radiation by a single exponential function for all electromagnetic frequencies. The irradiance $\Gamma(z,t)$ is thus written as

$$\Gamma(z,t) = R_{\text{sw}}(t) \exp\left(-\alpha|z|\right) , \tag{5.8}$$

where $\alpha > 0$ is the effective *attenuation coefficient* integrated over the shortwave spectrum. The attenuation coefficient becomes the third general tuning parameter of our model. It determines the length scale at which the incoming radiation is absorbed. For example, an attenuation coefficient of $\alpha = 1\,\text{m}^{-1}$ implies that only 10% of the radiation reaches depths greater than 2.3 m.

To summarize, the heat flux $Q(z,t)$ is given by

$$Q(z,t) = \begin{cases} R_{\text{sw}}(t) + R_{\text{lw}}(t) + Q_{\text{s}}(t) + Q_{\text{l}}(t) & z = 0 \\ \Gamma(z,t) & 0 > z > z_f \end{cases} . \tag{5.9}$$

Note that depending on the value of α, a certain fraction of radiation is lost in our model since it gets absorbed below the foundation depth. The foundation depth should be chosen such that this fraction is negligible.

So far, we have an idealized model with three parameters:

- the eddy diffusivity $\tilde{\kappa}$,
- the mixing coefficient μ,
- and the attenuation coefficient α.

Quantity	Symbol	Units	Value
Molecular diffusivity (water)	κ_{mol}	$\mathrm{m^2\,s^{-1}}$	$1 \times 10^{-7}\,\mathrm{m^2\,s^{-1}}$
Specific heat (water)	c_p	$\mathrm{J\,K^{-1}\,kg^{-1}}$	$3850\,\mathrm{J\,K^{-1}\,kg^{-1}}$
Specific heat (air)	$c_{p,a}$	$\mathrm{J\,K^{-1}\,kg^{-1}}$	$1005\,\mathrm{J\,K^{-1}\,kg^{-1}}$
Density (water)	ρ_w	$\mathrm{kg\,m^{-3}}$	$1027\,\mathrm{kg\,m^{-3}}$
Density (air)	ρ_a	$\mathrm{kg\,m^{-3}}$	$1.1\,\mathrm{kg\,m^{-3}}$
Refractive index (water)	n_w		1.34
Refractive index (air)	n_a		1.00
Stanton number	C_{s}		1.3×10^{-3}
Dalton number	C_{l}		1.5×10^{-3}
Latent heat of vaporization	L	$\mathrm{J\,kg^{-1}}$	$2.5 \times 10^{6}\,\mathrm{J\,kg^{-1}}$
Stefan-Boltzmann const.	σ_{SB}	$\mathrm{W\,m^{-2}\,K^{-4}}$	$5.67 \times 10^{-8}\,\mathrm{W\,m^{-2}\,K^{-4}}$
Gas constant (water vapor)	R_w	$\mathrm{J\,K^{-1}\,kg^{-1}}$	$461.51\,\mathrm{J\,K^{-1}\,kg^{-1}}$

Table 5.1: Physical constants in the model, their units, and values [80, 81, 82, 83, 57].

Additionally, we must specify the foundation temperature T_f. In our model, all mixing processes in the upper ocean are approximated by a wind-dependent diffusion term and a second internal mixing term. This adds a step of complexity compared to a standard single-layer slab model, but it is still considerably simplified compared to most of the models reviewed in section 3.3.1. The choice of a constant eddy diffusivity $\tilde{\kappa}$ forms the base version of our model (which we will later refer to as BASE). However, the base setup could be too simple to yield reasonable results, since it neglects any vertical variations of diffusivity due to density stratification. In the next section we propose three elementary refinements based on intuitive reasoning. We test the performance of these options against the base version in section 5.4.

5.2.1 Vertically varying diffusivity: Three options

From previous studies of the upper ocean (see chapter 3), we know that the level of turbulence generally varies with depth and time, even during constant wind conditions. Under diurnal warming, wind-driven turbulence competes against the stabilizing tendency of a positive temperature gradient. This gradient typically forms before noon when the sun heats near-surface waters, leading to stable density stratification. In consequence, the stratification inhibits vertical mixing; it would increase potential energy to mix colder, denser waters upwards. A positive feedback emerges: stratification leads to heat trapping, which leads to increased stratification, and so on. Later, as solar insolation weakens in the afternoon, the net surface heat flux turns from positive to negative, cooling the upper ocean. This causes instable density stratification, or buoyancy, and induces convective overturning.

To incorporate these dynamics in our model, we propose three highly simplified options that let the eddy diffusivity vary with depth. When doing so, we must think back to how the turbulent diffusivity is derived from the turbulent heat flux $\overline{w'T'}$ (see section 3.3.1). There, we pulled the diffusivity out of the outer spatial derivative, since it was a constant. In the case of a depth-dependent diffusivity, we must use the chain rule:

$$\frac{\partial}{\partial z}\left(\kappa \frac{\partial T}{\partial z}\right) = \frac{\partial \kappa}{\partial z}\frac{\partial T}{\partial z} + \kappa \frac{\partial^2 T}{\partial z^2}\ . \tag{5.10}$$

Hence, whenever using a depth-dependent diffusivity, we replace the diffusion term in eq. (5.1) with the right-hand side of eq. (5.10).

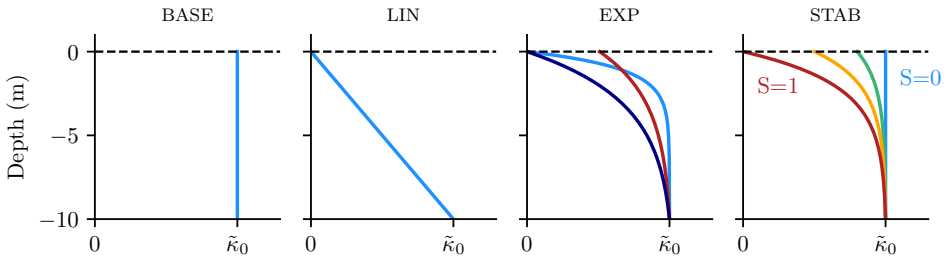

Figure 5.1: Vertical profiles of eddy diffusivity for the proposed parametrizations. The plots are labeled by their corresponding model version. (EXP) shows the effect of the parameters λ and σ by three example profiles: ($\lambda = 1, \sigma = 1$, blue), ($\lambda = 3, \sigma = 1$, dark blue), and ($\lambda = 3, \sigma = 0.5$, red). The right panel (STAB) illustrates the effect of the stratification factor from no stratification (blue) to full stratification (red). Here $\lambda = 2$ and $\sigma = 1$.

- **Linear diffusivity.** A first generalization of a constant eddy diffusivity $\tilde{\kappa}$ is to make it a linear function of depth. Arguably, the diffusivity should be smaller near the surface for two reasons: firstly, owing to the stratification effect during diurnal warming as described above; and secondly because the characteristic size of turbulent eddies decreases as we get close to the surface boundary. Smaller eddies transport heat less efficiently. As the simplest option we thus simply assume that the eddy diffusivity vanishes at the surface and write

$$\tilde{\kappa}(z) := \tilde{\kappa}_0 \frac{z}{z_f} \ . \tag{5.11}$$

  In this case the constant $\tilde{\kappa}_0$ is our model parameter for eddy diffusivity. We will refer to this model version as the LIN model. It is governed by the three paramters $\tilde{\kappa}_0$, μ, and α.

- **Exponential diffusivity.** A linear increase of diffusivity with depth may not be adequate because it increases relatively slowly near the surface and keeps steadily increasing thereafter. Instead, we imagine that there may be some characteristic depth at which the near-surface effects on diffusivity become small. This motivates an exponential dependence, which we write as

$$\tilde{\kappa}(z) := \tilde{\kappa}_0 \frac{1 - \sigma \exp(-|z|/\lambda)}{C_f} \ , \tag{5.12}$$

  with the normalization constant $C_f := 1 - \sigma \exp(-|z_f|/\lambda)$. Here we have introduced two new parameters: the *trapping depth* $\lambda > 0$ and the *surface suppressivity* σ ($0 \leq \sigma \leq 1$). The trapping depth characterizes how deep the suppression of turbulence due to stratification reaches into the water column. The surface suppressivity determines the value of the eddy diffusivity at the surface. If $\sigma = 1$, the surface eddy viscosity is zero. On the other hand, if $\sigma = 0$, then eq. (5.12) reduces to a constant eddy diffusivity $\tilde{\kappa}_0$, and we recover the BASE model.

  The exponential diffusivity profile is illustrated in fig. 5.1 along with the alternative options. We will refer to this version as the EXP model; it involves five parameters $\tilde{\kappa}_0$, μ, α, λ, and σ.

- **Stability-dependent diffusivity.** The purpose of reducing the diffusivity near the surface is to mimic the stabilizing effect of thermal stratification. This phenomenon is

Model version	Type of diffusivity	Parameters	Reference equation
BASE	constant $\tilde{\kappa}$	$\tilde{\kappa}$, μ, α	(5.2)
LIN	linear $\tilde{\kappa}$	$\tilde{\kappa}_0$, μ, α	(5.2), (5.11)
EXP	exponential $\tilde{\kappa}$	$\tilde{\kappa}_0$, μ, α, λ, σ	(5.2), (5.12)
STAB	stability-dependent $\tilde{\kappa}_0$	$\tilde{\kappa}$, μ, α, λ, σ, z_r	(5.2), (5.14)

Table 5.2: Overview of the four model versions.

restricted to clear and calm weather conditions. It is also localized in time, typically starting a few hours before noon and diminishing in the early afternoon. In fact, we may see the stratification effect as a state-dependent process since it depends on the temperature profile. The LIN and EXP versions neglect this by reducing $\tilde{\kappa}$ independently of time or temperature.

As a third option, we therefore propose an extension to the EXP model which makes $\tilde{\kappa}$ state-dependent. The level of stratification depends on the density gradient, which is approximately proportional to the temperature gradient. Based on this, we introduce a bulk *stratification factor* S. We assume that S is proportional to the temperature difference ΔT_r between the sea surface and some reference depth z_r,

$$\Delta T_r(t) := T(0,t) - T(z_r,t) \ ,$$

where $z_f < z_r < 0$. If this temperature difference is zero or negative, the water column within $[z_r, 0]$ is neutrally or instably stratified, and we set $S = 0$. Conversely, if $\Delta T_r > 0$ indicating stable stratification, then $S > 0$. We impose an upper limit of $S = 1$ once ΔT_r reaches 1 K, which basically means that we assume the water column to be "fully stratified" when $\Delta T_r \geq 1$. As a formula, this reads

$$S(t) = \begin{cases} 1 & \text{if } 1 < \Delta T_r(t) \\ \Delta T_r(t) & \text{if } 0 < \Delta T_r(t) \leq 1 \\ 0 & \text{otherwise.} \end{cases} \tag{5.13}$$

The general goal is to define an eddy diffusivity that is constant with depth, like the BASE version, *unless* there is stable near-surface stratification in which case the diffusivity is locally suppressed. We achieve this by multiplying the stratification factor S to the surface suppressivity σ in eq. (5.12), giving

$$\tilde{\kappa}(z) := \tilde{\kappa}_0 \frac{1 - S\sigma \exp(-|z|/\lambda)}{1 - S\sigma \exp(-|z_f|/\lambda)} \ . \tag{5.14}$$

In a sense, this leads to a form of "rich-gets-richer" dynamics, since a lower diffusivity enables further thermal stratification, which further reduces the diffusivity, and so on. Equation (5.14) defines the STAB version of our model, involving the six parameters $\tilde{\kappa}_0$, μ, α, λ, σ, and z_r. We can reduce the number of parameters by one if we relate the reference depth z_r to the trapping depth λ, and we might also set $\sigma = 1$ such that full stratification implies total suppression of turbulence at the surface.

In summary, we have four versions of our model to test against each other. They differ in their parametrization of eddy diffusivity. The BASE model is the most rudimentary version, and the progression BASE → LIN → EXP → STAB seeks to include additional detail at each step. This will allow us to investigate how much detail is needed to simulate diurnal warming in an idealized setting.

5.2.2 Atmospheric forcing

As input, the model requires time series of the following atmospheric variables:

- incident solar irradiance $R_{\text{sw, incident}}(t)$
- horizontal wind speed $u(t)$
- air temperature $T_a(t)$
- specific air humidity $s_a(t)$.

In the case of observational data, these quantities are typically measured at a reference height of 2-10 m above the sea surface. On the other hand, when coupled to a numerical atmospheric model, the atmospheric forcing is given by the state of the lowest vertical level in the atmospheric model.

Surface optics. For the sake of simplicity, we choose not to add a sophisticated absorption scheme that takes into account the multitude of factors involved in solar absorption. Nonetheless, we propose two refinements based on intuition and geometrical optics. Their purpose is to take account of the solar angle, i.e. the angle of the sun's position with respect to the normal of the surface plane.

We have previously defined the shortwave surface flux R_{sw} as the irradiance that passes the sea surface. In principle, a fraction $\mathcal{R}$ of incident irradiance is reflected back into the atmosphere when it hits the surface. The amount of reflection depends on the solar angle ϕ, which we define such that $\phi = 0$ when the sun stands in the zenith, parallel to the surface normal. The transmitted fraction $\mathcal{T}$ then becomes[2]

$$\mathcal{T} = 1 - \mathcal{R} = 1 - \frac{\mathcal{R}_\perp + \mathcal{R}_\parallel}{2} \ , \tag{5.15}$$

where we assume unpolarized light. The contributions from the two polarization directions read

$$\mathcal{R}_\perp = \left(\frac{n_a \cos\phi - n_w \sqrt{1 - (\frac{n_a}{n_w} \sin\phi)^2}}{n_a \cos\phi + n_w \sqrt{1 - (\frac{n_a}{n_w} \sin\phi)^2}} \right)^2 \tag{5.16}$$

$$\mathcal{R}_\parallel = \left(\frac{n_a \sqrt{1 - (\frac{n_a}{n_w} \sin\phi)^2} - n_w \cos\phi}{n_a \sqrt{1 - (\frac{n_a}{n_w} \sin\phi)^2} + n_w \cos\phi} \right)^2 \ , \tag{5.17}$$

where n_a and n_w denote the refractive indices of air and water, respectively. Their values can be taken from the literature and are listed in table 5.1. Thus the transmitted solar irradiance R_{sw} is given in terms of the incident solar irradiance reaching the sea surface, $R_{\text{sw, incident}}$, according to

$$R_{\text{sw}} = (1 - \mathcal{R}) R_{\text{sw, incident}} \ . \tag{5.18}$$

$R_{\text{sw, incident}}$ is what is measured, for example, by the sensor on a buoy.

Secondly, we consider that light rays take a different path through the water column depending on the solar angle ϕ. When the sun is low in the sky (large solar angle), the

[2] We neglect that in reality the sea surface is rarely completely even and flat.

optical path for the refracted light ray is longer to reach a certain depth z inside the water column. In other words, at large solar angles the incoming radiation effectively experiences more absorption and scattering before it reaches the depth z. To incorporate this, we invoke Snell's refraction law,

$$\phi' = \arcsin\left(\frac{n_a}{n_w}\sin\phi\right) \ , \tag{5.19}$$

where ϕ' is the refracted solar angle inside the water column and $0 \leq \phi < \frac{\pi}{2}$. While a light ray pointing straight down ($\phi' = 0$) needs to cover the distance z to reach depth z, a light ray with $\phi' > 0$ makes a distance of $z' = z/\cos(\phi')$ to reach the same depth. By replacing z with z' in (5.8), we finally get

$$\Gamma(z,t) = (1 - \mathcal{R}(\phi(t)))R_{\text{sw, incident}}(t)\exp\left(-\alpha\frac{|z|}{\cos\phi'(t)}\right) . \tag{5.20}$$

5.3 Numerical implementation

We implement the model in Python in order to solve eq. (5.1) numerically[3]. Following our objective to make the model suitable as a plug-in boundary condition in large-eddy simulations (LES) of the atmosphere, we focus on computational efficiency. First, we implement a non-uniform vertical grid to reduce the number of grid points. Then, we compare explicit and implicit Euler time-stepping schemes with the fourth-order Runge-Kutta scheme to find an adequate trade-off between computational speed and numerical accuracy.

5.3.1 Non-uniform vertical grid

In our model, the major sources and sinks of heat are located near the air-sea interface, where surface fluxes play an important role and most of the solar radiation is absorbed. Thus, we expect vertical temperature gradients to be largest near the surface. With increasing depth, the influence of the boundary diminishes while the relaxation term gains importance, counteracting the formation of strong temperature gradients.

This situation is a classical example of a boundary layer problem. As discussed in section 2.1.1, we require sufficiently high spatial resolution near the surface, whereas closer to the foundation depth a lower grid resolution may be chosen to save computational cost without too much loss of accuracy. This motivates the implementation of a stretched vertical grid, characterized by a steadily increasing grid spacing with increasing depth.

A simple way to build a non-uniform grid is to start with a small grid step Δz_0 and to increase each consecutive grid interval by a constant stretch factor $\epsilon > 1$. The depth z_n of the n-th point is then given by

$$z_n = -\Delta z_0\left(\frac{1-\epsilon^n}{1-\epsilon}\right) \ , \qquad n \in \{0,\dots,N\} \ . \tag{5.21}$$

[3]The code is available at https://github.com/reykboerner/diusst.

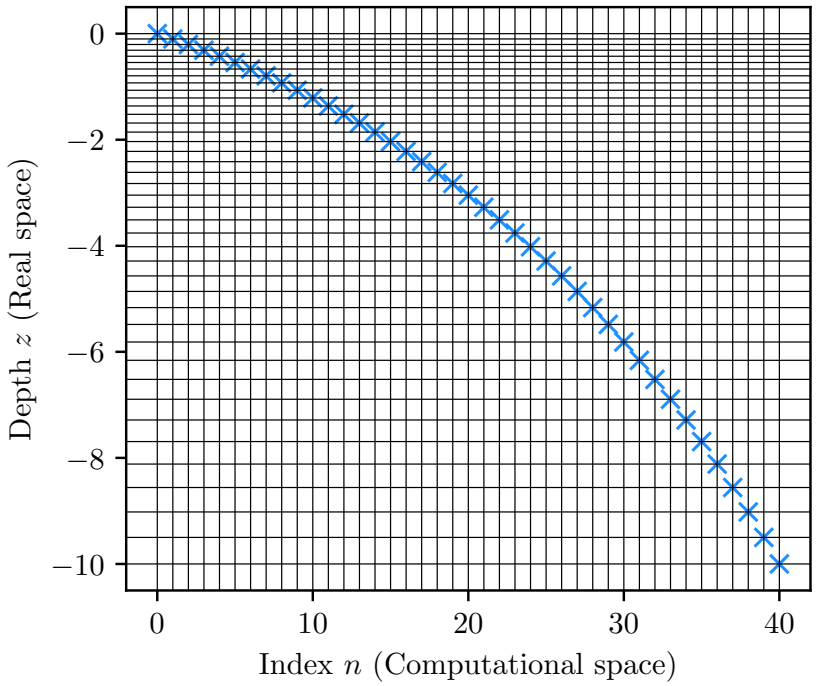

Figure 5.2: Visualization of the non-uniform vertical grid used for most simulations. Starting with a grid spacing of $\Delta z_0 = 10\,\text{cm}$ at the surface, the spacing increases with depth at a stretch factor $\epsilon \approx 1.04$. Here $N = 40$ and $z_f = -10\,\text{m}$.

Defining $\Delta z_n := z_{n+1} - z_n$, we indeed see that from n to $n+1$ the grid interval increases with the constant ratio $\epsilon = \frac{\Delta z_{n+1}}{\Delta z_n}$:

$$\Delta z_{n+1} = \frac{\Delta z_0}{1-\epsilon}\left(\epsilon^{n+2} - \epsilon^{n+1}\right) = \epsilon \frac{\Delta z_0}{1-\epsilon}\left(\epsilon^{n+1} - \epsilon^{n}\right) = \epsilon \cdot \Delta z_n \ . \tag{5.22}$$

In practice, we seek to obtain the stretch factor ϵ such that, for given Δz_0 and number of grid points N, the N-th point is located at the foundation depth z_f. This requires

$$z_f \equiv z_N = -\Delta z_0 \left(\frac{1-\epsilon^N}{1-\epsilon}\right) \ , \tag{5.23}$$

and solving for ϵ yields the implicit function

$$\epsilon(\Delta z_0, N) = 1 + \frac{\Delta z_0}{z_f}\left(1 - \epsilon^N\right) \ . \tag{5.24}$$

Eq. (5.24) can be solved iteratively with a numerical solver. Figure 5.2 illustrates the stretched grid for $z_f = -10\,\text{m}$, $\Delta z_0 = 0.1\,\text{m}$ and $N = 40$, corresponding to a stretch factor of $\epsilon \approx 1.04$.

Computing spatial derivatives. In section 2.1.1, we derived how to discretize spatial derivatives on a non-uniform grid. The general idea is to transform to computational space where the grid becomes uniform, evaluate the finite differences, and transform back to real space. The computational space may simply be defined by the set of grid indices n, since as integers they are evenly spaced in $\mathbb{N}$. (In the notation of 2.1.1, this means $\xi_n := n$ for

$\{0, \ldots, N\}$.) The transformation from z-space to n-space is found by inverting eq. (5.21), which yields

$$n(z) = \frac{\ln\left(1 + \frac{z}{\Delta z_0}(1-\epsilon)\right)}{\ln \epsilon} \ . \tag{5.25}$$

From this, we obtain the first and second derivatives of n with respect to z, which will enter our finite difference scheme:

$$\frac{\mathrm{d}n}{\mathrm{d}z} = \left[\ln\epsilon \cdot \left(\frac{\Delta z_0}{1-\epsilon} + z\right)\right]^{-1} \ , \tag{5.26}$$

$$\frac{\mathrm{d}^2 n}{\mathrm{d}z^2} = \left[-\ln\epsilon \cdot \left(\frac{\Delta z_0}{1-\epsilon} + z\right)^2\right]^{-1} \ , \tag{5.27}$$

We can show that this formulation reduces to a uniform grid in the limit of $\epsilon \to 1$, since

$$\lim_{\epsilon\to 1} \frac{\mathrm{d}n}{\mathrm{d}z} = -\frac{1}{\Delta z_0} \qquad \text{and} \qquad \lim_{\epsilon\to 1} \frac{\mathrm{d}^2 n}{\mathrm{d}z^2} = 0 \ . \tag{5.28}$$

Inserting this into eqs. (2.8) on page 5 retrieves the standard central finite difference on a uniform grid.

5.3.2 Discretized model equation

We implement three different time-stepping schemes: the explicit Euler method, the fourth-order Runge-Kutta method, and the implicit Euler method (see section 2.1). First, let us focus on the explicit Euler method. The discretized form of eq. (5.1) on a non-uniform grid reads

$$\begin{aligned}\frac{T_n^{i+1} - T_n^i}{\Delta t_i} = \kappa(t_i) &\left[\left(T_{n+1}^i - 2T_n^i + T_{n-1}^i\right) \cdot \left(\left.\frac{\mathrm{d}n}{\mathrm{d}z}\right|_{z_n}\right)^2 + \frac{T_{n+1}^i - T_{n-1}^i}{2} \cdot \left.\frac{\mathrm{d}^2 n}{\mathrm{d}z^2}\right|_{z_n}\right] \\ &- \mu\frac{T_n^i - T_f}{|z_n - z_f|} + \frac{1}{\rho_w c_p}\left[\left(Q_n^i - Q_{n-1}^i\right) \cdot \left.\frac{\mathrm{d}n}{\mathrm{d}z}\right|_{z_n}\right] \ ,\end{aligned} \tag{5.29}$$

for $n = 1, \ldots, N-1$, where n is the depth index and i the time index[4]. Note that we use a backward difference for the heat flux Q, since the heat source decreases with depth. At the foundation grid point $z_N \equiv z_f$, the boundary condition consists of imposing a constant foundation temperature $T_N^i = T_f$ for all time steps i. Therefore we do not have to evaluate the grid point N, and the grid point $N-1$ can be evaluated according to eq. (5.29). At the surface point ($n = 0$), we have a free boundary condition, requiring a choice how to handle the second derivative in the diffusion term. We use a dummy point in the atmosphere at height $z_{-1} := \Delta z_0$, which we assume has the same temperature[5] as T_0^i. Effectively, this means we compute the diffusion term at the surface based on the surface point and the

[4] The derivative $\mathrm{d}n\,/\,\mathrm{d}z$ is negative, since we defined z to decrease (i.e., it becomes more negative) with increasing n. This may help avoid confusion about signs in the finite differences

[5] Intuitively, the diffusion term acts to remove any temperature gradient at the surface, whereas the surface heat flux causes a temperature gradient.

point below it. Furthermore, we use the dummy point to evaluate the surface heat flux. With this, the explicit equation for the surface point becomes

$$\frac{T_0^{i+1} - T_0^i}{\Delta t_i} = \kappa(t_i) \left[\left(T_1^i - T_0^i\right) \cdot \left(\left(\left.\frac{\mathrm{d}n}{\mathrm{d}z}\right|_{z=0} \right)^2 + \frac{1}{2} \left.\frac{\mathrm{d}^2 n}{\mathrm{d}z^2}\right|_{z=0} \right) \right] - \mu \frac{T_0^i - T_f}{|z_f|} + \frac{1}{\rho_w c_p} \left[\left(Q_0^i - Q_{-1}^i\right) \cdot \left.\frac{\mathrm{d}n}{\mathrm{d}z}\right|_{z=0} \right] , \tag{5.30}$$

where Q_{-1}^i contains the surface heat fluxes, i.e.

$$Q_{-1}^i := R_{\mathrm{sw}}(t_i) + R_{\mathrm{lw}}(t_i) + Q_{\mathrm{s}}(t_i) + Q_{\mathrm{l}}(t_i) \ . \tag{5.31}$$

Runge-Kutta 4. The Runge-Kutta algorithm evaluates eqs. (5.29) and (5.30) at intermediate time points between t_i and t_{i+1}. A subtlety arises because our model equation is non-autonomous, i.e. it depends explicitly on time due to the time-dependent forcing. If the forcing is not known at the intermediate time steps (for example when the model is forced with a discrete observational time series), we must interpolate. In our case, we simply use the forcing at time step t_i, since we expect the forcing to be approximately the same until the next time step, which we will see is on the order of a few seconds.

Implicit Euler scheme. To derive the implicit version of eqs. (5.29) and (5.30), we replace the forward time difference on the right-hand side of these equations with a backward time difference (i.e. $i+1 \to i$ and $i \to i-1$) and move all time indices forward by one. Analogous to the description in section 2.1, the implicit scheme then involves the solution of the system of linear equations

$$\vec{T}^{i+1} = \left(\boldsymbol{A}^{i+1}\right)^{-1} \cdot \left(\vec{T}^i + \vec{b}^{i+1}\right) \ , \tag{5.32}$$

where the $N \times N$ matrix $\boldsymbol{A}^{i+1}$ and the N-dimensional vector $\vec{b}^{i+1}$ have the form

$$\boldsymbol{A}^{i+1} = \begin{bmatrix} \tilde{a}_0 & a_0^+ & 0 & \cdots & 0 \\ a_1^- & a_1 & a_1^+ & \cdots & 0 \\ \vdots & \ddots & \ddots & \ddots & \vdots \\ 0 & \cdots & a_{N-2}^- & a_{N-2} & a_{N-2}^+ \\ 0 & \cdots & 0 & a_{N-1}^- & a_{N-1} \end{bmatrix}^{(i+1)} \quad \text{and} \quad \vec{b}^{n+1} = \begin{pmatrix} b_0 \\ b_1 \\ \cdots \\ b_{N-2} \\ b_{N-1} - a_{N-1}^+ T_f \end{pmatrix} , \tag{5.33}$$

whose entries are given by

$$\begin{aligned} \tilde{a}_0 &:= 1 + \Delta t_{i+1} \kappa(t_{i+1}) \left(n'(0)^2 \pm \frac{1}{2} n''(0) \right) + \frac{\mu}{|z_n - z_f|} \\ a_n &:= 1 + 2\Delta t_{i+1} \kappa(t_{i+1}) n'^2 + \frac{\mu}{|z_n - z_f|} \\ a_n^\pm &:= -\Delta t_{i+1} \kappa(t_{i+1}) \left(n'^2 \pm \frac{1}{2} n'' \right) \\ b_n &:= -\Delta t_{i+1} \left(\frac{\mu}{|z_n - z_f|} T_f - \frac{Q_n^{i+1} - Q_{n-1}^{i+1}}{\rho_w c_p} \cdot n' \right) \ , \end{aligned} \tag{5.34}$$

for $n = 0, \ldots, N-1$. Here n' and n'' abbreviate the first and second derivative of n with respect to z_n.

Since the matrix $\boldsymbol{A}^{i+1}$ contains the time-dependent diffusivity $\kappa(t_{i+1})$, it is also time-dependent. In practice, this implies that we must compute and invert an $N \times N$ matrix at each time step, which comes at a high computational cost. Therefore, the implicit scheme may not be the most suitable option for our purposes. We lastly note that in the case of the state-dependent model version STAB, the matrix $\boldsymbol{A}^{i+1}$ would itself depend on the solution $\vec{T}^{i+1}$, such that the implicit scheme is not directly applicable without further approximations.

5.3.3 Numerical stability and speed

We now investigate the suitability of the three different time-stepping schemes for running our model. For this purpose, we focus on the BASE model. In the case of the two explicit schemes (Euler and RK4), we must consider that they are conditionally stable (see section 2.1). The numerical stability especially depends on the diffusion term, which has a Courant-Friedrichs-Lewy (CFL) number $\mathcal{C}$ of

$$\mathcal{C}(z_n, t_i) := 2\Big(\kappa_{\mathrm{mol}} + \tilde{\kappa} u(t_i)^2\Big) \frac{\Delta t_i}{\Delta z_n^2} \ . \tag{5.35}$$

Here we emphasize that the CFL number depends on depth and time, since it is a function of the variable grid spacing as well as of the wind speed. Stability requires that $\mathcal{C} \leq 1$ at all depths. This implies that for a given vertical grid, eddy diffusivity, and wind speed, we must use a time step not larger than

$$\Delta t_{i,\max} = \min_n \left(\frac{\Delta z_n^2}{2\Big(\kappa_{\mathrm{mol}} + \tilde{\kappa} u(t_i)^2\Big)} \right) \ . \tag{5.36}$$

Test simulations confirm that the solution becomes instable immediately after exceeding $\mathcal{C} = 1$ (not shown). It becomes clear that the wind-dependent turbulent diffusivity poses a numerical challenge, since the quadratic dependence of $\mathcal{C}$ on wind speed demands exceedingly small time steps under windy conditions. This makes the implicit Euler scheme tempting, given its unconditional stability.

Speed test. To conduct a speed test, we run each of the explicit Euler, implicit Euler, and RK4 implementations at different spatial resolutions, with the mixing coefficient and surface fluxes set to zero. We set the foundation temperature to 300 K while initializing the water column at 299 K, in order to have some diffusion dynamics in the simulation. We set the eddy diffusivity to $\tilde{\kappa} = 1 \times 10^{-4}\,\mathrm{m^2\,s^{-1}}$ and the wind speed to $10\,\mathrm{m\,s^{-1}}$. Furthermore, we choose a stretch factor of 1 (uniform grid) and then select the time step of each simulation such that it yields a certain CFL number. For the two explicit schemes we take $\mathcal{C} = 0.96$, whereas for the implicit scheme we also run the model at $\mathcal{C} = 60$ and 600, respectively. The execution times of these simulations per simulated model day are given in fig. 5.3.

We see that overall the Euler scheme is faster than the RK4 scheme. This is expected, since the RK4 scheme evaluates more time integrations per time step. The implicit scheme

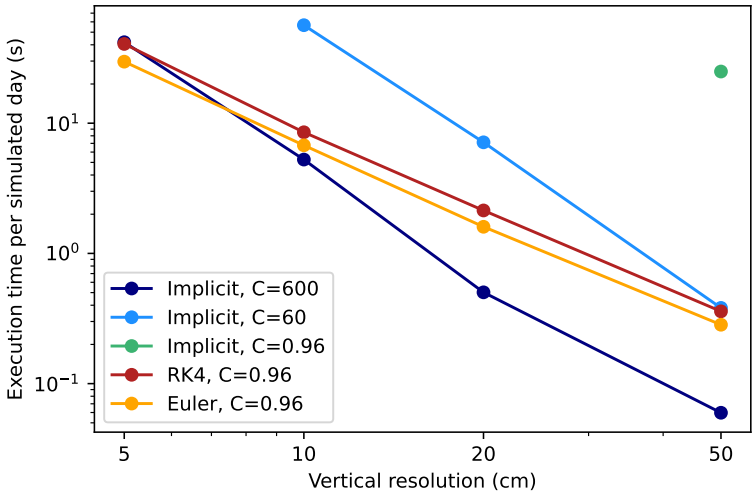

Figure 5.3: Speed test of time stepping schemes. The log-log plot shows the code execution time per simulated model day as a function of vertical grid resolution, run at different CFL numbers as indicated in the legend.

at the same CFL number is almost two orders of magnitude slower at 50 cm resolution, and its execution time increases faster with decreasing resolution compared to the explicit schemes – probably due to the need for inverting an increasingly large matrix at each time step. At 50 cm resolution, the implicit scheme is about as fast as the RK4 scheme when using a time step that corresponds to a CFL number of 60. At 5 cm resolution, we need to increase the CFL number to 600 in order to make the implicit scheme as fast as the RK4 scheme.

As fig. 5.4 suggests, the solutions from the implicit scheme vary considerably with the CFL number, such that we must expect low accuracy especially when $\mathcal{C} \gg 1$. Therefore, we rule out the implicit scheme. When comparing the explicit Euler with the RK4 scheme by means of an example simulation, we see in fig. 5.5 that both schemes yield very similar solutions. Since the Euler scheme is faster, we finally decide to use the explicit Euler scheme for our further investigation.

In order to contain the strong influence of wind speed on execution time, we impose an upper limit of $10\,\mathrm{m\,s^{-1}}$ on the wind speed entering the diffusivity. Any wind speeds larger than $10\,\mathrm{m\,s^{-1}}$ will be interpreted as $10\,\mathrm{m\,s^{-1}}$ in the diffusion term, whereas the actual wind speed is used to evaluate the surface fluxes. As our subsequent analysis will show, diffusion at $10\,\mathrm{m\,s^{-1}}$ wind speed is typically so strong that any temperature gradients will be flattened immediately. This justifies the choice of a cutoff.

To give an orientation, one day of simulation typically takes less than a second at low wind speeds, and up to several seconds for higher wind speeds. The execution time also depends on the value of the diffusivity and on the grid resolution.

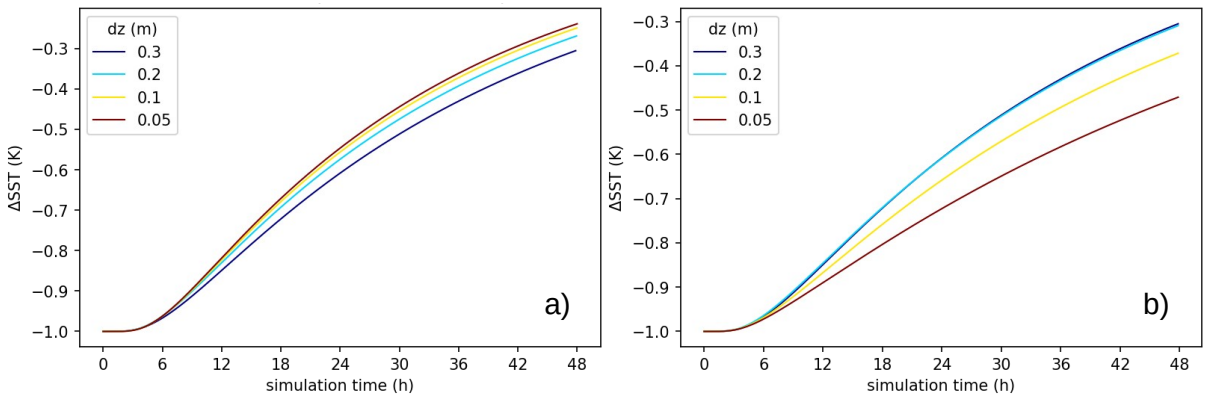

Figure 5.4: Grid convergence under constant and varying CFL number. Two sets of test simulations using the implicit scheme, showing the temperature difference between 1m depth and the foundation temperature as a function of time, after initialization as described in the main text. (a) shows runs at different grid resolution at a fixed CFL number $\mathcal{C} = 2.4$ (and thus varying time step); (b) shows the same but with a fixed time step of 9 minutes and varying CFL number. The left suggests convergence at low resolution, while the right suggests convergence at low CFL numbers. The key message is that the CFL number has a significant impact on the implicit scheme's solution.

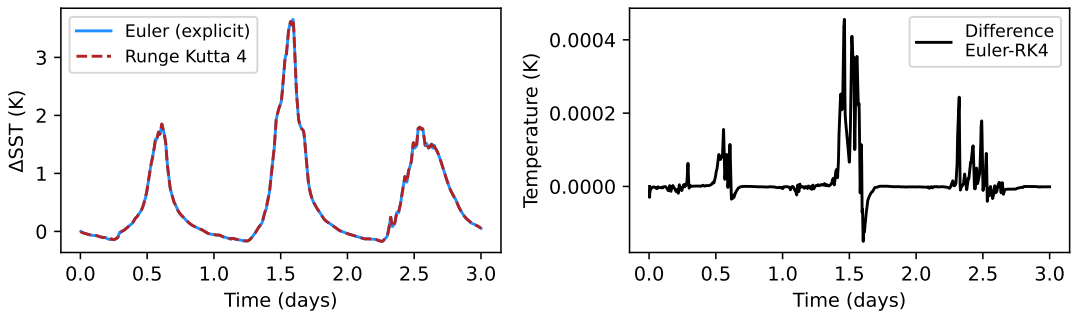

Figure 5.5: Comparison between the explicit Euler and RK4 schemes. The left panel shows the surface-foundation temperature difference ΔSST for a 3-day example simulation forced by real weather data from the MOCE-5 cruise (see chapter 4). The blue curve represents the Euler solution; red corresponds to the RK4 solution. The difference between the two solutions is plotted in the right panel.

5.4 Testing the model

Now that we have established the technical basis, we are ready to investigate diurnal warming in our model. Before using real atmospheric data, we first generate idealized artificial data to force the model. This will allow us to study the general behavior and sensitivity of the model under controlled conditions. In the next chapter, we will expose our model to the real world.

5.4.1 Idealized weather data

To mimic a generic, cloud-free day above the tropical ocean, we define the daily curves of solar irradiance, air temperature, air humidity, and wind speed in the following way. Imitating the sun's path over the course of the day, we assume a cosine-shaped irradiance curve between 6am and 6pm local time, with peak irradiance at noon, given by

$$R_{\text{sw, incident}}(t) = \begin{cases} R_{\text{sw}}^{\max} \cos\left(\frac{2\pi}{86400}t + \pi\right) & \text{if } \cos\left(\frac{2\pi}{86400}t + \pi\right) > 0 \\ 0 & \text{else,} \end{cases} \tag{5.37}$$

where $R_{\text{sw}}^{\max} = 1000\,\text{W}\,\text{m}^{-2}$ and time is in seconds. Next, we assume that the air temperature oscillates sinusoidally between a nighttime minimum $T_a^- = 299\,\text{K}$ and a daytime maximum $T_a^+ = 301\,\text{K}$:

$$T_a(t) = \frac{T_a^+ + T_a^-}{2} - (T_a^+ - T_a^-) \cdot \cos\left(\frac{2\pi}{86400}t\right) \ . \tag{5.38}$$

We introduce two types of wind conditions: either constant wind throughout the day ($u(t) = u_0$) or a sinusoidally varying wind that increases over night and calms down during the day, i.e.

$$u(t) = u_0 + \cos\left(\frac{2\pi}{86400}t\right) \ . \tag{5.39}$$

The latter option is inspired by the wind data observed during the MOCE-5 cruise (see fig. 4.5), where strong warming events often seem to coincide with a midday weakening of the wind. Lastly, we set the specific humidity to a constant value of $10\,\text{g}\,\text{kg}^{-1}$. The idealized weather data are visualized in fig. 5.6.

5.4.2 Parameter sensitivity experiments

We now use the artificial weather data to run a suite of sensitivity experiments with our model. Unless otherwise stated, we use the settings and parameter values given in table 5.3. Each simulation has a length of two days, where both days have identical weather conditions. The time step is chosen such that it gives a maximum CFL number of 0.95.

BASE model. Let us begin with the simplest version of our model, the BASE setup. It is controlled by the constant eddy diffusivity $\tilde{\kappa}$, the mixing coefficient μ, and the attenuation coefficient α. In figure 5.7, we show time series of surface warming ΔSST (defined as the temperature difference between the surface and the foundation depth) for a range of

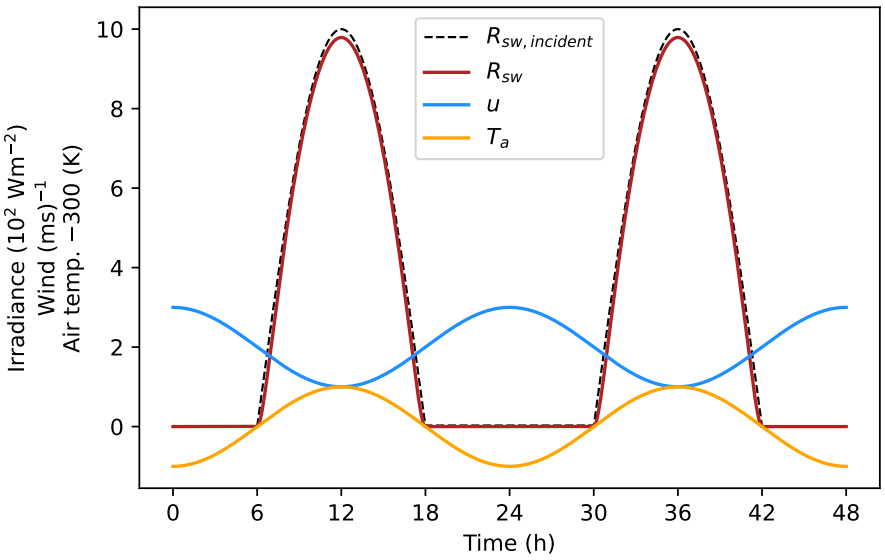

Figure 5.6: Time series of idealized weather data over two days. The curves are scaled or shifted to fit in one plot, as indicated on the vertical axis. The difference between the black dotted and the red solid line corresponds to the fraction of incident radiation that is reflected by the surface (see eq. (5.18)).

Quantity	Symbol	Value	Units	Comments
Wind speed	u_0	2	$\mathrm{m\,s^{-1}}$	constant
Grid spacing at surface	Δz_0	0.1	m	
Number of grid points	N	40		
Foundation depth	z_f	-10	m	
Foundation temperature	T_f	300	K	used as homogeneous initial cond.
Simulation time	$\mathcal{T}$	2	days	
CFL number	$\mathcal{C}$	0.95		

Table 5.3: Overview of settings for the sensitivity experiments.

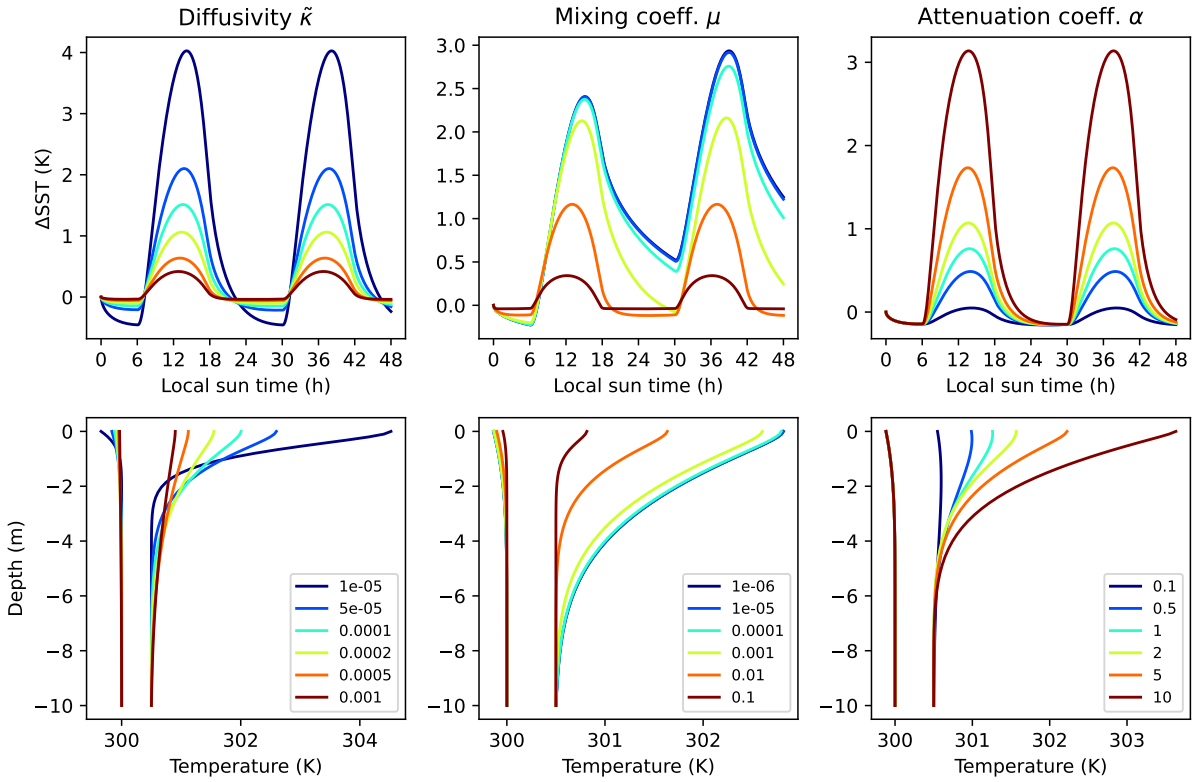

Figure 5.7: Sensitivity study of the BASE model. The top panels plot the surface-foundation temperature difference ΔSST as a function of time, while the bottom panels illustrate the corresponding vertical temperature profiles at 0200h (starting at $T_f = 300\,\mathrm{K}$) and 1400h (shifted by 0.5K) on the first day of simulation. Different colors indicate simulations with varied parameter values, as given in the legend. Left: variation of eddy diffusivity $\tilde{\kappa}$; center: mixing coefficient μ; right: attenuation coefficient α. In each case, the remaining two parameters are held fixed at values $\tilde{\kappa} = 1 \times 10^{-4}\,\mathrm{m^2\,s^{-1}}$, $\mu = 5 \times 10^{-3}\,\mathrm{m\,s^{-1}}$, and $\alpha = 4\,\mathrm{m^{-1}}$.

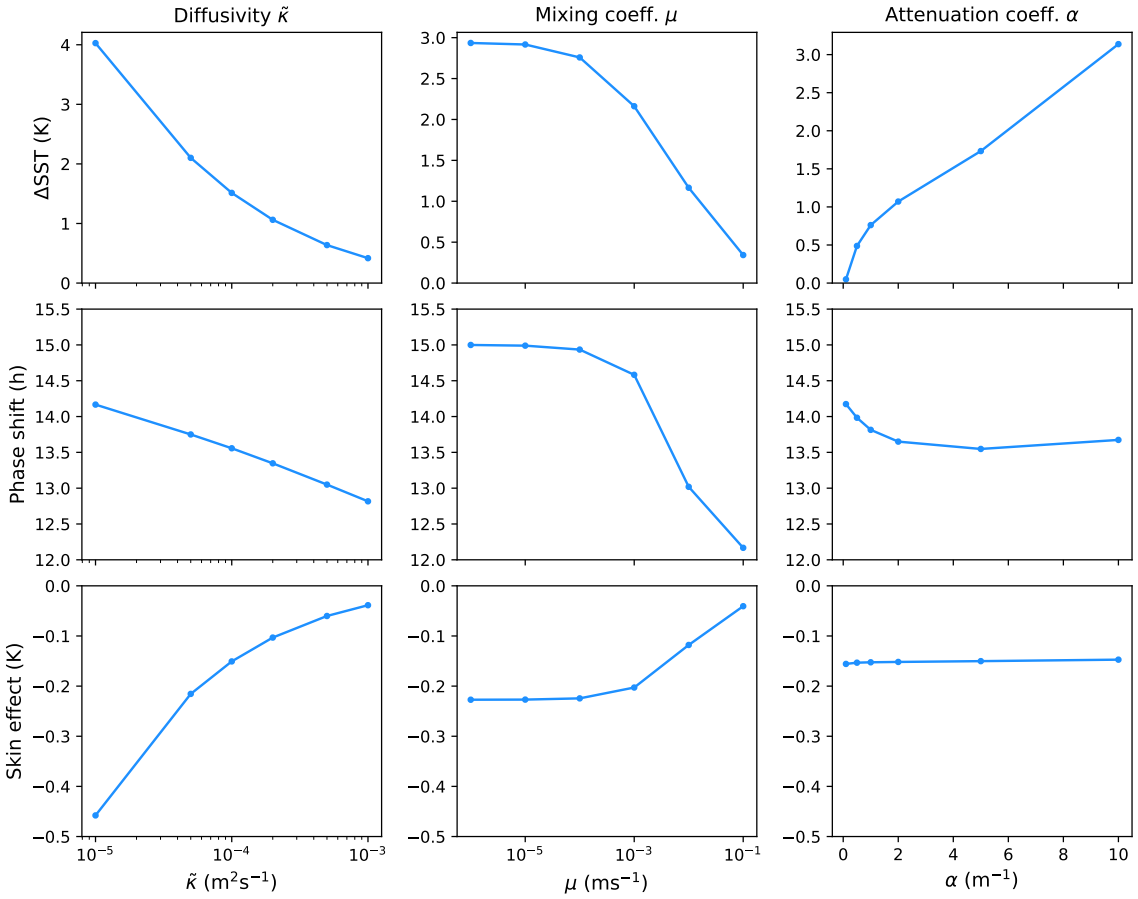

Figure 5.8: Warming amplitude, phase shift, and skin effect in the BASE model. The rows show the maximum value of the temperature difference ΔSST, the time of peak warming in hour of day, and the minimum value of ΔSST, respectively. Columns correspond to the parameter being changed, as labeled at the top. See the caption of fig. 5.7 for further details. Note the logarithmic scale in the left and center columns.

different parameter combinations. Additionally, we plot the vertical temperature profiles at 0200h and 1400h local time on the first day of each of these simulations.

Under the range of selected parameter values, the model produces diurnal surface warming that reaches up to 4 K during the day and cools again at night. The warming amplitude as well as the depth and time profiles of warming depend on the choice of all three parameters. Firstly, the diffusivity has a large impact on the amplitude and depth dependence of warming. Low diffusivity implies slow vertical heat transport, leading to intense heat trapping near the surface, where most of the solar radiation is absorbed. At higher diffusivity, heat is transported downwards more rapidly, leading to less warming near the surface but more warming below. The mixing coefficient acts like a relaxation velocity, i.e. large values of μ cause the temperature profile to quickly return to the foundation temperature, especially at greater depth. For small values of μ, we observe a run-away effect: heat is not sufficiently removed from the diurnal layer over night, such that the next day becomes warmer than the first. Longer simulations indicate that this increased warming continues until a new thermal steady-state is reached at several degrees higher temperature (not shown). The attenuation coefficient mainly scales the amplitude of warming. A high attenuation coefficient implies that most of the heat is absorbed near the surface, where it accumulates and where the internal mixing term has little influence. A smaller attenuation coefficient distributed the heating more equally over the diurnal layer, and much of the heat is "removed" into the foundation layer by the internal mixing term (or diffused downward).

Changing the diffusivity at constant wind speed is equivalent to changing the square of the wind speed under constant diffusivity. Thus, the sensitivity experiment for $\tilde{\kappa}$ also gives an idea of how wind affects diurnal warming in the model. We note that the dark blue depth profile in the bottom left panel of 5.7 seems optically similar to the observed low-wind profiles in fig. 4.4, while the yellow and orange profiles in the same plot resemble the medium-wind profiles in fig. 4.4.

To further analyze the trends observed in our sensitivity study, we focus on the time shift and value of peak ΔSST, as well as on the night-time minimum of ΔSST as a measure of the skin effect. In the literature, the term "skin effect" usually refers to radiative cooling in the upper millimeter of the sea skin, where molecular conduction dominates [74, 70]. Given that our grid resolution at the surface is 10 centimeters, we cannot hope to resolve these effects. Nonetheless we observe radiative cooling of the upper-most model layer, which we will refer to as skin effect in the present context.

Figure 5.8 depicts plots of the diurnal warming amplitude, phase shift of peak warming, and skin effect as a function of varied model parameters. We see that peak warming generally occurs after noon, and stronger warming typically coincides with a peak shifted later into the early afternoon. A pronounced skin effect appears at low diffusivities. The amplitude of warming appears to vary approximately linearly with the attenuation coefficient, while α has no notable influence on the phase shift or skin effect. Lastly, we note that the model response to each parameter is overall monotonic within the tested range. Based on this we do not expect any complex non-linear correlations between parameters.

LIN model. With a first understanding of how our model behaves under idealized forcing, let us switch to the LIN version of our model. In contrast with the BASE model, here the

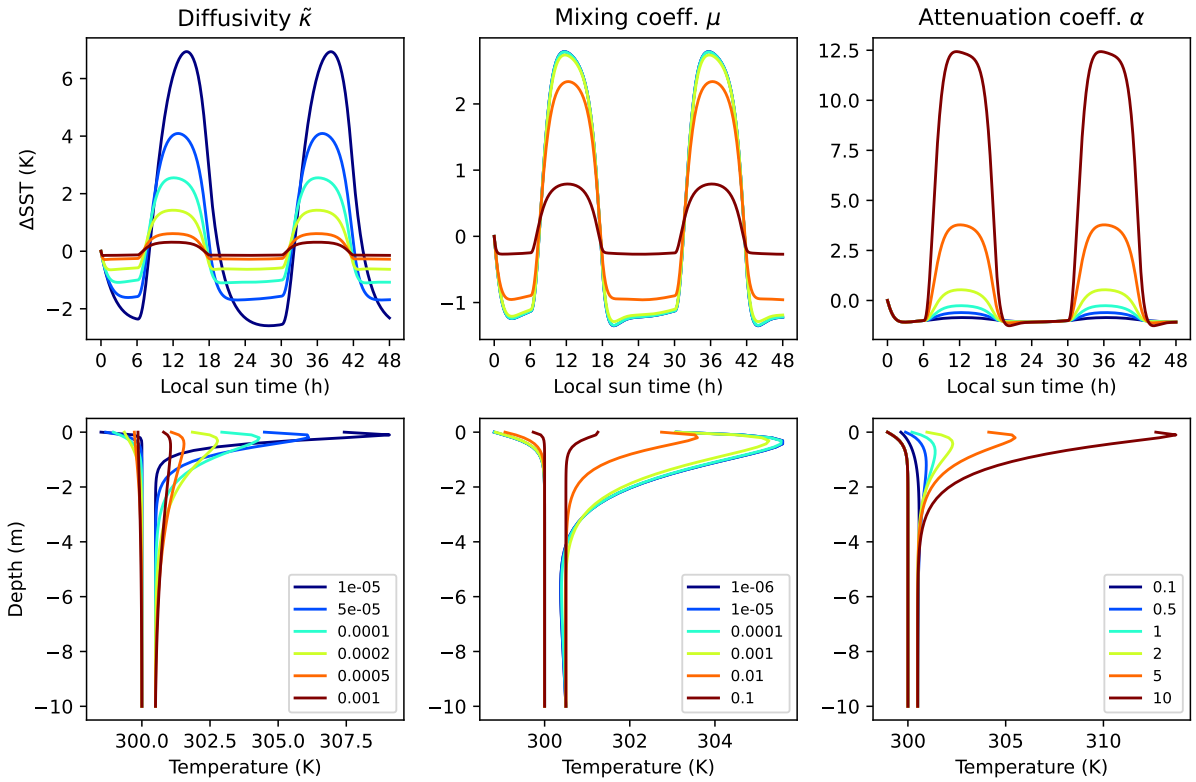

Figure 5.9: Sensitivity study of the LIN model. The figure shows the same as 5.7, but for the LIN model with a linear diffusivity profile.

eddy diffusivity vanishes at the surface and increases linearly with depth. We repeat the same sensitivity study as above; the results are shown in figs. 5.9 and 5.10.

The lower diffusivity at the surface has the effect that the upper part of the diurnal layer responds more directly to the atmospheric forcing, since it exchanges less heat with the water masses below. This manifests itself in more extreme warming during the day and intense skin cooling at night. Almost all vertical profiles feature an inversion in the near-surface temperature gradient. We interpret this as heat loss to the atmosphere which cannot be sufficiently resupplied with heat from below, due to the suppressed diffusivity. Only at large values of the parameters $\tilde{\kappa}$ and μ, their restoring effect limits the skin cooling as well as diurnal heating. Figure 5.10 quantifies the skin cooling (bottom row) and, furthermore, illustrates that peak warming mostly takes place closer to noon compared to the BASE model. This reflects that the surface responds to the diurnal cycle of solar radiation more directly.

EXP model. We have so far discussed two versions of our model: one which produces rather slowly varying behavior of near-surface temperature (BASE), and one which responds much more sensitively to atmospheric conditions (LIN). Our third model version, the EXP model, allows us to interpolate between these two "extreme" cases by varying the two additional parameters, namely the surface suppressivity σ and the trapping depth λ.

More specifically, the EXP model converges to the BASE model as $\sigma \to 0$, while it becomes equivalent to the LIN version when $\sigma = 1$ and $\lambda \to \infty$. In fig. 5.11, we compare example simulations from each of the three different versions. In the top row, the BASE model

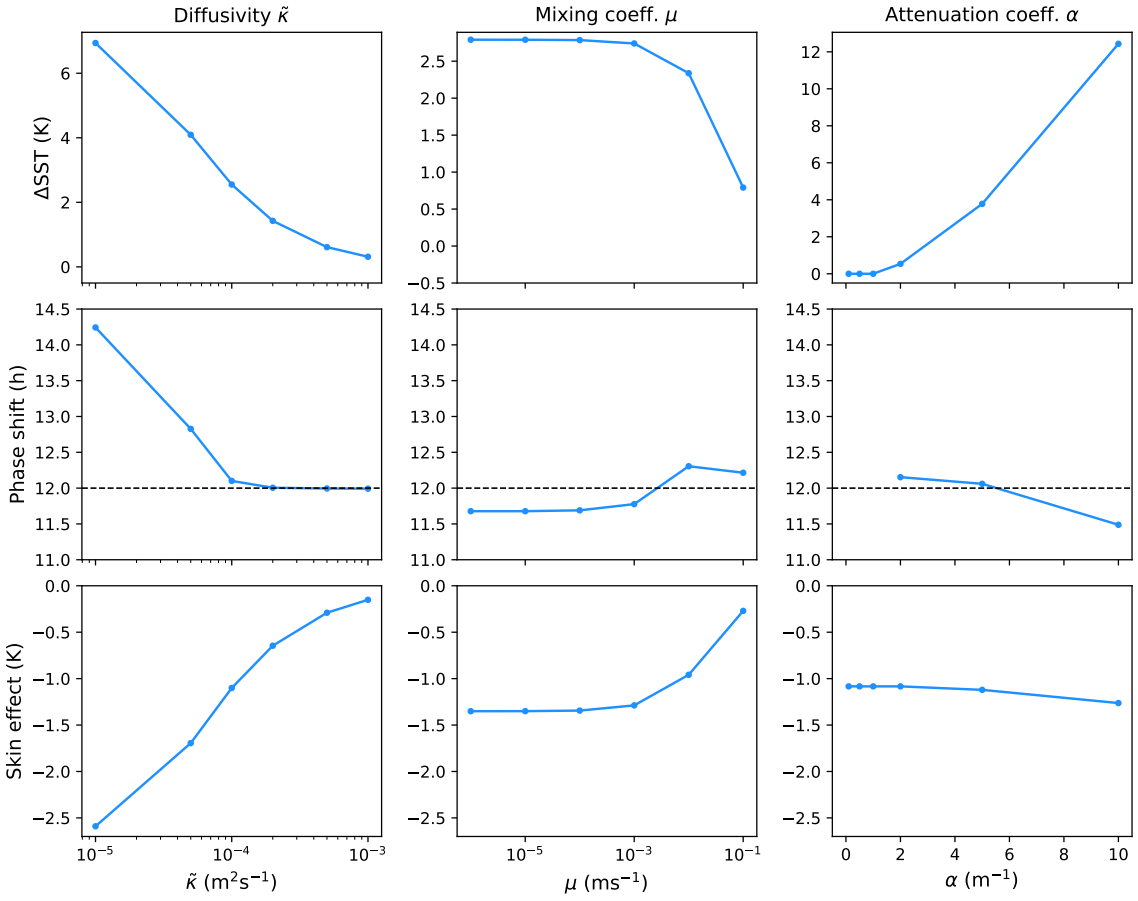

Figure 5.10: Warming amplitude, phase shift, and skin effect in the LIN model. The figure shows the same as 5.8, but for the LIN model. In the α sensitivity series, the phase shift cannot be determined for the two lowest values of α since the skin temperature remains cooler than the foundation temperature throughout the day.

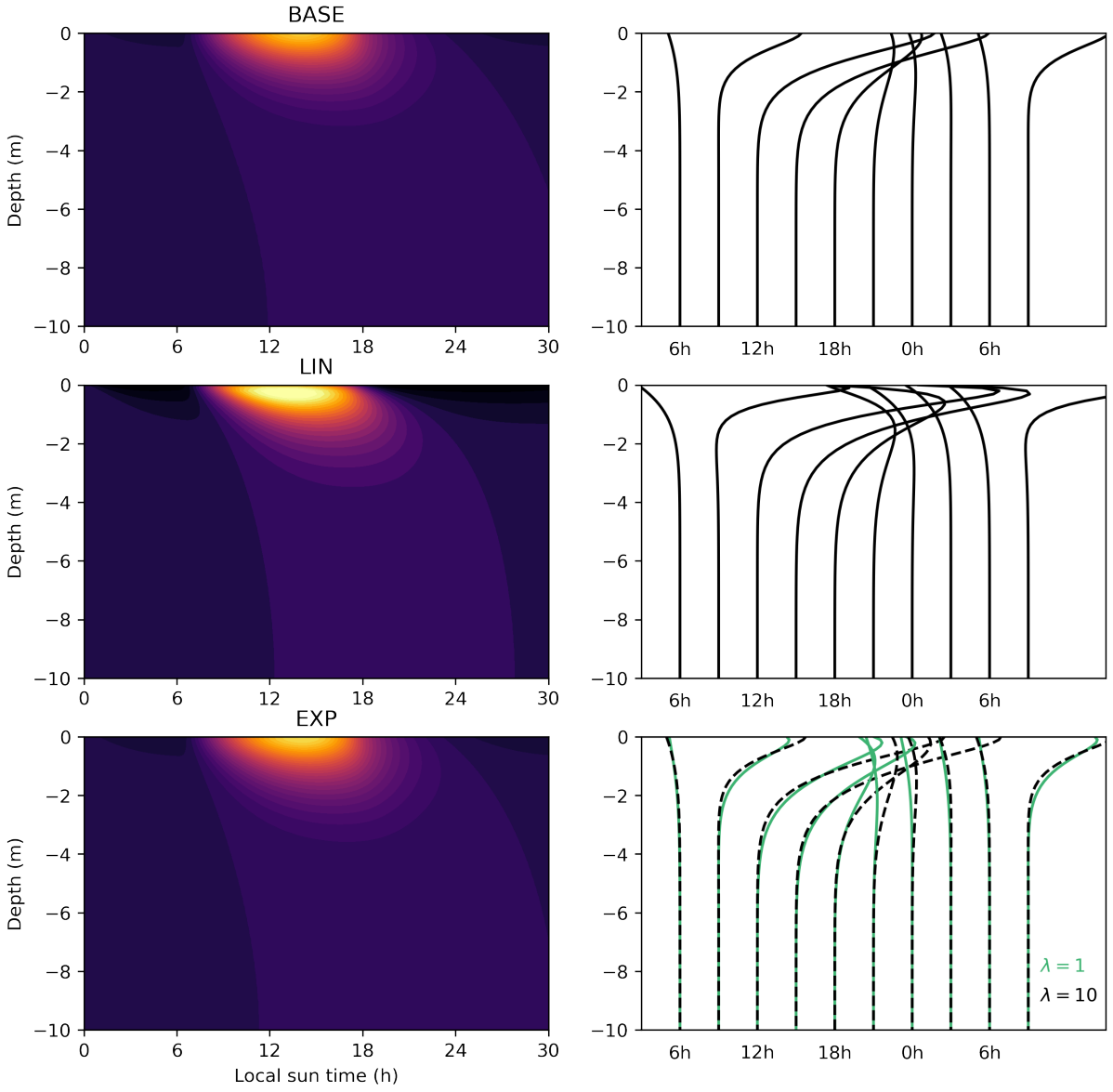

Figure 5.11: Comparison between BASE, LIN, and EXP versions. The contour plots (left) show temperature in a depth-time diagram, where black corresponds to $-0.5\,\mathrm{K}$ and bright yellow is $3\,\mathrm{K}$ or more. To the right of each contour plot, corresponding vertical temperature profiles are shown every three hours from 6am to 8am the following day (black lines). Each following profile is shifted by 0.5K. The bottom right panel additionally shows a simulation with different λ (green solid line, its contour plot is omitted.) In all cases, the wind is constant at $1\,\mathrm{m\,s^{-1}}$, $\mu = 5 \times 10^{-3}\,\mathrm{m\,s^{-1}}$, and $\alpha = 3\,\mathrm{m^{-1}}$. $\tilde{\kappa}$ is $1 \times 10^{-4}\,\mathrm{m^2\,s^{-1}}$ for BASE, $4 \times 10^{-4}\,\mathrm{m^2\,s^{-1}}$ for LIN, and $2 \times 10^{-4}\,\mathrm{m^2\,s^{-1}}$ for EXP. For the EXP model, $\sigma = 0.7$ and the values for λ are given in the figure.

features moderate warming without a significant inversion of the temperature gradient at the skin. Below, in the center row, we display a similar simulation from the LIN model, which is characterized both by strong diurnal warming and pronounced skin cooling. For example, we see a strong negative near-surface temperature gradient in the LIN profiles at 1800h and 2100h. As expected, the EXP simulations shows in-between behavior, i.e. stronger surface warming than the BASE example but less skin cooling than the LIN case. In this example, the surface suppressivity is set to $\sigma = 0.7$, meaning that at the surface the eddy diffusivity is 30% of the foundation depth value $\tilde{\kappa}_0$. To demonstrate the effect of the trapping depth λ, the bottom right panel of fig. 5.11 compares two simulations ($\lambda = 1$ and $\lambda = 10$). Overall, a large trapping depth means that the diffusivity is suppressed relatively far down into the water column, giving more vertical space for heat trapping. This leads to stronger near-surface warming, as shown in the figure. A smaller trapping depth allows for more heat transport near the surface, while still permitting surface cooling directly at the surface.

Interestingly, fig. 5.11 illustrates that all three model versions feature an asymmetry in the time-depth diagram, owing to the downward diffusion of heat at a certain time scale. This means that peak warming occurs earliest at the surface and later during the afternoon as we move deeper down the water column. This effect, sometimes referred to as "mixed-layer deepening", is also a characteristic of observations (see chapter 4).

STAB model. To conclude our test phase with artificial weather conditions, we briefly discuss what happens when we expand the EXP model to the STAB model. Recall that the STAB version includes a time-dependent stratification factor, mimicking the effect of heat trapping under stable thermal stratification during peak warming. A comparison between simulations from the EXP and STAB versions is provided in fig. 5.12.

The key difference between the two solutions is that the STAB model removes the negative temperature gradient near the surface. Until noon, the profiles are very similar. In the afternoon, the STAB profile warms slightly more and remains at warmer surface temperatures for a longer time. This extended near-surface heat trapping is clearly seen in the time-depth diagrams in the bottom row of fig. 5.12. We explain this as follows: as the sun's intensity increases, the stratification factor increases, suppressing diffusivity near the surface. Due to the strong solar insolation, the net heat flux is positive in the upper water layers, leading to enhanced warming. After the sun has crossed the zenith, the net surface flux eventually becomes negative, causing skin cooling. This reduces the stratification factor to zero, and near-surface turbulent mixing kicks in, which resupplies the heat lost to the atmosphere from the warm waters below.

It is interesting to note that the two simulations in fig. 5.12 were conducted with the sinusoidal wind pattern described by eq. (5.39), ranging from $3\,\mathrm{m\,s^{-1}}$ at midnight to $1\,\mathrm{m\,s^{-1}}$ at noon. This affects the structure of the mixed-layer deepening.

Selecting a candidate. Arguably, the STAB model is the most realistic of the four versions. It includes an approximate representation of the time-dependent stratification effect on diurnal warming, and the result in fig. 5.12 somewhat resembles simulations of other proposed models (e.g. [84]). However, it is also the least simple of the four model versions we present – while our aim is to keep it as simple as possible. As shown in fig.

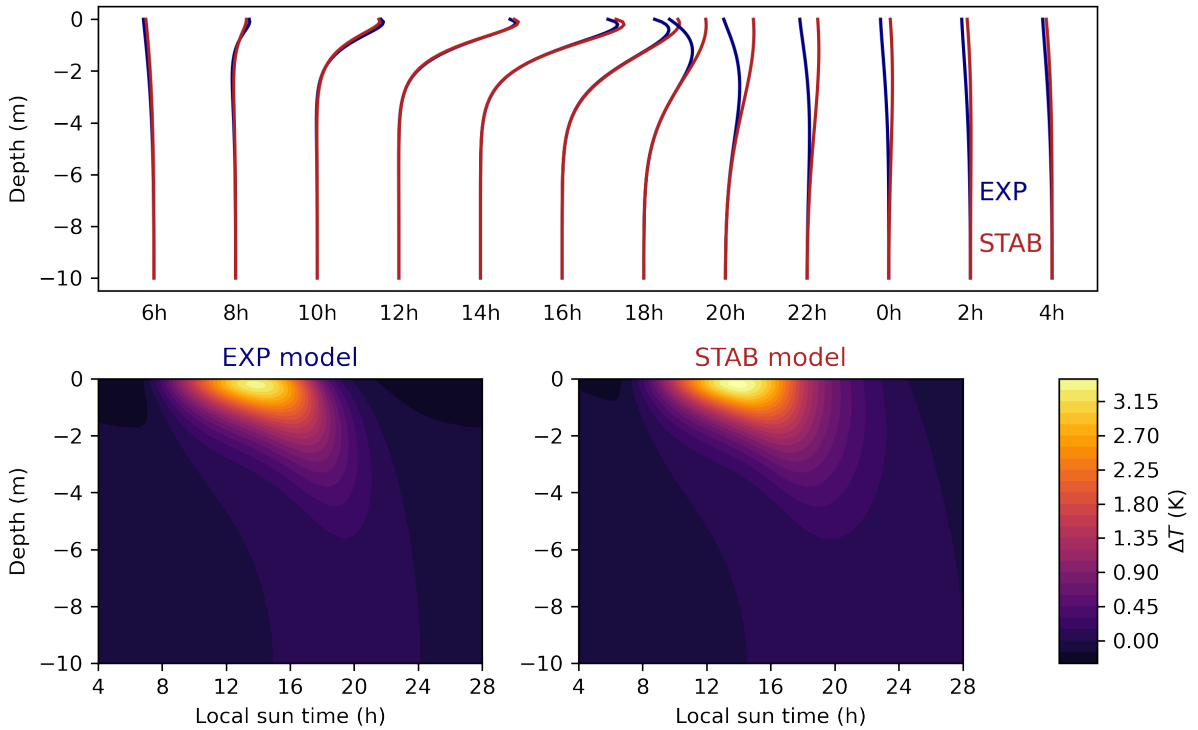

Figure 5.12: Warming and cooling in the EXP and STAB model. The top panel compares vertical temperature profiles from two simulations: one from the EXP model (dark blue) and one from the STAB model (red). Two hours correspond to 2 K on the horizontal axis. The bottom panels reveal the full time-depth information for each simulation. In both cases, the wind speed oscillates around $u_0 = 1\,\mathrm{m\,s^{-1}}$ according to (5.39). Parameter values are $\tilde{\kappa}_0 = 1 \times 10^{-4}\,\mathrm{m^2\,s^{-1}}$, $\mu = 0.002\,\mathrm{m\,s^{-1}}$, $\alpha = 2.5\,\mathrm{m^{-1}}$, $\sigma = 0.8$, and $\lambda = 2\,\mathrm{m}$. Furthermore, the reference depth for the stratification factor is $z_r = 1\,\mathrm{m}$.

5.11, we can also tune the EXP model in a way that it prevents excessive skin cooling, for example by reducing σ or increasing λ. We thus conclude that the EXP model offers a good compromise between flexibility and simplicity. Throughout the next chapter, we will focus on the EXP version.

6 Model calibration and validation

We began our study with an analysis of two observational datasets, which illuminated key features of diurnal surface warming in the tropical ocean (chapter 4). Based on this insight, we developed an idealized model of diurnal SST variability in chapter 5. In order to explore the general behavior of our model in a controlled environment, we first used artificial weather data as atmospheric forcing. Now, we are ready to expose our model to the real world. This chapter thus brings the observational and modeling parts of this thesis together.

Offering a compromise between flexibility and simplicity, we select the EXP version of our model, which is defined in terms of five tuning parameters: the eddy diffusivity $\tilde{\kappa}_0$ (we drop the subscript 0 from now on), the mixing coefficient μ, the attenuation coefficient α, the trapping depth λ, and the surface suppressivity σ. While the latter two parameters allow for a fine-tuning of the vertical diffusivity profile, we are mainly interested in the first three – they are the key parameters that regulate the fundamental processes in our model. Firstly, the diffusivity regulates the response of turbulent mixing to wind stress. Secondly, the mixing coefficient describes internal mixing and exchange processes with the foundation layer. And third, the attenuation coefficient governs at which depth range solar radiation is absorbed.

This thesis aims to develop a diurnal SST model suitable as a lower boundary condition for atmospheric simulations. Therefore, it is most important that the model captures the variability of SST directly at the air-sea interface. The dataset from the MOCE-5 cruise (see chapter 4) provides an observational record of precisely this skin temperature. Additionally, the dataset contains time series of wind speed, air temperature, and solar irradiance. This enables us to force our model with the MOCE-5 atmospheric data and compare the simulated solution of skin temperature evolution with that observed by the radiometer. Since the cruise dataset lacks humidity records, we assume a constant specific humidity of $10\,\mathrm{g\,kg^{-1}}$.

Throughout this chapter, simulations are run with $z_f = -10\,\mathrm{m}$, surface grid resolution $\Delta z_0 = 0.1\,\mathrm{m}$, number of grid points $N = 40$, and a CFL number of $\mathcal{C} = 0.95$.

6.1 Bayesian parameter estimation

The present situation is very common in science: on one side, we have a model, governed by a set of unknown parameters. On the other side, we have observational data – the "truth" – which our model seeks to describe. The framework of Bayesian inference provides a systematic approach to finding the most likely parameter values of the model, given the data. In the following, we describe how we use Bayesian inference to estimate the parameters of our model based on the MOCE-5 dataset.

Setup. As discussed in chapter 4, the MOCE-5 cruise took place in two different geographic regimes. At the beginning and end of the cruise, the research vessel sailed along the Mexican west coast on the open Pacific Ocean. For several days in between, the ship entered the Gulf of California, where the available data indicate that oceanic and atmospheric conditions were to some extent different. This presents both a challenge and an opportunity for our purposes. The challenge is that we may encounter difficulties in narrowing down uncertainties in the parameter estimates, since one parameter combination may not be able to describe both regimes. On the other hand, the diversity of conditions will allow us to investigate the generality of our model.

In addition to estimating parameter values, we wish to find out whether our model has predictive capabilities. It is therefore important that we only use a subset of the entire dataset as "training data" for Bayesian inference. The complementary set can then be used as a validation set.

Under these considerations, we choose the following setup. From the open Pacific part of the cruise, we select days 2, 3 and 4 (of October 1999) as the data interval to be used for Bayesian inference (see fig. 4.5). These days are characterized by relatively high wind speeds and low diurnal warming amplitudes. Likewise, from the Gulf part, we select days 13, 14, and 15. This interval contains the largest warming event of 5 K, as well as two other warming events of different amplitudes. We then estimate three sets of parameter values: 1) the best model based only on the Pacific interval; 2) the best model based only on the Gulf interval; and 3) the best model based on both 3-day intervals.

6.1.1 Likelihood and prior

According to Bayes' theorem, the posterior probability distribution of the parameter vector Θ is proportional to the product of the likelihood and the prior probability distribution. Thus, we first need to define a likelihood function $\mathcal{L}(\Theta)$ that quantifies how likely a certain parameter combination Θ is, given the data $\mathcal{D}$.

Likelihood function. Inspired by the χ^2 statistic, we define the likelihood as

$$\mathcal{L} = \exp\left(-\sum_{i\in\mathcal{D}} \frac{(m_i - d_i)^2}{\Sigma_i^2}\right) , \tag{6.1}$$

where the sum includes all data points in the training set $\mathcal{D}$, m_i is the simulated value of the data point d_i, and Σ_i is the standard error of the i-th data point. Specifically, the data points consist of the time series of temperature difference $\Delta\mathrm{SST}(t_i)$ between the sea surface and the foundation temperature at 3m depth. Using the atmospheric data as model input, we simulate the model with the parameter setting Θ to find the time series of simulated temperature differences,

$$m_i := T(0, t_i) - T(3, t_i) ,$$

where $T(0, t_i)$ and $T(3, t_i)$ are the modeled temperatures at the surface ($z = 0$) and at the grid point closest to $z = -3\,\mathrm{m}$, respectively, at the time of the data point d_i. We emphasize that we still use a foundation depth of $z_f = -10\,\mathrm{m}$ in the model, while using the grid point nearest to 3m depth to evaluate ΔSST.

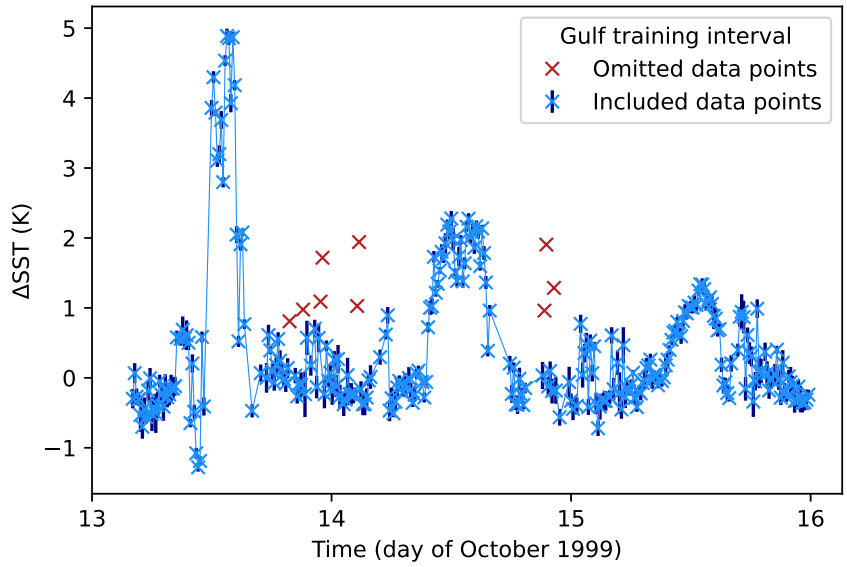

Figure 6.1: Removal of outlier data points. The red data points are omitted in the evaluation of the likelihood function. The blue data points constitute the Gulf training set; their error bars are also shown (dark blue bars).

Uncertainties ϵ_i of the skin temperature measurements are given in the MOCE-5 dataset, whereas no error is stated for the foundation temperature measurements. Rather arbitrarily, we define the error of the temperature difference $\Delta\mathrm{SST}(t_i)$ as

$$\Sigma_i = 2\epsilon_i \left(1 + \frac{v_i}{\max_i v_i}\right) , \tag{6.2}$$

where v_i is the boat speed at the i-th data point. This implies that the doubled error $2\epsilon_i$ is again increased up to a factor of two when the vessel moves. The reason behind this choice is that when cruising, the vessel may pass through waters of different temperatures which would distort the observed temperature difference. For example, a sudden cold current at 3m depth would imply an artificial rise in ΔSST, even though the skin is not warming. We thus increase the error of data points recorded under movement since we have less confidence in them.

Omitting outliers. In the Gulf training set (days 13, 14, and 15), we identify nine cases where ΔSST suddenly rises by around a Kelvin or more in the middle of the night (see fig. 6.1). We argue that these data do not originate from any of the effects we are trying to model but rather are artefacts of currents or of the moving boat. To avoid that these outliers affect the likelihood function, we remove them from the training set.

Since the likelihood function only depends on the temperature difference between two depths, it contains little information about the likelihood of the shape of the vertical profile. Essentially, the model output is two-dimensional (depth, time), whereas the likelihood function is based on one-dimensional data (temperature difference in time). Tests indicate that this makes it difficult to optimize five parameters at once. Since we are mainly interested in the key model parameters $\tilde{\kappa}$, μ, and α, we fix $\sigma = 0.8$ and $\lambda = 3\mathrm{m}$, leading

to $\Theta = (\tilde{\kappa}, \mu, \alpha)$. The given values of σ and λ are chosen based on an inspection of the resulting temperature profile shapes.

Prior distribution. Next to the likelihood function, we must specify a prior distribution of parameters. The prior distribution reflects the knowledge we already have about the parameters. A very broad distribution means that we are rather uncertain about what the parameter value should be. In the case of the eddy diffusivity $\tilde{\kappa}$ and the attenuation coefficient α, we choose a uniform distribution within the range $0 \leq \tilde{\kappa} \leq 5 \times 10^{-4}\,\mathrm{m^2\,s^{-1}}$, respectively $0.05 \leq \alpha \leq 10\,\mathrm{m^{-1}}$. We are fairly certain that the most likely parameter value will lie within these ranges, but choose not to impose any additional prior information. In the case of the mixing coefficient, we have made the experience that we must provide prior information in order to achieve convergence in the likelihood sampling (see below). Thus, we choose a normal distribution with mean $6 \times 10^{-3}\,\mathrm{m\,s^{-1}}$ and standard deviation $1.5 \times 10^{-3}\,\mathrm{m\,s^{-1}}$ as the prior distribution for the mixing coefficient μ. These values are chosen based on manual testing.

6.1.2 MCMC sampling

Having specified a likelihood function and a prior distribution in the three-dimensional parameter space, we are ready to sample from the parameter space in order to approximate the posterior distribution numerically. For this purpose, we use the popular Markov Chain Monte Carlo (MCMC) sampler `emcee`, which is implemented in Python [85]. It is based on the Goodman and Weare algorithm, which we introduced in chapter 2 [42].

We conduct one MCMC run for each of the three trainings sets (Gulf only, Pacific only, and Pacific+Gulf). Each run is initialized from the starting point $(\tilde{\kappa}, \mu, \alpha) = (1 \times 10^{-4}\,\mathrm{m^2\,s^{-1}}, 6 \times 10^{-3}\,\mathrm{m\,s^{-1}}, 4\,\mathrm{m^{-1}})$. For Gulf-only and Pacific-only, we use 16 walkers taking 10000 steps each, whereas in the case of Pacific+Gulf we use 24 walkers at 10000 steps. The Pacific-only simulation stopped after 6804 steps due to a technical error, but the recovered chain was long enough to yield reasonable statistics.

Adaptive interpolation. At each step, each walker must simulate the model for the duration of the training set (around three days) in order to compute the likelihood of the proposed parameter combination. If the proposal is rejected, the model must be simulated again. This makes the MCMC sampling computationally expensive. Moreover, the time step between consecutive data points of around 11 minutes is much too long to meet the CFL condition, if this time step were used in the model. Therefore, we must interpolate the atmospheric input data at sufficiently high time resolution to satisfy the CFL condition, and the model then uses the interpolated data to step forward in time to the next real data point.

Since the CFL number depends on wind speed, the required time resolution of the interpolated data depends on wind. At high winds, we require many model integrations to step forward from one real data point to the next. Initially, we implemented the MCMC sampling in the following way: first, the data was interpolated according to the maximum wind speed and the upper limit of $\tilde{\kappa}$, and this interpolated dataset was then used throughout the sampling. The consequence was a very long simulation time of around

	$\tilde{\kappa}_0$ ($\mathrm{m^2\,s^{-1}}$)	μ ($\mathrm{m\,s^{-1}}$)	α ($\mathrm{m^{-1}}$)	No. walkers	No. steps
Initial	10×10^{-5}	6.00×10^{-3}	4.00		
MAP Gulf	3.48×10^{-5}	5.47×10^{-3}	2.15	16	10000
MAP Pacific	2.62×10^{-5}	5.91×10^{-3}	0.70	16	6804
MAP Gulf+Pacific	7.39×10^{-5}	3.55×10^{-3}	2.31	24	10000

Table 6.1: Maxima of the posterior distributions (MAP) for each Bayesian MCMC run. Initial refers to the parameter values around which the random walkers were initialized. The number of walkers and steps is also shown. The fixed model parameters are $\sigma = 0.8$ and $\lambda = 3\,\mathrm{m}$.

80 seconds per iteration of the MCMC sampler. To address this, we modified the code such that the data was re-interpolated before each likelihood evaluation, using the current value of $\tilde{\kappa}$ with a time step corresponding to a CFL number of 0.95. This sped up the sampling by an order of magnitude.

6.1.3 Posterior distributions

After completion of each run, we have an ensemble of random walks in parameter space. Their position distribution approximates the posterior distribution. The results are shown in figs. 6.2 to 6.7 after cutting off the first 200 steps of each sample as burn-in. The walkers generally converged within the first 100 steps. Since the auto-correlation time of the random walks amounts to around 40 to 50 steps in each of the MCMC simulations, we have roughly 200 independent samples for the Gulf-only and Pacific+Gulf runs. The Pacific-only run consists of a bit more than 100 independent samples. For each of the three training sets, we show corner plots of the posterior distribution as well as a comparison between prior and posterior. As an estimate of the best parameter values, we find the maximum of the histograms that represent the posteriors. This is known as *maximum a posteriori* (MAP) estimation. The MAP values are summarized in table 6.1.

In the case of the Gulf-only and Gulf+Pacific estimations, the MCMC algorithm identifies clear maxima in parameter space. The shapes of the posterior distributions resemble Gaussian distributions, although they are not always completely symmetric. The 2D plots in the corner diagrams illustrate the correlations between parameters. Note that the posterior distribution of μ does not coincide with its prior distribution, meaning that the likelihood estimation added information about the distribution of μ. This is especially true for the Pacific+Gulf case. In the case of the Pacific-only estimation, we see sharp peaks in the posteriors of $\tilde{\kappa}$ and α but also long tails. It seems that the walkers repeatedly explored larger values of $\tilde{\kappa}$ and α, and the convergence to a single parameter value is not as clear. The distribution of μ is largely controlled by the prior in this case. Nonetheless, we can compute unique MAP estimates from this posterior, and we will explore the solution these estimated parameter values yield.

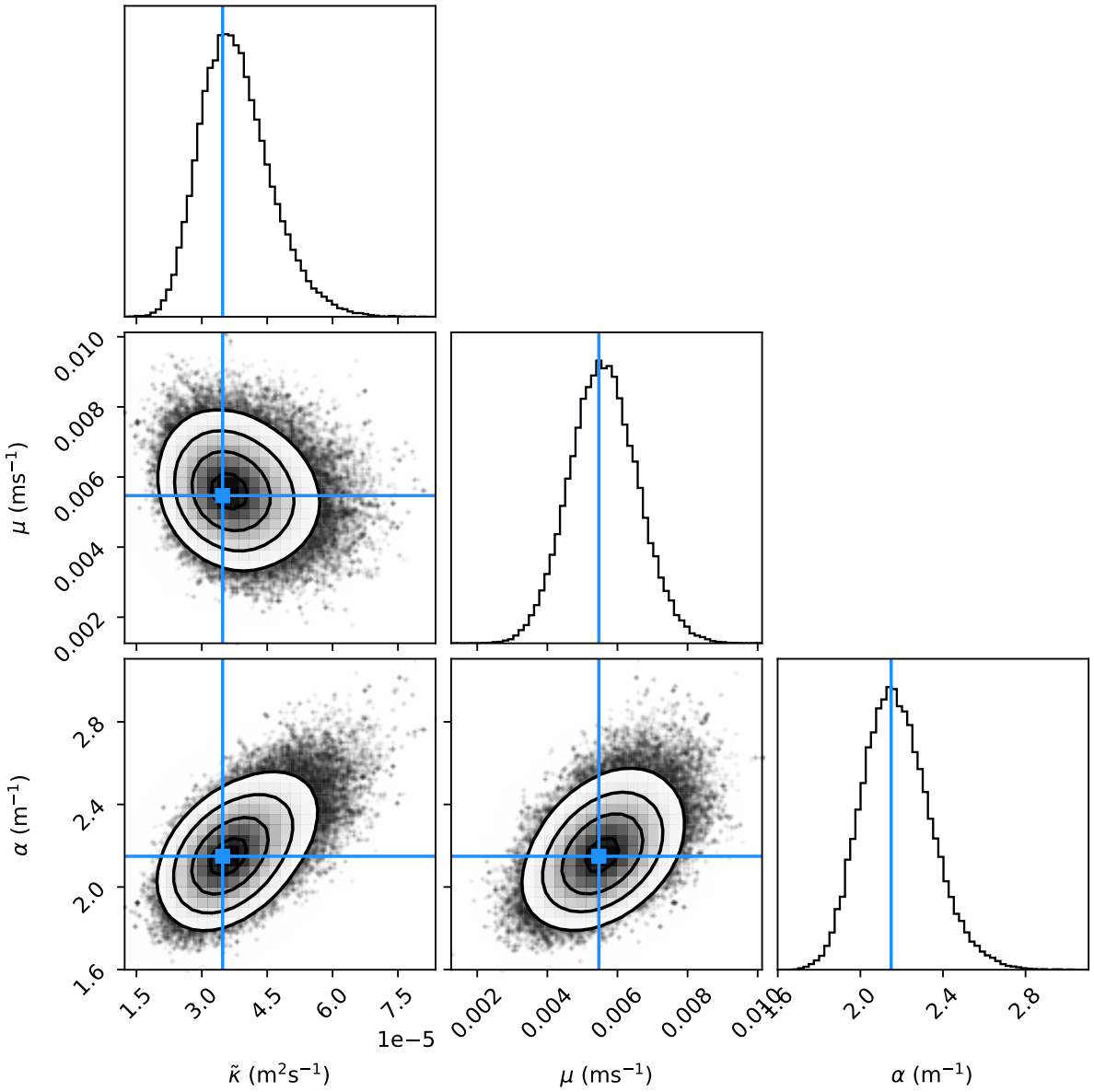

Figure 6.2: Corner plot of the Gulf-only MCMC estimation. On the diagonal, the marginalized posterior distributions are shown for each parameter. The off-diagonal 2D plots illustrate parameter correlations. The blue lines indicate the MAP value.

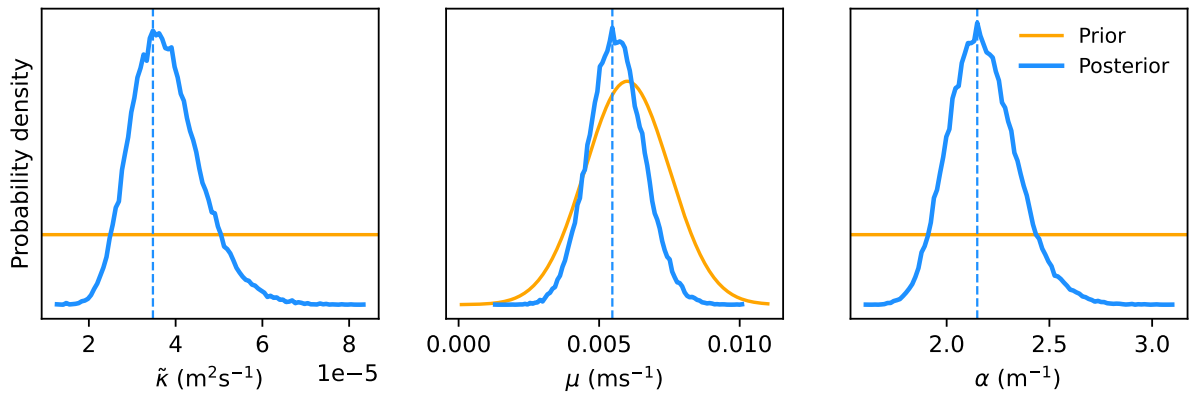

Figure 6.3: Prior and posterior distributions for the Gulf-only run. The blue dashed line indicates the MAP estimate.

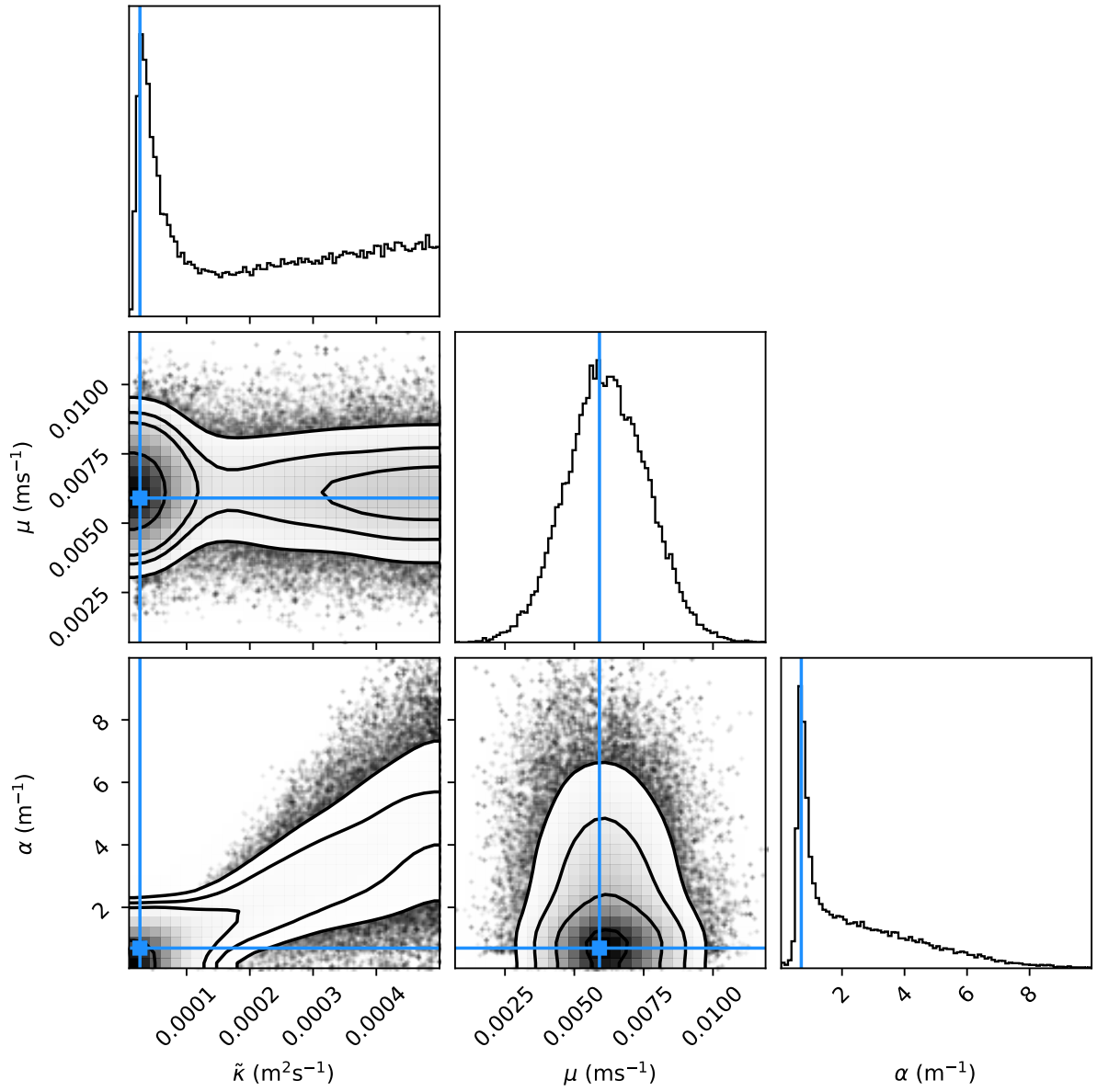

Figure 6.4: Corner plot of the Pacific-only MCMC estimation.

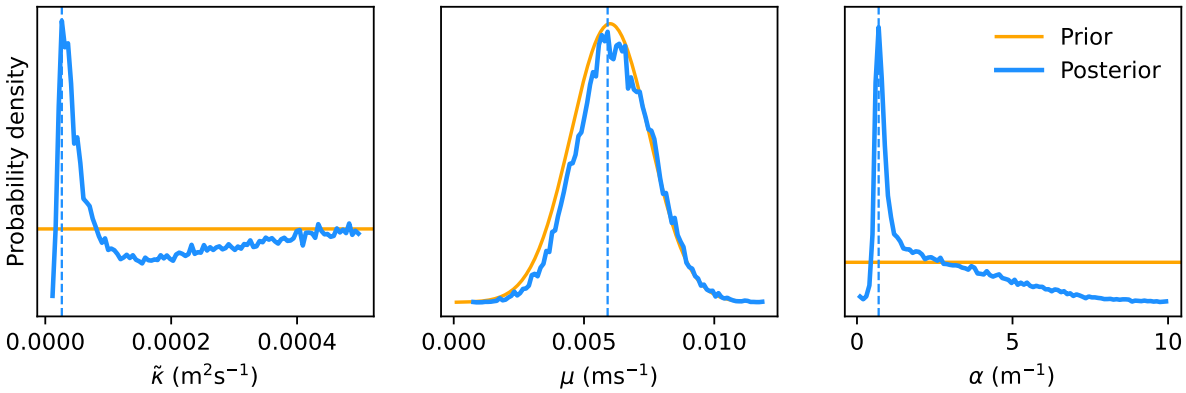

Figure 6.5: Prior and posterior distributions for the Pacific-only run. The blue dashed line indicates the MAP estimate.

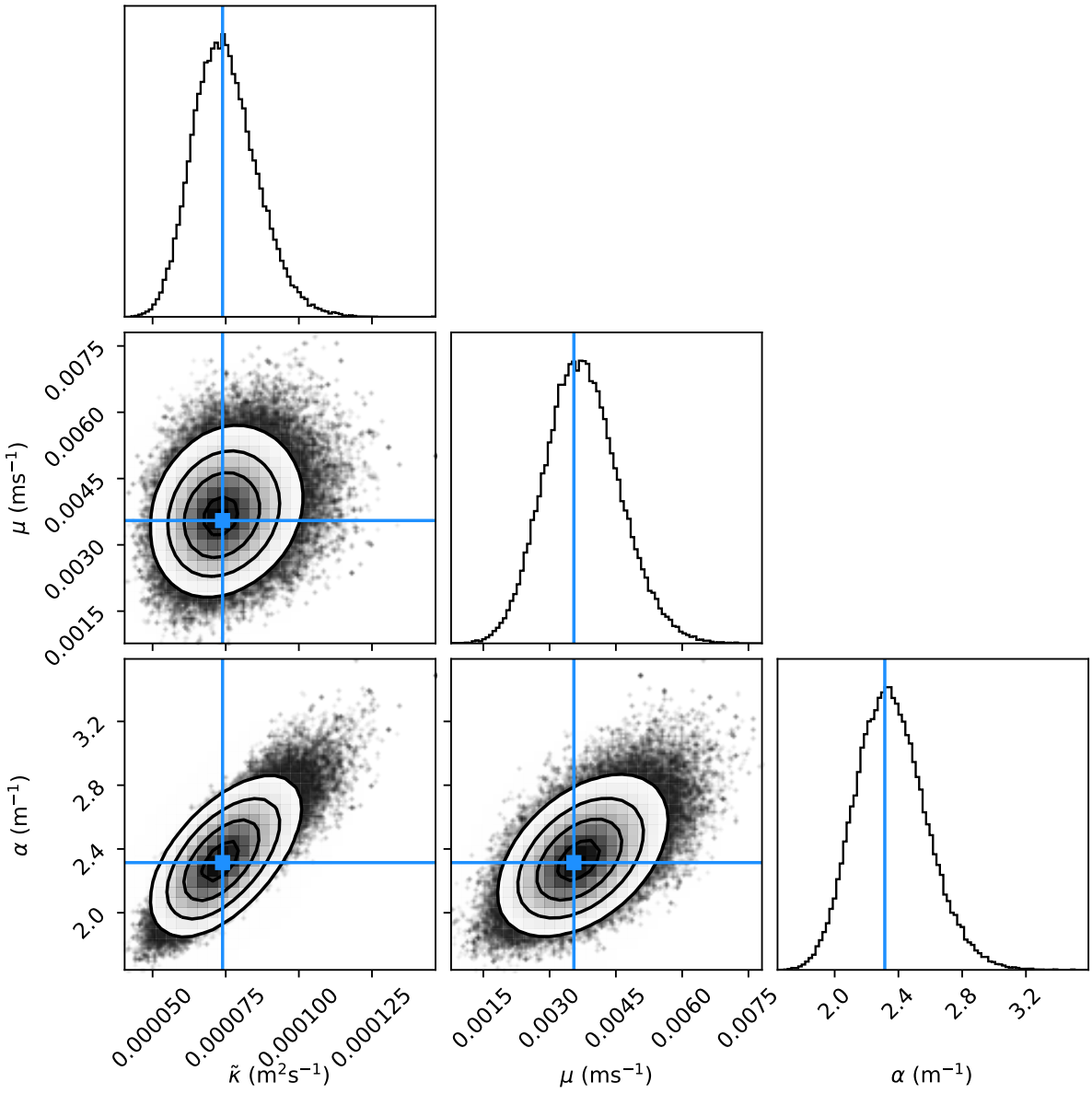

Figure 6.6: Corner plot of the Pacific+Gulf MCMC estimation.

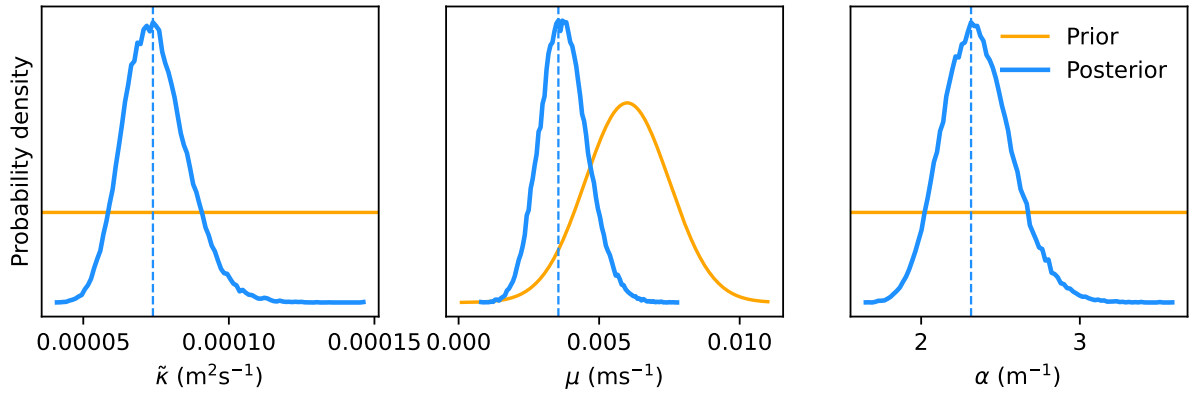

Figure 6.7: Prior and posterior distributions for the Pacific+Gulf run. The blue dashed line indicates the MAP estimate.

6.2 Model vs. observations

Now that we have systematically calculated estimates of the model parameters $\tilde{\kappa}$, μ, and α, let us analyze what happens when we plug these estimates into the model and force it with the atmospheric data observed during the MOCE-5 cruise.

6.2.1 Prior and posterior simulations

Figures 6.8, 6.9, and 6.10 illustrate the results for each of the training sets. We expand the shown time interval to adjacent days before or after the training period, in order to get an idea to which extent the model can predict warming events that it has not been fitted to.

In fig. 6.8, we compare observed ΔSST with the simulated ΔSST using the starting values (referred to as prior) and the MAP values (posterior) of the Gulf-only estimation, respectively. The training interval consists of three days showing three warming events of different magnitude. The MAP simulation underestimates the large warming event on day 13 as well as the warming event on day 15. In fact, the posterior simulation performs worse at capturing the day 13 peak compared to the prior simulation. Possibly, the likelihood function puts little weight on the peak, since it consists of few data points compared to the large number of data points which have lower ΔSST. Both simulations capture the day 14 peak well. Furthermore, especially the posterior simulation performs well at reproducing the slight skin cooling at night. By showing days 10-13, we see that the given choice of parameters also approximates warming events outside of the training interval reasonably well. The peaks on days 10 and 12 are well captured in structure and magnitude, whereas warming on day 11 is overestimated. The depth-time contour plot in the center panel reveals a vertical view of the simulated temperature evolution (using the MAP estimates). It shows that most of the warming is restricted to the top 2 m of the water column. We also see the deepening of the warm layer in the afternoons, e.g. on day 11 or day 14.

Figure 6.9 shows the same as before for the Pacific-only case, which exhibited a somewhat unclear posterior distribution. When inspecting the ΔSST time series, however, we see that the posterior simulation traces the observational data relatively well. In contrast, the prior simulation greatly overestimates the warming on days 6 and 7. The MAP estimates of the Pacific-only case suggest comparatively small values of the eddy diffusivity and

attenuation coefficient. This means that the heat source is more distributed over the water column and there is little vertical mixing. Indeed, the time-depth contour plot indicates that warming and cooling is governed more directly by the surface fluxes and less by internal mixing processes. It remains unclear whether this vertical structure is realistic for the open Pacific ocean or whether it is an unrealistic way of achieving good agreement in the ΔSST signal.

Finally, figure 6.10 illustrates prior and posterior simulations on the entire time span of the cruise dataset. The two training intervals (Pacific on the left, Gulf on the right) are shaded. This time we do not show the corresponding time-depth diagram because the time axis is too squeezed to see much. Here it is remarkable that the model often shows good agreement with the data over a wide range of warming amplitudes, from less than half a Kelvin in the first week to 3 K of warming on day 10. The largest warming event in the data corresponds with the largest warming event in the simulations, even though the posterior simulation underestimates the 5 K peak by more than a Kelvin. The prior distribution in fact captures the warmest peak more accurately but it overestimates other peaks, e.g. on days 6, 7, and 10. The nighttime temperatures are overall captured well.

6.2.2 Wind dependence

Using the original cruise data together with the Pacific+Gulf posterior simulation, let us now investigate the correspondence between model and observation more thoroughly. A critical feature we aim to represent is the wind dependence of the diurnal warming amplitude. In chapter 4, we visualized this characteristic by two scatter plots of the MOCE-5 data (see fig. 4.6). It is interesting to plot the model output in the same way, using the time points of the observational data. The result is shown in fig. 6.11 and compared to the previous result from chapter 4.

Overall, the model and the observations show similar characteristics in these plots. The model output is less noisy than the data, and simulated warming does not exceed 4 K in the present case. However, the wind dependence agrees well between the observations and our model. In both cases, wind speeds of more than $5\,\mathrm{m\,s^{-1}}$ essentially prohibit diurnal warming.

For the cruise data as well as for the buoy records, our data analysis in chapter 4 suggested an exponential relationship between warming amplitude and wind speed. An exponential dependence has also been proposed by other authors, e.g. by Gentemann et al. [36]. This motivates us to investigate whether we also obtain an exponential dependence from our model, and to which extent the exponents are comparable.

To do this, we return to the idealized weather data introduced in section 5.4.1, with peak insolation of $1000\,\mathrm{W\,m^{-2}}$ and a diurnally oscillating air temperature between 299 and 301 K. The specific humidity is set to $10\,\mathrm{g\,kg^{-1}}$. Starting at at wind speed of $0.5\,\mathrm{m\,s^{-1}}$, we now run simulations at increasing wind speed in intervals of $0.5\,\mathrm{m\,s^{-1}}$, until $10\,\mathrm{m\,s^{-1}}$. For each of these simulations, we calculate the maximum of the skin-foundation temperature difference ΔSST as well as the temperature difference $\Delta T(1\mathrm{m})$ between 1m depth and the foundation. The results are plotted in fig. 6.12 as a function of wind speed. Furthermore, we use a least-squares optimizer (`iminuit`) to fit an exponential function to these model data. Visually, an exponential relationship seems plausible. The magnitude of warming is decreased at 1m depth compared to the surface, but there still seems to be an exponential

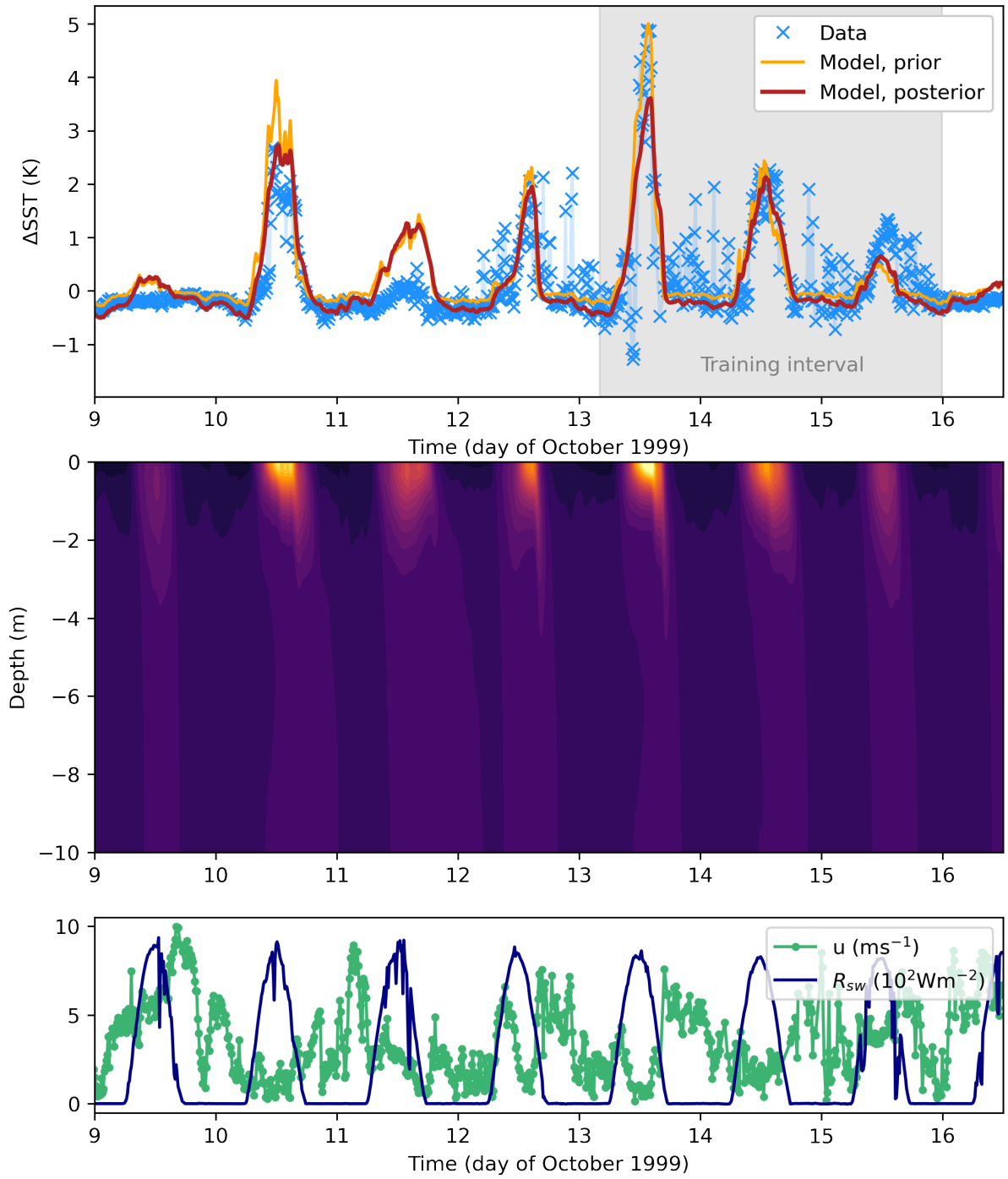

Figure 6.8: Results of the prior and MAP-posterior simulations for the Gulf-only estimation. The grey shaded area indicated the training interval which was used for the MCMC simulation.

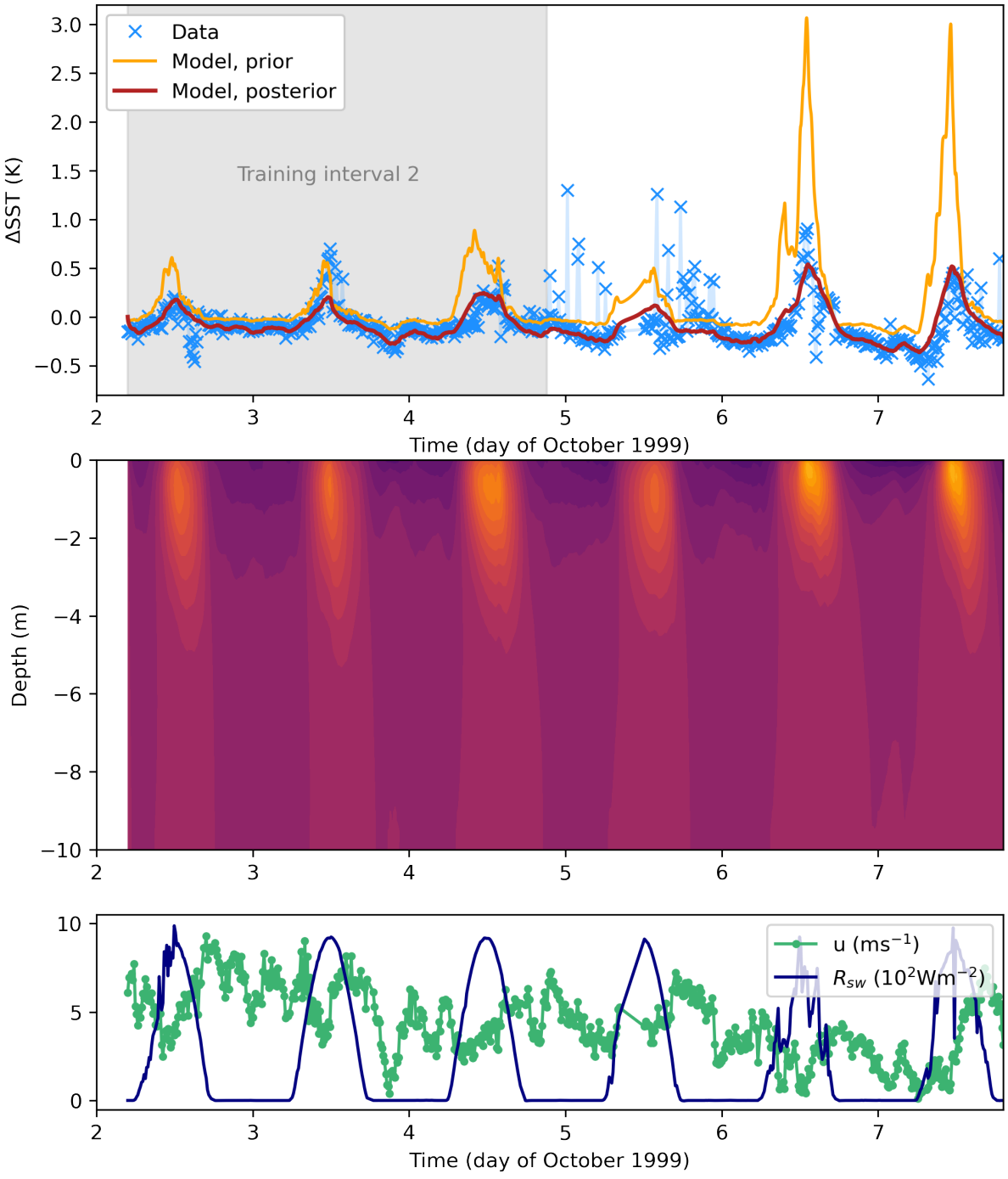

Figure 6.9: Prior and MAP-posterior simulations for the Pacific-only estimation.

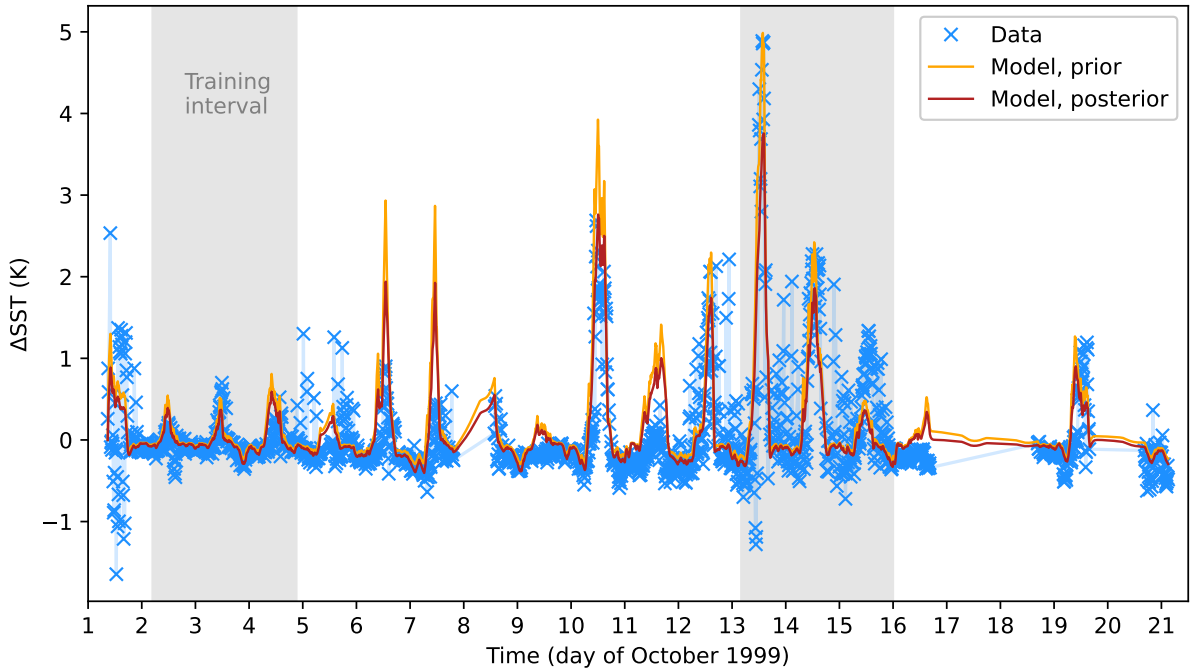

Figure 6.10: rior and MAP-posterior simulations for the Pacific+Gulf estimation.

	intersect y_0	exponent γ	Comment
MOCE-5, ΔSST	3.44	0.52	fig. 4.8
GTMBA buoys, $\Delta T(1\text{m})$	1.32	0.35	fig. 4.14
Gentemann et al. [36], ΔSST		0.53	
Model, ΔSST	6.622	0.63	
Model, $\Delta T(1\text{m})$	2.71	0.38	

Table 6.2: The y intersects and exponents of the diurnal warming amplitude as a function of wind speed, assuming that $\Delta T(u) = y_0 \exp(-\gamma u)$.

decay with wind speed above $2\,\mathrm{m\,s^{-1}}$. Curiously, we see the same decrease in $\Delta T(1\text{m})$ at low wind speeds that we also observed in the buoy data (see fig. 4.14). This could indicate that at low wind speeds the heat is trapped above 1m depth and mainly leaves again through the air-sea interface, e.g. by evaporative cooling.

From the exponential fits performed on the different data, including both observations and model output, we obtain the estimated exponents of amplitude decay with wind speed. The results are summarized in table 6.2. At both depths, our model produces a slightly larger exponent when contrasted with observations. However, the order of magnitude is similar, and the values of the exponents are sensitive to the weight we put on each data point when fitting. For example, if we make the y-error of a point in fig. 6.12 proportional to its value, the fit gives a smaller exponent. In summary we conclude that our model exhibits a similar wind dependence as observations.

6.2.3 Predictive skill

To quantify the level of agreement between our model and the MOCE-5 dataset, we finally show a scatter plot of modeled vs. observed ΔSST. A perfect model would cause all points

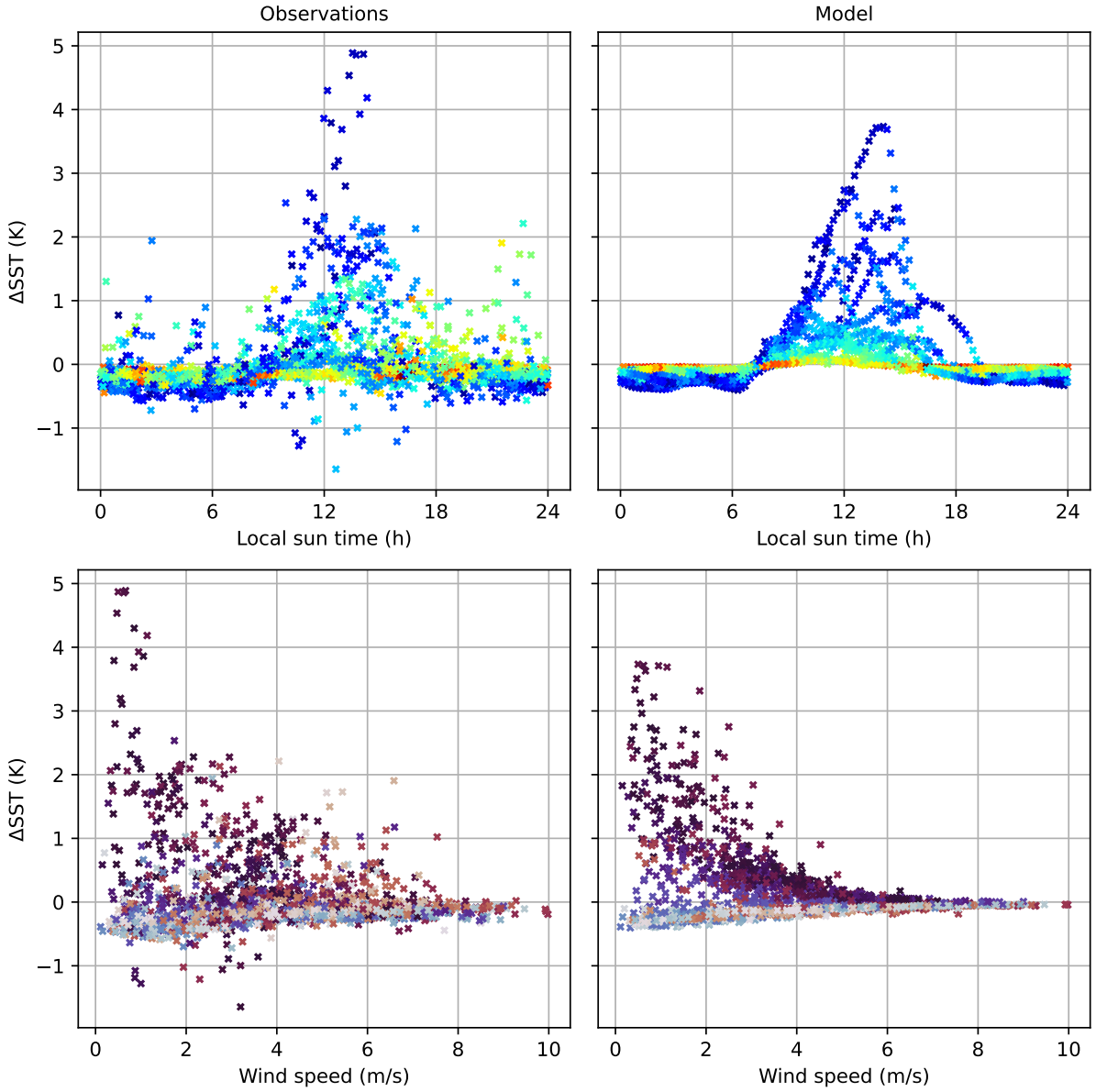

Figure 6.11: Comparison of wind dependence in model and observation. In the top panel, the points are colored by wind speed. In the bottom panel, the points are colored by local sun time. The left column shows the observations from the MOCE-5 cruise, while the right column depicts the corresponding simulated data points from the model.

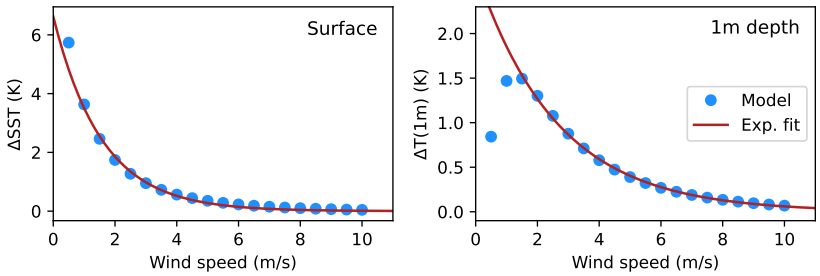

Figure 6.12: Wind dependence of diurnal warming in our model for the posterior simulation based on the Pacific+Gulf estimation. The temperature difference is taken with respect to the foundation temperature at 10m depth.

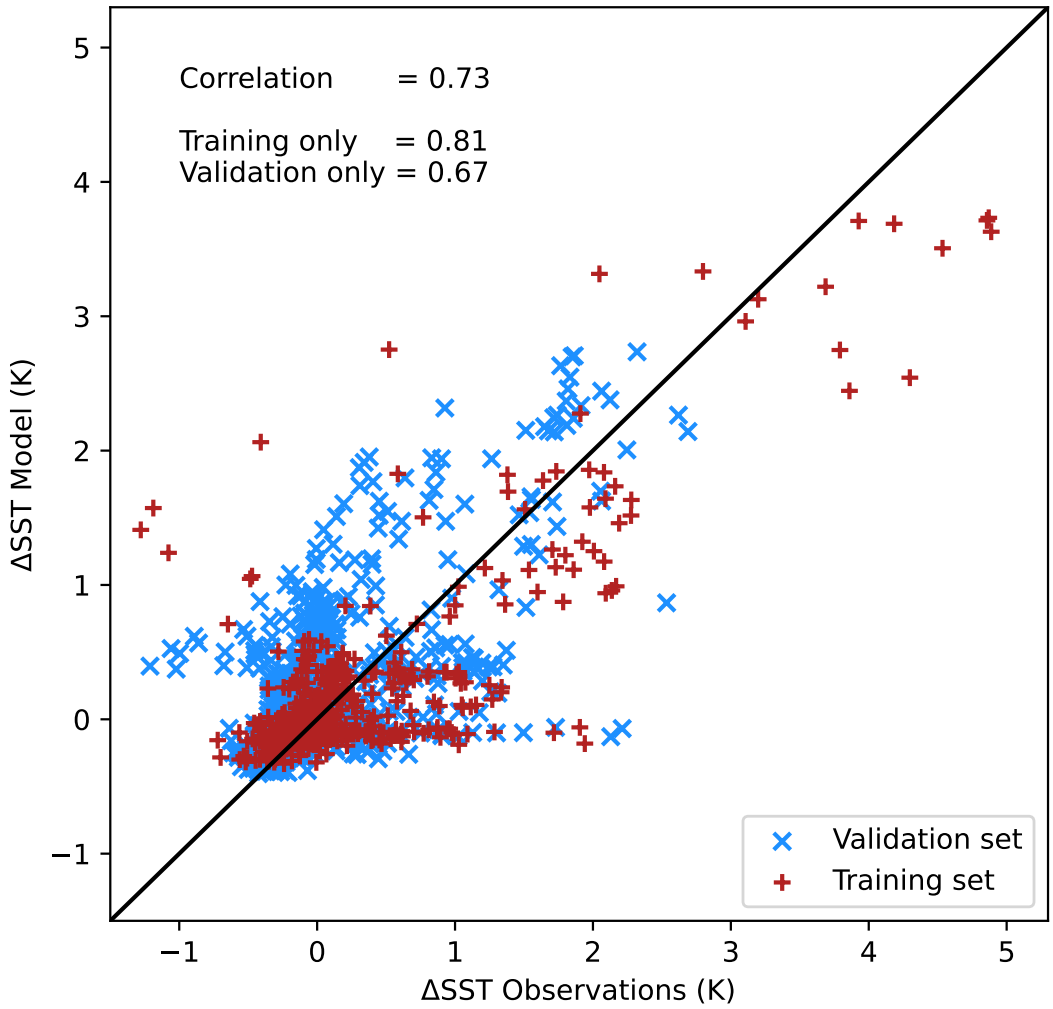

Figure 6.13: Predictive skill of our model based on the MOCE-5 data and Bayesian inference using the Pacific+Gulf intervals.

to lie precisely on the black diagonal line. We differentiate by color between points that were used for Bayesian inference (the training set, Pacific+Gulf) and points that were not (the validation set). For the training set only, we find a Pearson correlation coefficient of 0.73. Unsurprisingly, the validation set agrees less well with the observations, yielding a correlation of 0.67. Altogether, the correlation between model and cruise data amounts to 0.73, which confirms that our model is able to predict the time evolution of diurnal surface warming to a certain degree.

6.3 Better than a slab?

A central argument of this thesis is that slab ocean models may be insufficient as an interactive lower boundary condition in atmospheric simulations, since they neglect wind-

driven mixing processes. However, we have so far not verified this claim. Is our model really better than a single-layer slab? Are mixing processes in the upper ocean crucial to get diurnal sea surface warming right? To answer this question, we implement a slab model as described by eq. (3.14) and force this model with days 9-15 of the MOCE-5 dataset. We also simulate our model with the Pacific+Gulf parameter estimates during the same time interval. The results are illustrated in fig. 6.14.

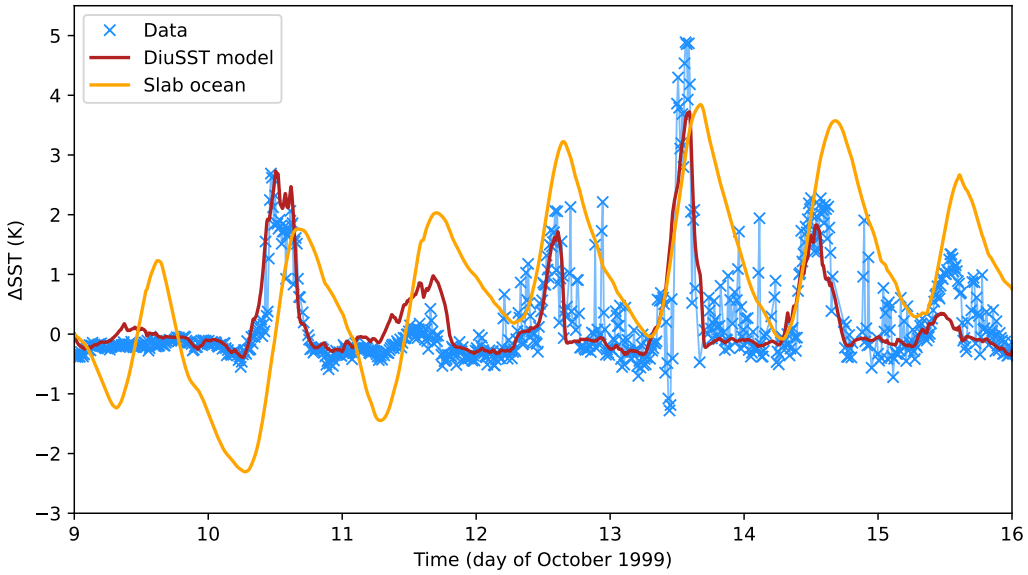

Figure 6.14: Comparison between our model and a standard slab model. For the slab model, a slab depth of 1m and a sink term of $50\,\mathrm{W\,m^{-2}}$ are chosen. The simulation with our model uses the Pacific+Gulf MAP.

The slab model does not describe the variable amplitudes and sharp peaks of warming. In fact, the slab model shows a rather similar day-night amplitude of warming regardless of the wind speed. Stronger wind speed is more reflected in a mean cooling of the slab due to the enhanced surface heat fluxes. While our model, which we call DiuSST here, does not perfectly capture the amplitude of all peaks, it follows the warming and cooling pattern much more closely, making a distinction between windy and calm days.

7 Discussion

Observations. Our observational analysis in the first part of this study relies on a range of datasets, characterized by different conditions and measurement methodologies. Despite this diversity, all datasets show clear signs of diurnal warming of sea surface temperature (SST). Indeed, the diurnal cycle of SST marks a prominent peak in the power spectrum of SST time series. While this has been known before, much of the data analysis presented here is new. Our results thus corroborate earlier findings and provide additional evidence.

One of the key results is that diurnal warming is modulated by a strong wind dependence. Due to enhanced vertical mixing, strong winds prevent diurnal warming. Our analysis suggests an exponential relationship between the amplitude of diurnal warming and the wind speed, in agreement with previous studies [36]. At 1m depth, the exponential dependence interestingly breaks down in the low-wind regime. This could imply that, at winds of less than 1-2 $\mathrm{m\,s^{-1}}$, most of near-surface heat trapping takes place at water depths less than one meter. Slab oceans of several meters thickness or global ocean models, where the uppermost layer is tens to hundreds of meters thick, cannot resolve these dynamics. At the same time, a thin slab will most likely overestimate diurnal warming especially under stronger winds, due to ignoring turbulent heat transport into the deeper ocean. This highlights that slab models cannot adequately represent wind-dependent diurnal surface warming in the ocean.

Despite robust similarities across the different locations studied, we also observe regional and seasonal differences in the SST signals. In the case of the MOCE-5 cruise, there appears to be a distinction between waters inside and outside the Gulf of California. Concretely, the majority of warming events above 1 K occur within the Gulf area. Is this a coastal phenomenon? Are the optical properties different inside the Gulf, leading to increased solar absorption near the surface? This could be the case, for example, if there is a high chlorophyll concentration. Or can this difference be traced back to the wind dependence, because the wind is stronger over the open ocean? The same question arises regarding the annual variability of the diurnal SST amplitude which we discover at the ATLANTIC buoy. Its annual cycle seems synchronized with an annual cycle in wind speed, but it is not clear whether the wind pattern alone can explain the interannual variability of diurnal SST variation. Answering these questions requires further investigation, which lies beyond the scope of this thesis.

Another important feature of diurnal warming involves the deepening of the warm layer. Under calm conditions, heat is trapped near the surface until noon and then diffused downwards in the afternoon, which implies that peak warming occurs later with increasing depth. When developing our model, we put an emphasis on reproducing this time-asymmetry. Not only the phase shift of warming but also the amplitude of warming depends significantly on depth. This makes it difficult to compare the radiometric cruise data with the buoy records which have their upper-most thermometer at 1m depth. Our crude extrapolation method indicates that at the buoy locations, SST warming is probably

significantly larger than the warming recorded 1m below. Since the atmosphere senses only the ocean's skin, we emphasize the importance to use skin SST measurements when calibrating ocean models for use in atmospheric simulations.

Modeling assumptions. Our modeling approach is highly idealized an thus involves numerous simplifying assumptions. Firstly, we assume scale separation between the diurnal near-surface SST dynamics and the low-frequency variation of the upper ocean. By making the problem one-dimensional and removing any equation for horizontal flow, we further assume that we can neglect horizontal currents, including tidal flows[1]. Moreover, we assume a flat sea surface, ignoring wave breaking, Langmuir circulations, and wave spray. By making the diffusivity a direct function of wind speed, we implicitly assume that turbulent mixing varies instantly with wind changes. In reality however, we expect that turbulent mixing will have a certain inertia after the wind drops, such that strong diurnal warming would not be possible immediately after a sharp drop in wind speed. In fact, near-by storms could remotely mix surrounding waters through the propagation of gravity waves. Regarding solar absorption, we make a highly simplified choice by assuming a constant attenuation coefficient independent of wavelength. In reality, the attenuation coefficient varies with frequency and depends strongly on the optical properties of the sea water, which may vary with time.

Modeling approach. Yet, our goal is not to model a plethora of specific situations accurately, but rather to develop a model that behaves like an average, generic tropical sea surface. This is what we need for idealized cloud-resolving simulations, which we may likewise view as generic representations of the tropical atmosphere. From this general perspective, two factors appear to dominate in determining the evolution of SST on diurnal timescales: the incoming radiation and the wind-driven turbulent mixing processes. By capturing these two processes, our model significantly outperforms a single-layer slab. Another advantage of our model is that the depth-dependence of warming follows from the mixing processes, rather than being imposed by an artificial temperature profile. However, the choice of eddy diffusivity profile is rather arbitrary, and it is not clear which option is the best to take. We base our choice on comparisons with the available data.

Datasets The key advantage of the MOCE-5 cruise dataset is that it contains simultaneous records of bulk sea temperature at 3 m depth and SST directly at the skin, combined with important atmospheric data such as wind speed, air temperature, and solar radiation. This allows us to force the model with atmospheric data and compare the simulated skin temperature difference ΔSST with the observed skin-bulk temperature difference. Unfortunately, humidity data are missing in the available dataset, leading to an error in the modeled latent heat flux. Moreover, the time series is rather short, and the research vessel often moves around during the measurements. This leads to temperature changes and currents that would not be present at a fixed location.

Bayesian inference. When performing the Bayesian inference, we make the following assumptions:

[1]Given the 12-h peak in the SST power spectrum at the ATLANTIC buoy, lateral heat transport due to tides may not be negligible in some regions.

- The position of the ship does not affect the value of model parameters (translational invariance)
- Temporal changes of foundation temperature can be neglected, because they originate either from advection of cold water masses or from the boat transsecting into different water masses.
- The observed warming of SST is due to air-sea interactions and not due to internal ocean dynamics (such as a sudden cool current at the foundation depth).

Sometimes, the prior distribution obtained by human fine-tuning captures the amplitudes of the large peaks better than the Bayesian posterior distribution. This is probably because the human eye focuses on the peaks, whereas the likelihood function evaluates all points equally according to their weight. A single peak is then less important in the likelihood compared to many points without diurnal warming at night. To put more emphasis on the peaks, the errors of the individual data points could be changed.

The Bayesian inference does not succeed at estimating smooth posterior distributions for all parameters simultaneously, because the likelihood function is only computed based on a temperature difference between two depths. To constrain the parameters more efficiently, we would probably need to include more information about the vertical profile in the likelihood function.

To obatain more robust estimates, it would be desirable to re-perform the Bayesian inference based on a dataset recorded at a fixed location, including air humidity data and further temperature measurements at depth. We imagine that this would also yield a clear posterior distributions for the mixing coefficient μ, which acts at greater depth. Perhaps observational data from the recent EUREC4A campaign can provide the timeseries of interest.

Suitability as a surface boundary condition. Our model is easy to code and fast enough to be coupled to a cloud-resolving model without adding too much additional computation time. We hope to couple the model to the SAM model in future work. However, since the atmosphere is only interested in the skin temperature, it might not be necessary to compute the entire depth dependence of the diurnal layer at each simulation time step. Instead, the results of this thesis and our knowledge of the exponential form of the wind dependence of warming could be used to derive an even simpler parametrized model that does not require solving a PDE. For example, a single layer slab model could accurately include the effect of wind-driven mixing if the slab depth can vary with time. This approach has already been used in some upper ocean models using a Richardson number criterion that determines the time evolution of slab depth.

Extensions. An important aspect which our model currently neglects is precipitation. When it rains, the light freshwater film at the surface increases stable stratification, which can lead to enhanced surface warming after a rain event. In principle, this effect could be included in the stratification factor.

8 Conclusion & Outlook

This work presents an idealized model of diurnal sea surface warming in the tropical ocean.

In the first part, we conduct an analysis of observational data in order to investigate the key features of diurnal sea surface temperature variation in the tropical ocean. The primary dataset includes around two weeks of radiometric and meteorological data from the MOCE-5 cruise, conducted in October 1999 near the Mexican west coast. In addition, we consider buoy records from three different locations in the tropical ocean, of which two buoys lie in the Pacific and the third is located near Western Africa. Our results confirm that diurnal warming constitutes a dominant mode of SST variability, and that warming amplitudes at the sea skin can reach up to 5K under calm and clear conditions. However, the amount of warming strongly depends on the wind speed, and we find that the mean amplitude of warming decays exponentially with wind speed.

Inspired by the heat equation, we next build a multilayer model that describes heat transport in the upper few meters of the ocean under atmospheric forcing of insolation, wind speed, air temperature, and humidity. In addition to the turbulent diffusion term, we include a second mixing term which represent the interaction with the water column below the simulation domain. This leads to eq. (5.1):

$$\frac{\partial T}{\partial t} = \underbrace{\kappa(t)\frac{\partial^2 T}{\partial z^2}}_{\text{diffusion}} - \underbrace{\mu\frac{T - T_f}{|z - z_f|}}_{\text{mixing}} + \underbrace{\frac{1}{\rho_w c_p}\frac{\partial Q(z,t)}{\partial z}}_{\text{source}} \quad . \tag{8.1}$$

We investigate the behavior of the model under different parameter combinations and test the effect of different diffusivity profiles on the spatio-temporal temperature pattern.

Combining the observations with our model, we perform Bayesian inference to estimate the best parameters. Using the maximum a posteriori estimate, we then compare the simulated temperature evolution with the corresponding observed time series. We show that our model is capable of reproducing and predicting key features of diurnal sea surface warming. Importantly, we accurately capture the exponential wind dependence of the magnitude of warming.

Our model has been designed with the aim to be suitable as an interactive surface boundary condition for high-resolution, idealized simulations of the tropical atmosphere. We demonstrate that our model significantly outperforms standard slab ocean models which have recently been used as oceanic boundary conditions. Given the renewed interest in atmospheric simulations with more realistic air-sea interactions, we hope that our work may contribute to new avenues of research that seek to unravel the fascinating complexity of convective organization in a coupled ocean-atmosphere system.

References

[1] R. Knutti, M. A. A. Rugenstein, and G. C. Hegerl, "Beyond equilibrium climate sensitivity", en, *Nature Geosci*, vol. 10, no. 10, pp. 727–736, 2017. DOI: 10.1038/ngeo3017.

[2] T. Schneider, J. Teixeira, C. S. Bretherton, *et al.*, "Climate goals and computing the future of clouds", en, *Nature Climate Change*, vol. 7, no. 1, pp. 3–5, 2017. DOI: 10.1038/nclimate3190.

[3] S. Bony, B. Stevens, D. M. W. Frierson, *et al.*, "Clouds, circulation and climate sensitivity", en, *Nature Geoscience*, vol. 8, no. 4, pp. 261–268, 2015. DOI: 10.1038/ngeo2398.

[4] A. P. Siebesma, S. Bony, C. Jakob, *et al.*, *Clouds and Climate: Climate Science's Greatest Challenge*. Cambridge University Press, 2020.

[5] B. Khouider, *Models for tropical climate dynamics: waves, clouds, and precipitation*. Springer, 2019, vol. 3.

[6] I. M. Held, R. S. Hemler, and V. Ramaswamy, "Radiative-convective equilibrium with explicit two-dimensional moist convection", *Journal of Atmospheric Sciences*, vol. 50, no. 23, pp. 3909–3927, 1993.

[7] A. M. Tompkins and G. C. Craig, "Radiative–convective equilibrium in a three-dimensional cloud-ensemble model", en, *Quarterly Journal of the Royal Meteorological Society*, vol. 124, no. 550, pp. 2073–2097, 1998. DOI: https://doi.org/10.1002/qj.49712455013.

[8] C. S. Bretherton, P. N. Blossey, and M. Khairoutdinov, "An energy-balance analysis of deep convective self-aggregation above uniform SST", *Journal of the atmospheric sciences*, vol. 62, no. 12, pp. 4273–4292, 2005.

[9] C. E. Holloway, A. A. Wing, S. Bony, *et al.*, *Observing Convective Aggregation*, 6. Springer Netherlands, 2017, vol. 38. DOI: 10.1007/s10712-017-9419-1.

[10] Y. Kawai and A. Wada, "Diurnal sea surface temperature variation and its impact on the atmosphere and ocean: A review", en, *J Oceanogr*, vol. 63, no. 5, pp. 721–744, 2007. DOI: 10.1007/s10872-007-0063-0.

[11] Z. Sharifnezhadazizi, H. Norouzi, S. Prakash, *et al.*, "A Global Analysis of Land Surface Temperature Diurnal Cycle Using MODIS Observations", EN, *Journal of Applied Meteorology and Climatology*, vol. 58, no. 6, pp. 1279–1291, 2019. DOI: 10.1175/JAMC-D-18-0256.1.

[12] J. O. Haerter, B. Meyer, and S. B. Nissen, "Diurnal self-aggregation", *npj Clim. Atmos. Sci.*, vol. 3, no. 1, pp. 1–11, 2020. DOI: 10.1038/s41612-020-00132-z.

[13] G. G. Jensen, R. Fiévet, and J. O. Haerter, "The diurnal path to persistent convective self-aggregation", en, *arXiv:2104.01132 [nlin, physics:physics]*, 2021.

[14] S. K. Müller and C. Hohenegger, "Self-Aggregation of Convection in Spatially Varying Sea Surface Temperatures", en, *Journal of Advances in Modeling Earth Systems*, vol. 12, no. 1, e2019MS001698, 2020. DOI: https://doi.org/10.1029/2019MS001698.

[15] S. Shamekh, C. Muller, J.-P. Duvel, *et al.*, "How do ocean warm anomalies favor the aggregation of deep convective clouds?", *Journal of the Atmospheric Sciences*, vol. 77, no. 11, pp. 3733–3745, 2020.

[16] W. G. Large, J. C. McWilliams, and S. C. Doney, "Oceanic vertical mixing: A review and a model with a nonlocal boundary layer parameterization", en, *Rev. Geophys.*, vol. 32, no. 4, p. 363, 1994. DOI: 10.1029/94RG01872.

[17] J. F. Price, R. A. Weller, and R. Pinkel, "Diurnal cycling: Observations and models of the upper ocean response to diurnal heating, cooling, and wind mixing", en, *J. Geophys. Res.*, vol. 91, no. C7, p. 8411, 1986. DOI: 10.1029/JC091iC07p08411.

[18] A. Soloviev and R. Lukas, "Observation of large diurnal warming events in the near-surface layer of the western equatorial Pacific warm pool", en, *Deep Sea Research Part I: Oceanographic Research Papers*, vol. 44, no. 6, pp. 1055–1076, 1997. DOI: 10.1016/S0967-0637(96)00124-0.

[19] R. R. Weihs and M. A. Bourassa, "Modeled diurnally varying sea surface temperatures and their influence on surface heat fluxes", en, *Journal of Geophysical Research: Oceans*, vol. 119, no. 7, pp. 4101–4123, 2014. DOI: https://doi.org/10.1002/2013JC009489.

[20] S. J. Woolnough, F. Vitart, and M. A. Balmaseda, "The role of the ocean in the Madden–Julian Oscillation: Implications for MJO prediction", en, *Q.J.R. Meteorol. Soc.*, vol. 133, no. 622, pp. 117–128, 2007. DOI: 10.1002/qj.4.

[21] A. M. Tompkins, "On the relationship between tropical convection and sea surface temperature", *Journal of climate*, vol. 14, no. 5, pp. 633–637, 2001.

[22] C. Hohenegger and B. Stevens, "Coupled radiative convective equilibrium simulations with explicit and parameterized convection", en, *Journal of Advances in Modeling Earth Systems*, vol. 8, no. 3, pp. 1468–1482, 2016. DOI: https://doi.org/10.1002/2016MS000666.

[23] A. M. Tompkins and A. G. Semie, "Impact of a mixed ocean layer and the diurnal cycle on convective aggregation", en, *J Adv Model Earth Syst*, 2021. DOI: 10.1029/2020MS002186.

[24] S. Shamekh, C. Muller, J.-P. Duvel, *et al.*, "Self-Aggregation of Convective Clouds With Interactive Sea Surface Temperature", *Journal of Advances in Modeling Earth Systems*, vol. 12, no. 11, e2020MS002164, 2020.

[25] J. Kondo, Y. Sasano, and T. Ishii, "On Wind-Driven Current and Temperature Profiles with Diurnal Period in the Oceanic Planetary Boundary Layer", EN, *Journal of Physical Oceanography*, vol. 9, no. 2, pp. 360–372, 1979. DOI: 10.1175/1520-0485(1979)009<0360:OWDCAT>2.0.CO;2.

[26] G. L. Mellor and T. Yamada, "Development of a turbulence closure model for geophysical fluid problems", en, *Reviews of Geophysics*, vol. 20, no. 4, pp. 851–875, 1982. DOI: https://doi.org/10.1029/RG020i004p00851.

[27] L. H. Kantha and C. A. Clayson, "An improved mixed layer model for geophysical applications", en, *Journal of Geophysical Research: Oceans*, vol. 99, no. C12, pp. 25 235–25 266, 1994. DOI: https://doi.org/10.1029/94JC02257.

[28] Y. Noh and H. Jin Kim, "Simulations of temperature and turbulence structure of the oceanic boundary layer with the improved near-surface process", en, *J. Geophys. Res.*, vol. 104, no. C7, pp. 15 621–15 634, 1999. DOI: 10.1029/1999JC900068.

[29] C. W. Fairall, E. F. Bradley, J. S. Godfrey, *et al.*, "Cool-skin and warm-layer effects on sea surface temperature", en, *J. Geophys. Res.*, vol. 101, no. C1, pp. 1295–1308, 1996. DOI: 10.1029/95JC03190.

[30] C. L. Gentemann, P. J. Minnett, and B. Ward, "Profiles of ocean surface heating (POSH): A new model of upper ocean diurnal warming", *J. Geophys. Res.*, vol. 114, no. C7, p. C07017, 2009. DOI: 10.1029/2008JC004825.

[31] X. Zeng and A. Beljaars, "A prognostic scheme of sea surface skin temperature for modeling and data assimilation", en, *Geophysical Research Letters*, vol. 32, no. 14, 2005. DOI: https://doi.org/10.1029/2005GL023030.

[32] P. J. Webster, C. A. Clayson, and J. A. Curry, "Clouds, radiation, and the diurnal cycle of sea surface temperature in the tropical western Pacific", *J. Clim.*, vol. 9, no. 8, 1996. DOI: 10.1175/1520-0442(1996)009<1712:CRATDC>2.0.CO;2.

[33] Y. Kawai and H. Kawamura, "Evaluation of the diurnal warming of sea surface temperature using satellite-derived marine meteorological data", *Journal of Oceanography*, vol. 58, no. 6, pp. 805–814, 2002.

[34] J. F. Price, R. A. Weller, C. M. Bowers, *et al.*, "Diurnal response of sea surface temperature observed at the long-term upper ocean study (34°N, 70°W) in the Sargasso Sea", en, *Journal of Geophysical Research: Oceans*, vol. 92, no. C13, pp. 14 480–14 490, 1987. DOI: https://doi.org/10.1029/JC092iC13p14480.

[35] X. Zeng, M. Zhao, R. E. Dickinson, *et al.*, "A multiyear hourly sea surface skin temperature data set derived from the TOGA TAO bulk temperature and wind speed over the tropical Pacific", en, *J. Geophys. Res.*, vol. 104, no. C1, pp. 1525–1536, 1999. DOI: 10.1029/1998JC900060.

[36] C. L. Gentemann, C. J. Donlon, A. Stuart-Menteth, *et al.*, "Diurnal signals in satellite sea surface temperature measurements", en, *Geophysical Research Letters*, vol. 30, no. 3, 2003. DOI: https://doi.org/10.1029/2002GL016291.

[37] A. Gelman, J. B. Carlin, H. S. Stern, *et al.*, *Bayesian Data Analysis*. CRC Press, 2013.

[38] L. Held and D. Sabanés Bové, *Likelihood and Bayesian Inference: With Applications in Biology and Medicine*, en, ser. Statistics for Biology and Health. Berlin, Heidelberg: Springer Berlin Heidelberg, 2020. DOI: 10.1007/978-3-662-60792-3.

[39] R. Fiévet, V. Raman, and A. H. Auslender, "Data-Driven One-Dimensional Modeling of Pseudoshocks", en, *Journal of Propulsion and Power*, vol. 35, no. 2, pp. 313–327, 2019. DOI: 10.2514/1.B37175.

[40] N. Metropolis, "The beginning of the Monte Carlo method", *Los Alamos Science*, vol. 15, no. 584, pp. 125–130, 1987.

[41] C. Miller, "Markov chain Monte Carlo sampling", in *Practical Astrostatistics*, 2018.

[42] J. Goodman and J. Weare, "Ensemble samplers with affine invariance", en, *CAMCoS*, vol. 5, no. 1, pp. 65–80, 2010. DOI: 10.2140/camcos.2010.5.65.

[43] E. Bodenschatz, W. Pesch, and G. Ahlers, "Recent Developments in Rayleigh-Bénard Convection", en, *Annu. Rev. Fluid Mech.*, vol. 32, no. 1, pp. 709–778, 2000. DOI: 10.1146/annurev.fluid.32.1.709.

[44] D. Samanta, K. B. Karnauskas, and N. F. Goodkin, "Tropical Pacific SST and ITCZ Biases in Climate Models: Double Trouble for Future Rainfall Projections?", en, *Geophysical Research Letters*, vol. 46, no. 4, pp. 2242–2252, 2019. DOI: https://doi.org/10.1029/2018GL081363.

[45] B. Oueslati and G. Bellon, "The double ITCZ bias in CMIP5 models: Interaction between SST, large-scale circulation and precipitation", *Climate dynamics*, vol. 44, no. 3-4, pp. 585–607, 2015.

[46] R. A. Madden and P. R. Julian, "Description of global-scale circulation cells in the tropics with a 40–50 day period", *Journal of Atmospheric Sciences*, vol. 29, no. 6, pp. 1109–1123, 1972.
[47] C. Zhang, "Madden-Julian Oscillation", *Reviews of Geophysics*, vol. 43, no. 2, 2005.
[48] J.-Y. Hsu, H. Hendon, M. Feng, *et al.*, "Magnitude and Phase of Diurnal SST Variations in the ACCESS-S1 Model During the Suppressed Phase of the MJOs", en, *Journal of Geophysical Research: Oceans*, vol. 124, no. 12, pp. 9553–9571, 2019. DOI: https://doi.org/10.1029/2019JC015458.
[49] P. Markowski and Y. Richardson, "Mesoscale Meteorology in Midlatitudes", *Mesoscale Meteorol. Midlatitudes*, pp. 1–407, 2010. DOI: 10.1002/9780470682104.
[50] J. O. Haerter, "Convective Self-Aggregation As a Cold Pool-Driven Critical Phenomenon", *Geophys. Res. Lett.*, vol. 46, no. 7, pp. 4017–4028, 2019. DOI: 10.1029/2018GL081817.
[51] H. F. Fuglestvedt and J. O. Haerter, "Cold pools as conveyor belts of moisture", *Geophysical Research Letters*, vol. 47, no. 12, e2020GL087319, 2020.
[52] J. Edson, T. Crawford, J. Crescenti, *et al.*, "The coupled boundary layers and air–sea transfer experiment in low winds", *Bulletin of the American Meteorological Society*, vol. 88, no. 3, pp. 341–356, 2007.
[53] A. B. Kara, A. J. Wallcraft, E. J. Metzger, *et al.*, "Wind Stress Drag Coefficient over the Global Ocean", EN, *Journal of Climate*, vol. 20, no. 23, pp. 5856–5864, 2007. DOI: 10.1175/2007JCLI1825.1.
[54] M. F. Cronin, C. L. Gentemann, J. Edson, *et al.*, "Air-Sea Fluxes With a Focus on Heat and Momentum", English, *Front. Mar. Sci.*, vol. 6, 2019. DOI: 10.3389/fmars.2019.00430.
[55] K. Stamnes, G. E. Thomas, and J. J. Stamnes, *Radiative Transfer in the Atmosphere and Ocean*, 2nd ed. Cambridge: Cambridge University Press, 2017. DOI: 10.1017/9781316148549.
[56] S. A. Josey, D. Oakley, and R. W. Pascal, "On estimating the atmospheric longwave flux at the ocean surface from ship meteorological reports", en, *Journal of Geophysical Research: Oceans*, vol. 102, no. C13, pp. 27 961–27 972, 1997. DOI: https://doi.org/10.1029/97JC02420.
[57] C. A. Friehe and K. F. Schmitt, "Parameterization of air-sea interface fluxes of sensible heat and moisture by the bulk aerodynamic formulas", *Journal of Physical Oceanography*, vol. 6, no. 6, pp. 801–809, 1976.
[58] J. DeCosmo, K. B. Katsaros, S. D. Smith, *et al.*, "Air-sea exchange of water vapor and sensible heat: The Humidity Exchange Over the Sea (HEXOS) results", en, *Journal of Geophysical Research: Oceans*, vol. 101, no. C5, pp. 12 001–12 016, 1996. DOI: https://doi.org/10.1029/95JC03796.
[59] Y. Noh, H. S. Min, and S. Raasch, "Large Eddy Simulation of the Ocean Mixed Layer: The Effects of Wave Breaking and Langmuir Circulation", EN, *Journal of Physical Oceanography*, vol. 34, no. 4, pp. 720–735, 2004. DOI: 10.1175/1520-0485(2004)034<0720:LESOTO>2.0.CO;2.
[60] Y. Noh, E. Lee, D.-H. Kim, *et al.*, "Prediction of the diurnal warming of sea surface temperature using an atmosphere-ocean mixed layer coupled model", en, *J. Geophys. Res.*, vol. 116, no. C11, p. C11023, 2011. DOI: 10.1029/2011JC006970.
[61] R. B. Stull and E. B. Kraus, "The transilient model of the upper ocean", *Journal of Geophysical Research: Oceans*, vol. 92, no. C10, pp. 10 745–10 755, 1987.

[62] Y. Kawai and H. Kawamura, "Study on a Platform Effect in the In Situ Sea Surface Temperature Observations under Weak Wind and Clear Sky Conditions Using Numerical Models", EN, *Journal of Atmospheric and Oceanic Technology*, vol. 17, no. 2, pp. 185–196, 2000. DOI: 10.1175/1520-0426(2000)017<0185:SOAPEI>2.0.CO;2.

[63] J. F. Price, C. N. K. Mooers, and J. C. V. Leer, "Observation and Simulation of Storm-Induced Mixed-Layer Deepening", EN, *Journal of Physical Oceanography*, vol. 8, no. 4, pp. 582–599, 1978. DOI: 10.1175/1520-0485(1978)008<0582:OASOSI>2.0.CO;2.

[64] Y. Takaya, J.-R. Bidlot, A. C. M. Beljaars, *et al.*, "Refinements to a prognostic scheme of skin sea surface temperature", en, *J. Geophys. Res.*, vol. 115, no. C6, p. C06009, 2010. DOI: 10.1029/2009JC005985.

[65] W. Li, R. Yu, H. Liu, *et al.*, "Impacts of diurnal cycle of SST on the intraseasonal variation of surface heat flux over the western Pacific warm pool", *Advances in Atmospheric Sciences*, vol. 18, no. 5, pp. 793–806, 2001.

[66] E. C. Kent, J. J. Kennedy, D. I. Berry, *et al.*, "Effects of instrumentation changes on sea surface temperature measured in situ", en, *WIREs Climate Change*, vol. 1, no. 5, pp. 718–728, 2010. DOI: 10.1002/wcc.55.

[67] K. Hosoda, "A review of satellite-based microwave observations of sea surface temperatures", en, *J Oceanogr*, vol. 66, no. 4, pp. 439–473, 2010. DOI: 10.1007/s10872-010-0039-3.

[68] "NOAA Coral Reef Watch Daily Global 5km Satellite Coral Bleaching Heat Stress SST Product (Version 3.1)". (), [Online]. Available: https://coralreefwatch.noaa.gov/product/5km/index_5km_sst.php (visited on 08/10/2021).

[69] F. J. Wentz, "Satellite Measurements of Sea Surface Temperature Through Clouds", en, *Science*, vol. 288, no. 5467, pp. 847–850, 2000. DOI: 10.1126/science.288.5467.847.

[70] E. W. Wong and P. J. Minnett, "The Response of the Ocean Thermal Skin Layer to Variations in Incident Infrared Radiation", en, *Journal of Geophysical Research: Oceans*, vol. 123, no. 4, pp. 2475–2493, 2018. DOI: https://doi.org/10.1002/2017JC013351.

[71] T. R. Karl, A. Arguez, B. Huang, *et al.*, "Possible artifacts of data biases in the recent global surface warming hiatus", *Science*, vol. 348, no. 6242, pp. 1469–1472, 2015.

[72] M. Marshall. "Ships and buoys made global warming look slower". en-US. (2010), [Online]. Available: https://www.newscientist.com/article/dn19772-ships-and-buoys-made-global-warming-look-slower/ (visited on 07/19/2021).

[73] "MOCE-5 Cruise Synopsis". (), [Online]. Available: http://data.moby.mlml.sjsu.edu/timeseries/moce5/General_Info/synopsis_moce_5.html (visited on 08/09/2021).

[74] P. J. Minnett, "Radiometric measurements of the sea-surface skin temperature: The competing roles of the diurnal thermocline and the cool skin", *Int. J. Remote Sens.*, vol. 24, no. 24, pp. 5033–5047, 2003. DOI: 10.1080/0143116031000095880.

[75] "Global Tropical Moored Buoy Array". (), [Online]. Available: https://www.pmel.noaa.gov/gtmba/ (visited on 08/09/2021).

[76] "Global Tropical Moored Buoy Array". en. (2014), [Online]. Available: https://www.pmel.noaa.gov/project/global-tropical-moored-buoy-array (visited on 08/10/2021).

[77] H. Dembinski and P. O. e. al, "Scikit-hep/iminuit", 2020. DOI: 10.5281/zenodo.3949207.

[78] M. Konda, N. Imasato, K. Nishi, *et al.*, "Measurement of the sea surface emissivity", en, *J Oceanogr*, vol. 50, no. 1, pp. 17–30, 1994. DOI: 10.1007/BF02233853.

[79] O. A. Alduchov and R. E. Eskridge, "Improved Magnus form approximation of saturation vapor pressure", *Journal of Applied Meteorology and Climatology*, vol. 35, no. 4, pp. 601–609, 1996.

[80] K. G. Nayar, M. H. Sharqawy, and L. D. Banchik, "Thermophysical properties of seawater: A review and new correlations that include pressure dependence", *Desalination*, vol. 390, pp. 1–24, 2016.

[81] M. H. Sharqawy, J. H. Lienhard, and S. M. Zubair, "Thermophysical properties of seawater: A review of existing correlations and data", *Desalination and water Treatment*, vol. 16, no. 1-3, pp. 354–380, 2010.

[82] A. Duxbury, F. Mackenzie, and R. H. Byrne. "Chemical and physical properties of seawater". en. (2021), [Online]. Available: https://www.britannica.com/science/seawater (visited on 08/13/2021).

[83] N. C. Wells and S. King-Hele, "Parametrization of tropical ocean heat flux", en, *Q.J Royal Met. Soc.*, vol. 116, no. 495, pp. 1213–1224, 1990. DOI: 10.1002/qj.49711649511.

[84] P.-E. Brilouet, J.-L. Redelsperger, M.-N. Bouin, *et al.*, "A case-study of the coupled ocean–atmosphere response to an oceanic diurnal warm layer", *Quarterly Journal of the Royal Meteorological Society*, vol. 147, no. 736, pp. 2008–2032, 2021.

[85] D. Foreman-Mackey, D. W. Hogg, D. Lang, *et al.*, "Emcee : The MCMC Hammer", en, *Publications of the Astronomical Society of the Pacific*, vol. 125, no. 925, pp. 306–312, 2013. DOI: 10.1086/670067.